Stabilization of Electron-Scale Turbulence by Electron Density Gradient in NSTX

by

Juan Ruiz Ruiz

Submitted to the Department of Aeronautics and Astronautics
in partial fulfillment of the requirements for the degree of

Master of Science in Aeronautics and Astronautics

at the

MASSACHUSETTS INSTITUTE OF TECHNOLOGY

June 2015

Signature redacted

Author .....
Department of Aeronautics and Astronautics
May 12, 2015

Signature redacted

Certified by .....
Anne White
Cecil and Ida Green Associate Professor
Thesis Supervisor

Signature redacted

Accepted by .....
Paulo C. Lozano
Associate Professor of Aeronautics and Astronautics
Chair, Graduate Program Committee

Stabilization of Electron-Scale Turbulence by Electron Density Gradient in NSTX

by

Juan Ruiz Ruiz

Submitted to the Department of Aeronautics and Astronautics
on May 12, 2015, in partial fulfillment of the
requirements for the degree of
Master of Science in Aeronautics and Astronautics

Abstract

Microturbulence is present in all magnetic confinement fusion devices, and is believed to play a major role in driving anomalous transport levels that exceed neoclassical theory predictions. In NSTX, electron thermal transport is found to dominate energy loss. Theory and experiments have shown that electron temperature gradient (ETG) turbulence on the electron gyro-scale, $k_\perp \rho_e \lesssim 1$, can be responsible for anomalous electron thermal transport in NSTX. Electron scale (high-k) turbulence is diagnosed with a high-k microwave scattering system [92] in NSTX. Here we report on the stabilization effects of the electron density gradient on electron-scale density fluctuations in a set of neutral beam injection (NBI) heated H-mode plasmas. We found that the absence of high-k density fluctuations from measurements is correlated with large equilibrium density gradient, and this correlation will be shown to be consistent with linear stabilization of ETG modes due to density gradient by using the analytical ETG linear threshold in [94] and linear gyrokinetic simulations with GS2 [95]. We also found that the observed power of the electron-scale turbulence (when it exists) is anti-correlated with the equilibrium density gradient. Thorough analysis of electron density fluctuations from the high-k scattering diagnostic at NSTX shows that larger equilibrium density gradient leads to higher values of the wavenumber corresponding to the maximum in the fluctuation wavenumber spectrum. Higher equilibrium electron density gradient also gives rise to a lower value of the plasma frame frequency of the detected density fluctuations. Linear gyrokinetic simulations using GS2 are in agreement with experimental results, and show a clear correlation between the wavenumber value at the maximum linear growth rate and the local value of the electron density gradient. Higher values of the electron density gradient are also shown to reduce the value of the real frequency of instability.

Thesis Supervisor: Anne White
Title: Cecil and Ida Green Associate Professor

Acknowledgments

I would like to thank my academic advisor Prof. Manuel Martinez-Sanchez for helping me come to MIT. Manuel had faith in me and first brought me to MIT as a visiting student to the Space Propulsion Laboratory in Spring 2013. My time in the Space Propulsion Laboratory was extremely enriching and fruitful, and I wanted to personally thank Manuel for his support and faith in me.

I would like to show my gratitude to Prof. Anne White for recruiting me to MIT. Anne believed in me since the first moment, and has devoted incredible amounts of time and effort to teach me and help me grow as a graduate student. Our physics discussions have contributed in great value to my education, and I am really looking forward to continuing those discussions in the next few years.

I would like to thank all professors at the Plasma Science and Fusion Center. The quality of the classes imparted at PSFC and the quality of the faculty and staff are difficult to match anywhere else in the world. I have had the privilege to take classes from Prof. Ian Hutchinson, Prof. Anne White, Prof. Jeffrey Freidberg and Prof. Porkolab. All classes were of great intellectual level and have given me a solid background on plasma physics and fusion energy. I look forward to taking other classes at PSFC in the near future.

I would also like to thank fusion's entering class of 2013, in particular I would like to thank my officemate Daniel Kwak, and classmates Silvia Espinosa, Chuteng Zhou and Franco Mangiarotti. I have had the privilege to be around very intelligent individuals and I have taken advantage of our fruitful interactions.

I also have to thank my whole family in Spain. My family has always had great expectations on me and they have supported me on all decisions I have made in life. It is not easy as a graduate student to study for a Masters or a doctoral degree abroad, far away from your loved ones, but their support has given me the energy to get to this point: I have a great family and for that I am truly thankful. I could not have done this without them.

Contents

List of Figures

Chapter 1

Introduction to Controlled Thermonuclear Fusion

1.1 Role of fusion in the energy scene.

The ultimate goal of controlled thermonuclear fusion is the production of energy. The world population is continually increasing, and the demands on electricity, and thus energy production, are expected to increase in the future. Magnetic confinement fusion energy is one of the most promising techniques that addresses key issues that the world needs to face with respect to energy production.

Magnetic fusion energy has several important advantages when compared to existing energy sources today. The main advantages are the reserves of fuel, the impact on the environment and safety. The reserves of fusion fuel on earth are extremely abundant, and could provide the world population with energy for centuries. The basic fuel for a fusion reaction are light elements, such as hydrogen (H) and its isotopes deuterium (D) and tritium (T). Deuterium is naturally present on earth, and its natural abundance with respect to hydrogen is 1 atom of deuterium for every 6,400 atoms of hydrogen [1]. The earth's oceans are natural reservoirs of hydrogen and deuterium and their large quantities are infinite from a practical viewpoint. Tritium is not naturally present on earth but it can be obtained by breeding reactions with the Li^6 isotope. Tritium production is subject to the natural abundance of Li^6 on earth. Geological estimates indicate that the natural

abundance of the lithium-6 isotope on earth is sufficient for fusion energy to provide the base-load electricity supply for an order of a thousand years [1] (assuming increases in global energy demands, and base-load provided by fusion is taken to be 30 %). The environmental impact of fusion is practically inexistent and fusion reactions produce no greenhouse emissions contrary to existent energy sources such as oil or coal. Fusion energy is also a safe energy source and will not give rise to a radioactive meltdown.

It is important to mention the several disadvantages fusion has with respect to existent energy sources. The science of fusion is intrinsically complex and is explained by plasma physics. Numerous scientific challenges involving the physics of fusion plasmas have yet to find a solution, namely the control of a self-heated plasma and non-inductive steady state operation. There are also technological challenges that need to be addressed, namely the problem of plasma-wall interactions and the divertor problem. The development of high-field superconducting magnets and structural materials able to sustain the strain from magnetic forces are also imperative issues that need a solution. The economic challenges from fusion come from the inherently complex nature of a fusion facility. Complexity means cost, and in order to become an energy source in the future, fusion needs to be competitive cost-wise with other energy options existent today.

1.2 Principles of fusion energy.

Fusion is a form of nuclear energy and is the source of energy that powers the sun. In a fusion reaction, light elements (nuclei) merge together to form heavier nuclei. The mass difference between products and reactants provides an excess energy to the products known as reaction yield. This energy is needed to sustain the fusion reaction. The mass difference can be calculated using the famous Einstein's relation $E_{reactants} - E_{products} = \Delta mc^2$. The principal reaction considered is the deuterium-tritium (D-T) reaction. As deuterium and tritium fuse, they produce an alpha particle (helium nucleus) and a high-energy neutron. In order for fusion reactions to occur, nuclei need to have sufficient energy to overcome the mutual repulsion from the Coulomb potential barrier. The minimum temperature for a D-T fusion reaction to occur is typically on the order of 10^8 K (10 keV. In plasma physics and in this manuscript we use energy units for temperature $k_B T \rightarrow T$).

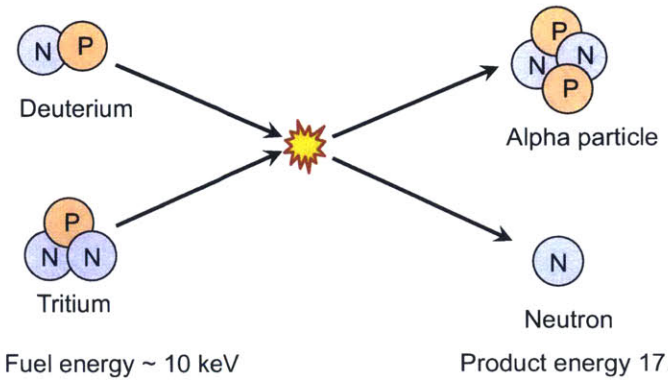

Figure 1-1: Deuterium-Tritium fusion reaction. P and N stand for *proton* and *neutron* respectively.

As a comparison, the D-T fusion reaction produces 17.6 MeV of energy. The D-T fusion reaction is shown in Fig. 1-1.

The D-T fusion reaction is expected to power the first generation fusion power plants. However, the D-T reaction has its advantages and disadvantages. On figure 1-2 are compared to the D-T, D-D and D-He^3 reaction rates and cross sections. The deuterium-deuterium (D-D) and deuterium-helium 3 (D-He^3) reactions could be possible candidates for powering future generation power plants. The quality or performance of a fusion reaction can be described by the reaction cross section (fig. 1-2 a)) or the reaction rate (fig. 1-2 b)), indicative of the probability for a reaction of occurring. For values of energy below about 100 keV, the D-T reaction has the largest cross section and reaction rate. For this reason it is the major candidate for first generation fusion reactors. However, tritium is not present naturally on earth and would have to be produced, for example, by a breeding reaction with lithium (Li^6). Earth's natural lithium reserves are not as abundant as deuterium reserves. As fusion energy research continues to develop, alternate fusion reactions like D-D or D-He^3 could become more interesting in the far future, as lithium reserves become scarce on earth. Additionally, the D-D reaction produces less energetic neutrons, which can be a radiological concern.

Plasma is the state of matter at temperatures necessary for fusion reactions to occur. At fusion temperatures, electrons are completely or partially disassociated from atomic nuclei, and the result is a soup of charged particles, electrons and ions, called *plasma*. Charged particles in the plasma respond to electric forces from other charged particles and

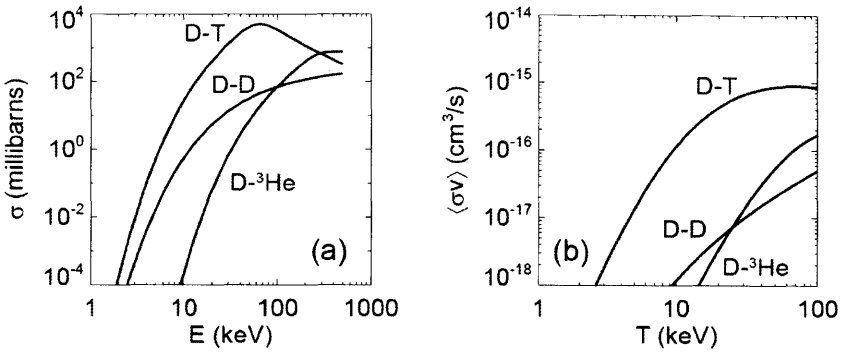

Figure 1-2: a) Fusion reaction cross sections. b) Fusion reaction rates, averaged over a Maxwellian distribution function [2].

give rise to shielding. This collective behavior shields particles for distances greater than the Debye length λ_D, given by $\lambda_D = \left(\epsilon_0 T_e / n_e e^2\right)^{1/2}$, where T_e is the electron temperature and n_e is the electron density in the plasma. The shielding effect on a test particle in the plasma is shown on figure 1-3. Plasma physicists define what is called the plasma parameter Λ by $\Lambda = \frac{4\pi}{3} n_e \lambda_D^3$. This parameter denotes the number of particles that live inside a sphere centered on the test particle with radius λ_D, called the Debye sphere. If $\Lambda >> 1$ a large number of particles are susceptible of interacting with a test particle and a statistical treatment of the plasma (based on the theory of statistical physics) is adequate. A simple manipulation allows expression of the plasma parameter Λ as the ratio of a characteristic kinetic energy of particles (E_{th}, given by the temperature T_e) to the characteristic energy of Coulomb interactions between particles distant $\sim \lambda_D$ (Fig. 1.1). Hence the condition $\Lambda >> 1$ translates the fact that the kinetic energy of particles is much higher than the Coulomb interaction energy, and collective effects within the plasma dominate over Coulomb collisions.

$$\Lambda = \frac{4\pi}{3} n_e \lambda_D^3 \propto \left(\frac{T_e}{e^2 / 4\pi\epsilon_0 \lambda_D} \right)^{3/2} = \left(\frac{E_{th}}{E_{Coul}} \right)^{3/2} = 5.4 \times 10^6 \frac{T^{3/2}}{n^{1/2}} \qquad (1.1)$$

In equation 1.1, T is measured in keV (1 keV $\sim 10^7 K$) and n is measured in units of $10^{20} m^{-3}$. For typical fusion plasma of $T = 15\ keV$ and $n = 2 \times 10^{20}\ m^{-3}$, $\Lambda \sim 10^8$. The condition of collective effects to dominate over Coulomb interactions is largely satisfied by a fusion plasma. The definition of the Debye length is central in plasma physics. In this

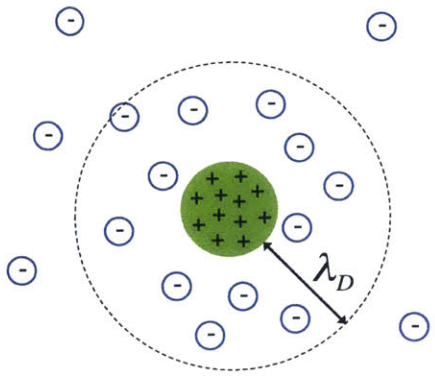

Figure 1-3: Debye shielding effect in a plasma. Beyond the Debye length λ_D a test particle is shielded out. The Debye sphere denotes the volume of particles in the plasma that are sensitive to interact with a test particle.

thesis we will make use of the Debye length to define coherent and incoherent scattering of waves in the plasma. In this thesis, coherent scattering of micro-waves is used to diagnose turbulence in the plasma through measurement of fluctuations in the plasma density.

There are other requirements a fusion plasma has to obey in order to attain fusion reactor conditions and yield a net energy production. The plasma has to be confined for a sufficiently long time and be sufficiently dense in order for sufficient fusion reactions to occur. The initial calculations of power balance analysis in a thermonuclear fusion reactor were made by J. D. Lawson in his original publication [3], where he introduced the importance of the parameter $n\tau_E$. n is the plasma density and τ_E is the energy confinement time. The energy confinement time is a measure of the confinement quality of the plasma, and is defined as the ratio between the total energy in the plasma by the total power loss by the plasma. This definition responds to a intuitive sense of confinement time: τ_E increases with the total plasma energy and decreases with plasma power loss. We have already mentioned the importance of achieving a high temperature in order for fusion reactions to take place. A simple criterion that takes into account all the previous requirements on $n\tau_E$ and T can be summarized in a simple triple product condition,

$$nT\tau_E > 3 \times 10^{21} m^{-3} keV s \tag{1.2}$$

Ignition is achieved when fusion power from fusion reactions balances energy losses in the plasma and is the ultimate goal towards achieving steady state fusion reactor op-

eration. The energy confinement time τ_E has proven to be the most difficult parameter to increase due to complicated mechanisms that produce energy loss in the plasma. The confinement of a fusion plasma has been a big concern ever since the beginning of controlled thermonuclear fusion research. In stars and our sun, confinement is achieved by the enormous gravitational force exerted on the plasma. However, fusion reactions do not naturally occur on earth and the high temperatures needed to produce fusion reactions make the confinement of a fusion plasma on earth a daunting task. Controlled thermonuclear fusion research has conceived two ways of achieving fusion: inertial confinement fusion and magnetic confinement fusion. Inertial confinement fusion seeks to produce fusion energy by exerting huge pressures on a small pellet of fuel which will be be compressed to high temperature and inside which fusion reactions will occur. There are nowadays two main inertial confinement fusion facilities in the world, the National Ignition Facility (NIF) situated at the Lawrence Livermore National Laboratory in Livermore, California, and the project Laser Megajoule in Bordeaux, France. On the other hand, magnetic confinement fusion seeks to use magnetic fields to exert a force on the plasma particles and produce confinement.

1.3 Magnetic confinement fusion.

As the name indicates, magnetic confinement fusion devices seek to use magnetic fields to produce confinement. When subject to a uniform magnetic field charged particles gyrate in circular motion around magnetic field lines and drift at constant velocity parallel to the magnetic field line. By bending the magnetic field lines in a closed shape particles should remain confined to the field line. This is the principle behind magnetic confinement fusion, as implemented today in tokamaks and stellarators. Stellarators were first conceived by Lyman S. Spitzer in the 1950's and his ideas gave rise to Project Sherwood on controlled thermonuclear fusion. Tokamaks were conceived in the Soviet Union from original theoretical ideas of red army soldier Lavrent'ev [5] that were further exploited by Sakharov and Tamm [5–7] and developed into the tokamak concept we have today.

The curvature and non uniformity of the magnetic field lines created in stellarator and

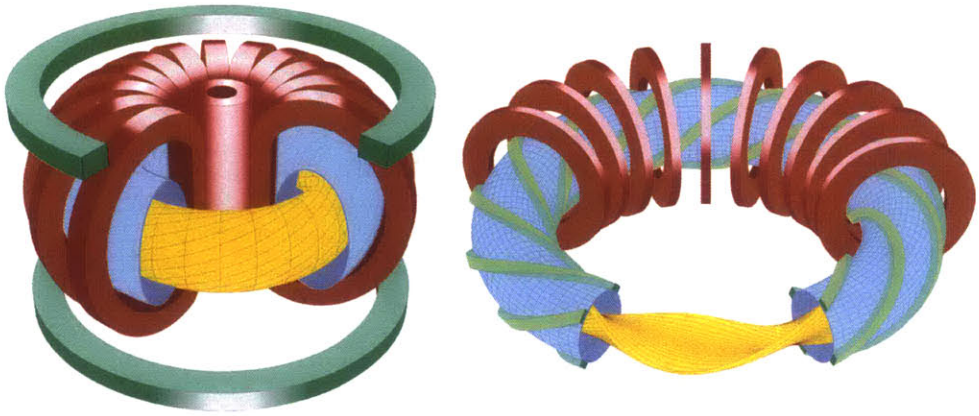

Figure 1-4: Tokamak (left) and stellarator (right) design concepts. Notice the axis of symmetry present in a tokamak. Courtesy of [4].

tokamak devices give rise to particle drifts across the magnetic field lines. Particles are subject to drifts perpendicular to the magnetic field lines which translate into particle and energy losses from the plasma to the outside, hence degrading the confinement. Stellarators have overcome this difficulty by using helical magnetic field lines that balance particle drifts (Fig. 1-4 b)). Tokamaks have a torus shape and are symmetric around an axis (axisymmetric) by design (Fig. 1-4 c)). Tokamaks rely on the presence of an electric current along the toroidal direction (the long way around the torus, subscripted t. cf. Fig 1-5) that will in turn produce an additional magnetic field in the poloidal direction (subscripted p, cf. Fig. 1-5). The poloidal magnetic field $\boldsymbol{B_p}$ in a tokamak curves magnetic field lines in the poloidal direction and produces the confinement. Sustaining the electric current, and thus the poloidal magnetic field, by non-inductive means, is of great importance in tokamak research nowadays.

The axisymmetry of a tokamak greatly reduces the complexity of the geometry with respect to the stellarator and also allows the existence of simpler, closed flux surfaces compared to the the stellarator (also known as magnetic surfaces). To introduce the concept of flux surfaces it is useful to mention the concept of magneto-hydrodynamical equilibrium. The theory of magneto-hydrodynamics is a fluid theory that is very well suited to describe the equilibrium state of toroidal plasmas. The equilibrium state of a tokamak plasma is well described by the force balance equation

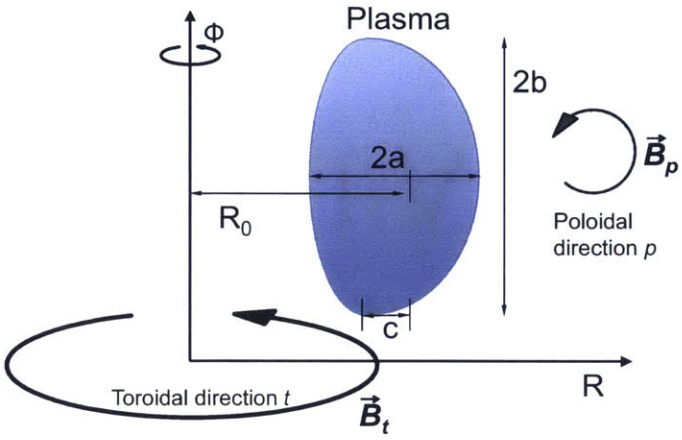

Figure 1-5: Schematic representation of the geometry in a tokamak device. R_0 is the major radius and a is the minor radius. t is the toroidal direction and p is the poloidal direction.

$$\boldsymbol{J} \times \boldsymbol{B} = \boldsymbol{\nabla} P \tag{1.3}$$

where P is the pressure, $\boldsymbol{J}$ is the total current density and $\boldsymbol{B}$ the total magnetic field. By taking the dot-product of that equation with $\boldsymbol{B}$ one gets $\boldsymbol{B} \cdot \boldsymbol{\nabla} P = 0$, which means that magnetic field lines lie in surfaces of constant pressure. One can prove that these surfaces also preserve poloidal magnetic flux [8]. In fact, one can prove that pressure P and current $\boldsymbol{J}$ are flux functions (functions only of poloidal flux), such that $P = P(\psi)$ and $\boldsymbol{J} = \boldsymbol{J}(\psi)$, where ψ is the value of the poloidal flux. These surfaces are known as flux surfaces. Flux surfaces can be theoretically well defined in a very precise manner, but this simplistic definition allows to easily grasp the concept behind flux surfaces. For more precise definitions of flux surfaces, the reader is referred to [8].

1.4 Standard tokamak and the spherical tokamak (ST)

Research based on the spherical tokamak (ST) design [9] began in the 1990s with the tokamak START [10] in the Culham Science Centre in the United Kingdom. START revolutionized the tokamak and led the construction of two new ST devices: the National Spherical Tokamak Experiment (NSTX [11, 12]) in the Princeton Plasma Physics Laboratory and the Mega Ampere Spherical Tokamak (MAST [13]) also at Culham, both

currently undergoing a major upgrade.

The mission of NSTX and MAST is to establish the physics baseline to test the viability of the ST as a practical fusion power source such as ST-FNSF (Spherical Torus Fusion Nuclear Science Facility [14, 15]). The ST provides access to a wide variety of new regimes inaccessible to the standard tokamak. The main goals of NSTX can be summarized as follows: simultaneously attain high-β (1.4.1), high confinement (1.4.2) and high bootstrap fraction (1.4.3), and provide solutions to handle the heat loads on plasma facing components (1.4.4).

Figures 1-6 and 1-7 are shown flux surfaces for a standard tokamak and for typical NSTX plasmas. The magnetic axis is defined as the innermost flux surface (reduced to a point in Fig. 1-7) and the last closed flux surface determines the plasma boundary. Flux surfaces can be open or closed depending on their topology ($cf.$ Fig. 1-7 b)) and are delimited by the last closed flux surface (LCFS). The aspect ratio of a tokamak plasma is defined as $A = R_0/a$, where R_0 is the major radius of the LCFS and a is the LCFS minor radius (Fig. 1-5). Standard tokamak plasmas are large aspect ratio, typically $A \gtrsim 3$ while spherical torus plasmas (ST) are $A \sim 1$ (Fig. 1-6) and this is a major difference between standard tokamaks and spherical tori. The inverse aspect ratio is $\epsilon = a/R_0$. The elongation is defined as $\kappa = b/a$ where $2b$ is the LCFS height and the triangularity $\delta = c/a$ ($cf.$ Fig. 1-5). The safety factor q can be defined as the number of turns in the toroidal direction per one full poloidal turn and it is a measure of how *curved* the magnetic field lines are in the poloidal direction. At large aspect ratio we obtain the cylindrical limit of the safety factor $q \approx rB_t/RB_p$, where $B_t = |\boldsymbol{B_t}|$ is the value of the magnetic field in the toroidal direction, and $B_p = |\boldsymbol{B_p}|$ is the magnetic field in the poloidal direction ($cf.$ Fig. 1-5 for clearness). The magnetic shear $\hat{s}$ is defined as the logarithmic radial derivative of the safety factor $\hat{s} = \mathrm{d}ln(q)/\mathrm{d}ln(r)$ and it is a measure of how *sheared* are the magnetic field lines from one flux surface to another. The magnetic shear $\hat{s}$ and safety factor q are of great importance in tokamak plasmas as they can stabilize some magnetohydrodynamic instabilities as well as micro instabilities that give rise to loss of particles, energy and momentum across the magnetic field lines (transport).

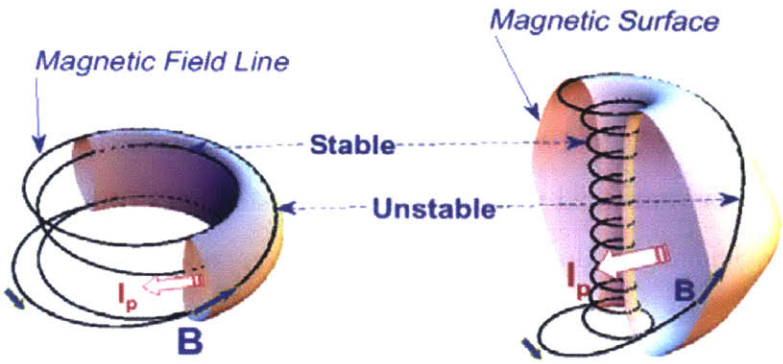

Figure 1-6: Comparison of conventional tokamak and spherical tokamak configurations (from [91]). B is the magnetic field direction and I_p the plasma current.

1.4.1 High toroidal beta

The plasma toroidal-β is defined as the ratio between the average plasma pressure to the applied magnetic field pressure, that is

$$\beta_t = \langle P \rangle / (B_t^2 / 2\mu_0) \tag{1.4}$$

In this definition, $\langle . \rangle$ indicates the average over the flux surface, also known as flux surface average. The toroidal-β measures how efficiently the applied magnetic field of the tokamak is used to produce confinement. NSTX has achieved values of β_t approaching 40%, about a factor of 4 greater than that accessible to standard tokamaks. High plasma β is also important towards the development of a pilot ST power plant since high plasma pressure is needed to produce fusion reactions (fusion power scales as the squared of plasma pressure $\langle P \rangle^2$).

1.4.2 High confinement

The confinement properties of an ST can be substantially different to those in a standard tokamak. Assessing the confinement quality from first physics principles has proven to be a challenge in tokamaks. A popular way to evaluate the confinement performance in tokamaks are empirical 'scaling laws' that relate the energy confinement time to typical tokamak parameters such as the I_p, B_t, R, etc (I_p is the total plasma current, not to confuse with the poloidal direction, subscripted p). In NSTX, the H-mode global en-

ergy confinement has been shown to have a very strong dependence on collisionality $B\tau_E \sim 1/\nu_e^*$ [20] and is different from the ITER98y$_2$ scaling $B\tau_E \sim$ independent of ν_e^* [16] (the electron collisionality ν_e^* measures the importance of Coulomb collisions in the plasma). The energy confinement scaling on collisionality exhibited in STs is radically different to that exhibited in standard aspect ratio tokamaks and is favorable to operation in low-collisionality regimes for future STs.

The low aspect ratio $A = R_0/a$, high elongation $\kappa = b/a$ condition of STs induce strong magnetic field line curvature on ST plasmas ($cf.$ Fig. 1-6). High magnetic field line curvature is believed to have a stabilizing effect that can improve confinement with respect to standard tokamaks. Neutral Beam Injection (NBI) heated plasmas at NSTX exhibit high $E \times B$ shearing rates that have proven beneficial to the confinement in STs with respect to standard tokamaks. At the same time, fast-ion populations coming from NBI can in turn destabilize a particular set of instabilities known as Alfvén eigenmodes, which can give rise to high levels of transport and hence degrade the confinement. Furthermore, high beta levels attained in NSTX can also destabilize electromagnetic modes such as micro-tearing modes (MT). Drift wave modes such as the electron temperature gradient (ETG) instability are also routinely found unstable in NSTX. This thesis makes a contribution towards the understanding of the ETG-driven micro instability, diagnosed experimentally with the high-k scattering system at NSTX [92]. By scattering microwaves off the plasma the high-k scattering diagnostic at NSTX is able to measure density fluctuations on the electron gyro-radius scale (ρ_e) that are indicative of the ETG instability. It is found that the local value of the electron density gradient has a stabilizing effect on electron density fluctuations. Linear gyrokinetic simulations carried out with the GS2 code [95] show that the electron density gradient value is correlated with the wavenumber at peak linear growth rate, and anticorrelated with high-k linear growth rate values. One important research thrust for NSTX-U and many other tokamaks world-wide is the study of the transport of electron energy. Electron thermal transport is routinely the main energy loss channel at NSTX and is observed to be much higher than predicted by theory (more on this on next section). The toroidal ETG instability is thought to be responsible for these *anomalous* levels of electron thermal transport under some operating regimes. Diagnosing the ETG instability with the high-k scattering diagnostic at NSTX

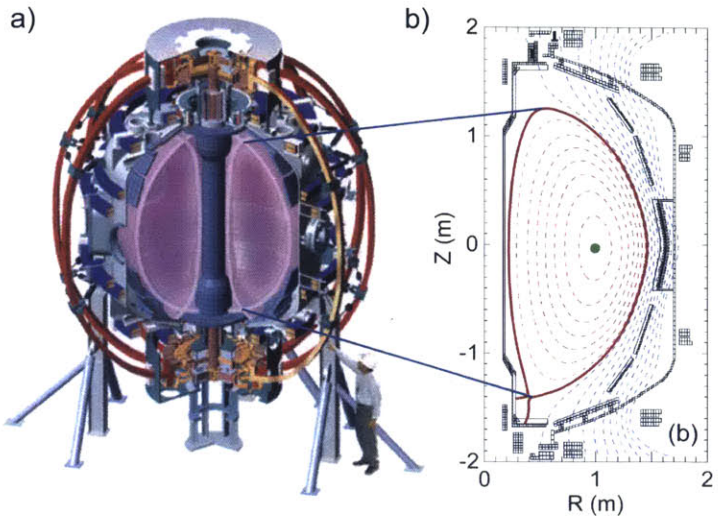

Figure 1-7: a) NSTX device. b) Poloidal flux surfaces (also simply flux surfaces or magnetic surfaces) in a typical NSTX plasma: last closed flux surface (LCFS) in solid red, open flux surfaces in dashed blue lines, closed flux surfaces in dashed red lines. Because the pressure P is a flux function ($P = P(\psi)$), these are also contours of constant pressure. The magnetic axis is a green dot.

is important to gain a deeper understanding to the problem of electron thermal transport. In addition to the ETG instability at NSTX, the coexistence of all the micro instabilities mentioned in this paragraph makes the study of confinement and the transport properties in STs substantially different than in standard high aspect ratio tokamaks.

1.4.3 High bootstrap fraction: towards steady-state operation

We previously emphasized the importance of a toroidal electric current in the tokamak. Since the first tokamaks came into operation, tokamaks have relied on transformer inductive action as a mechanism to drive current, having the plasma as the secondary circuit. This method is not able to drive current and produce the confinement needed for steady state operation in a reactor. New methods of so-called *non-inductive* current drive are envisioned to exist in future reactor scale fusion plants, and are an area of current research nowadays, particularly in NSTX.

A very important contribution to the total current driven in NSTX (and also in NSTX-U [26]) is the bootstrap current. In the 1970s, it was theorized that pressure gradients between the hot core and the cold edge region in a toroidal plasma would drive a toroidal

plasma current due to the friction force between particles in the plasma [30, 31]. The bootstrap current has been experimentally observed in tokamaks since the 1980s, and it is expected to play a major role in future fusion reactor plants since it will relax the constraints on non-inductive current drive systems. It is thought that the plasma current in a fusion power plant should have a bootstrap fraction on the order of 80%. In the limit of unit aspect ratio ($A = R_0/a = 1$), the bootstrap current takes a simple form

$$j_{BS} = -R\frac{dP}{d\psi} = -R\frac{dP}{dr}\frac{dr}{d\psi} \tag{1.5}$$

as shown in [28], where ψ is the poloidal flux (recall the pressure P is a flux function: $P = P(\psi)$). This simple expression for j_{BS} directly highlights the importance of the pressure gradient contribution to the bootstrap current. When we consider larger aspect ratio ($A > 1$, $\epsilon = 1/A < 1$), the bootstrap current has a dependency as follows $j_{BS} \approx -\epsilon^{1/2} R dp/d\psi$. It is interesting to compare the scaling relationship between j_{BS} and the Ohmic current j_{OH} (current usually driven by an electric field, though it can also be driven by neutral beams or waves)

$$j_{BS}/j_{OH} \sim \epsilon^{1/2}\beta_p \tag{1.6}$$

where $\beta_p = 2\mu_0 P/B_p^2$ is the poloidal beta. This dependency shows a favorable contribution of the bootstrap current in small inverse aspect ratio tokamaks, such as STs ($\epsilon \sim 1$). In addition, the scaling on β_p is favorable for the spherical tokamaks since STs are designed to operate at high beta with respect to standard tokamaks. For a detailed discussion of the physics behind the bootstrap current the reader is referred to [28, 29]. The bootstrap current was experimentally confirmed in tokamaks in the 1980s [32]. Obtaining high bootstrap current fractions $f_{BS} = I_{BS}/I_p$ (I_p is the total current carried by the plasma and and I_{BS} is the total bootstrap current) is very beneficial to tokamaks since it relaxes the obligation for auxiliary current drive systems. As we have seen, the bootstrap current is very effective in the ST because of its low aspect ratio A and high-β (NSTX has achieved 70% of bootstrap current fraction).

NSTX complements bootstrap current drive by using a coaxial helicity injection (CHI [33]) system, NBI and a high-harmonic fast wave (HHFW [34]) system. CHI is used at

NSTX for plasma current initiation and has delivered 160 kA of current. NBI and HHFW act both as auxiliary plasma heating and current drive systems. NBI relies on the injection of fast-neutrals that will become ionized once they enter the plasma. The fast-ion population originating from NBI fast neutrals will carry a current that will eventually slow down on the plasma. The overdense plasma condition of NSTX plasmas ($\omega_{pe}/\Omega_e > 1$) precludes the use of conventional electron cyclotron heating (ECH) and electron cyclotron current drive (ECCD). In these overdense scenarios, a HHFW system has proven successful to heat and drive current in NSTX plasmas. The NSTX HHFW system uses 30 MHz waves injected in the plasma, and is able to couple up to 6 MW of power. Core electron temperatures of over 5 keV have been achieved in HHFW heated plasmas at NSTX.

1.4.4 Solving the plasma heat load problem

High power levels are anticipated in conventional tokamak test reactors as well as in compact STs, and will give rise to high heat flux loads on plasma facing components (PFC), in particular the divertor. The divertor in a tokamak is a device allowing the removal of waste material from the plasma and it can reach heat flux levels of up to $10MW/m^2$, comparable to levels expected to be attained in ITER. NSTX is unique in the world fusion program for investigating the impact of lithium PFCs on H-mode plasmas. It has been shown that lithium can offer several potential benefits such as enhancing thermal confinement and the suppression of edge localized modes (ELMs). ELMs are disruptive instabilities typical of H-mode plasmas that create bursts of energy and particles that can seriously damage PFCs and the divertor. In addition to the use of lithium PFCs, resonant magnetic perturbations (RMPs) coils were installed on NSTX and NSTX-U to mitigate ELMs, following succesful demonstration at the DIIID tokamak [27]. So far RMPs have triggered, rather than stabilized ELMs at NSTX and further research understanding the mechanisms of RMPs will continue at NSTX-U. High flux expansion is another viable possibility to reduce heat flux peaks on the divertor plates. Magnetic configurations such as the "snowflake" divertor have been successfully implemented at NSTX and further investigation will continue on NSTX-U.

R	0.85 m
a	0.68 m
I_p	1 MA
B_T	0.3 T
κ	2.0
R/a	1.25
Startup	OH, electron cyclotron heating (CHI)
Wall stabilization	Close-fitting conducting plates
Auxiliary heating and current drive	CHI, HHFW (6 MW), NBI (5 MW)
Profile control	HHFW, CHI, NBI
Maximum pulse length	5 s (> current relaxation time)
Divertor	Single- and double-null, IWL
Profile diagnostics	

Figure 1-8: Original NSTX device capabilities as a first of a kind, ultra-low aspect ratio spherical torus (from [93]). Note the magnetic field has since then been increased to $B = 0.55$ T for NSTX, and will achieve 1 T for NSTX-U. The plasma current I_p is expecting a upgrade to 2 MA for NSTX-U.

1.5 Thesis scope

In this thesis, I present the analysis results of a series of experiments that measure high-k turbulence levels in NSTX. Theory and numerical simulations [97, 98, 101–106] have suggested that micro instabilities driven by the electron temperature gradient (ETG) could be responsible for the anomalous electron thermal transport levels observed experimentally. ETG turbulence is diagnosed in NSTX plasmas using the high-k scattering diagnostic. The high-k scattering diagnostic measures electron density fluctuations on the electron gyro radius scale ($k_\perp \rho_e \lesssim 1$) using a 280 GHz microwave coherent scattering system [92]. The scattering system consists of five collection channels that simultaneously measure five different wave numbers in the range $5 \lesssim k_\perp \lesssim 30$ cm^{-1}. Heterodyne receivers installed on each channel allow to determine the direction of propagation of the observed fluctuations. The wavenumber resolution of the observed electron density fluctuations is $\Delta k \approx \pm 0.7$ cm^{-1} and the radial resolution $\Delta R \approx \pm 2$ cm. Measured wave vectors are primarily radial k_r, with a small binormal component k_b satisfying $k_b/k_r \approx 0.2 - 0.3$ (k_r is the radial component perpendicular to the flux surface and k_b is the binormal component perpendicular to the local magnetic field but inside the flux surface). A ray tracing code was used to compute the detected wavenumbers by each channel of the high-k system. Linear gyrokinetic simulations with the gyrokinetic code GS2 complement the experimental study carried out with the high-k scattering diagnostic.

The chapter 2 of this thesis gives is a general background on plasma turbulence and transport in tokamaks, and the distinctive features of transport in spherical tokamaks. Chapter 3 discusses the physical principles underlying the scattering process taking place in the measurement of electron scale density fluctuations, and describes the experimental configuration of the high-k scattering diagnostic at NSTX. Chapter 4 provides the analysis tools used in the course of this work to analyze electron density fluctuation measurements, carry out linear gyrokinetic simulations with GS2, ray tracing calculations and TRANSP calculations. Chapter 5 describes the experimental observation of the background equilibrium density gradient as a stabilizing mechanism on high-k turbulence at NSTX. Linear gyrokinetic simulations with GS2 support the experimental observations.

Chapter 2

Plasma Turbulence and Transport Background

The theory of transport goes well beyond plasma physics. By definition transport describes situations that are out of equilibrium, and can be explained by the theory of non-equilibrium thermodynamics. We start this chapter by describing transport as a diffusive process. We will then turn to explain transport in conventional aspect ratio tokamaks, and will end by giving a very brief review of the current understanding of transport processes in spherical tokamaks such as NSTX.

2.1 Transport as a diffusive process

Particle, momentum and heat fluxes can be rigorously calculated from first-principle physics. Non-equilibrium thermodynamics defines transport fluxes having a linear relation to thermodynamic forces (typically given by gradients of a certain physical quantity) for situations close to equilibrium. In that context, we can define transport fluxes as the proportionality factor between a transport flux and a thermodynamic force. A simple constitutive relation is given by Fick's law

$$\Gamma_r = -D\frac{\partial n}{\partial r} \tag{2.1}$$

which states a linear relation between a particle flux Γ_r and its conjugate thermody-

namic force $\partial n/\partial r$. The simple Fick's relation 2.1 coupled with the particle conservation equation results in the well-known diffusion equation. The proportionality factor D is known as the particle diffusivity. The analogous relation to 2.1 for energy defines a radial heat flux Q_r and heat diffusivity χ as a function of the conjugate thermodynamic force $\partial T/\partial r$ as $Q_r = -n\chi\partial T/\partial r$. In reality, and in particular in tokamak plasmas, fluxes cannot always be simply expressed as a function of its conjugate thermodynamic force, and several thermodynamic forces might come in play in the definition of a particular flux. In this thesis, we will look at a particular type of flux, the electron heat flux in tokamak plasmas. A process in which fluxes exhibit a linear relationship with thermodynamic fluxes is known as a diffusive process. In tokamak plasmas, situations may arise where fluxes are also non-diffusive. A simple but realistic example of a non-diffusive process is $\Gamma_r = -D\partial n/\partial r + Vn$. In this case, the term Vn is known as the convective term and V is the convective velocity. Such an expression for the flux will give rise to what is commonly known as the advection-diffusion equation. This form has been applied to tokamak plasmas and experimentally verified [52].

2.2 Transport in conventional aspect ratio tokamaks.

Transport of particles across the magnetic field lines in a magnetically-confined plasma determines the confinement quality of the plasma. Small transport levels of particles and energy across the magnetic field will give rise to good confinement. In a uniform magnetic field, particles gyrate around the magnetic field in circular motion and move at constant velocity along the magnetic field. When particles are part of a plasma, Coulomb collisions are inevitable and they give rise to transport of particles from one magnetic field line to another, commonly known as classical transport. Magnetically confined plasmas are inherently nonuniform and anisotropic with densities and temperatures that peak in the plasma core. Transport processes driven by gradients are enhanced by geometrical effects and exceed classical transport in a uniform magnetic field. This so-called 'neoclassical transport' is based on a robust, first principles physics foundation [35] and studies transport due to collisions in a toroidal geometry such as the tokamak. Many aspects of neoclassical transport theory have been verified experimentally [32,36–38], as is the case for

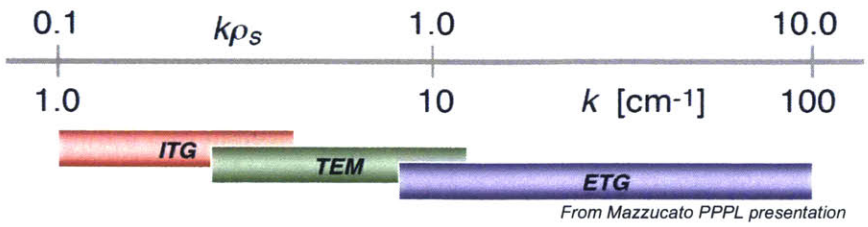

Figure 2-1: Expected wavenumber values for relevant drift wave turbulent modes in magnetically confined fusion plasmas. Of particular importance to spherical torii is the ETG instability. Note here that values for the ion sound gyro-radius ρ_s were taken from typical NSTX discharges (ρ_s is computed using T_e and m_i instead of T_i and m_i as in ρ_i).

the bootstrap current. Neoclassical transport sets the irreducible minimum transport level attained in a tokamak. Despite success at describing parallel heat transport in tokamak plasmas, bootstrap current, and in many cases impurity transport, neoclassical transport is not able to predict experimental levels of cross-field (perpendicular) heat transport in the plasma.

The excess transport observed in experiments is widely referred to as *anomalous* transport, and electron heat transport remains the least understood transport channel. Radial transport in present day experiments exceeds predictions from neoclassical theory by up to three orders of magnitude. This disagreement between first principles theory and experiments has existed since the beginnings of tokamak plasmas. Theories today are still far from being able to explain anomalous transport in tokamaks but a huge progress has been made and the gap is closing in. Anomalous transport is currently widely attributed to small-scale micro instabilities that give rise to turbulence in the plasma [39,40].

Of particular importance is the transport of electron energy. In a thermonuclear fusion reactor, high energy alpha particles will transfer most of their energy to the electrons. Electrons thus play a key role in the sustainment of plasma energy in a reactor, hence the importance of the electron thermal transport problem. In current fusion experiments such as NSTX, electron thermal transport is regularly found at anomalous levels. As was previously mentioned, this thesis contributes to the understanding of electron thermal transport by focusing on a particular micro instability called the electron temperature gradient instability (ETG). The ETG instability is also found to play a very important role in conventional aspect ratio tokamaks, as will be discussed in the next section.

In the core of a standard tokamak, the current belief is that most of the turbulence is driven by drift waves. Drift waves propagate in the plasma perpendicularly to density and temperature gradients. Drift waves can become unstable in a toroidal plasma due to inhomogeneities and gradients (namely of density) and due to geometrical and curvature effects, which can further enhance the instability of these modes. Depending on the instability drive of drift waves, they are identified as the ion temperature gradient driven instability (ITG [41–44]), the trapped electron mode (TEM [45]) and the electron temperature gradient driven instability (ETG [46]). Drift waves are highly anisotropic. The spatial scale length perpendicular to the magetic field can be of the order of the ion gyro-radius ρ_i (ITG, TEM), and it can even go down to a factor of the electron gyro-radius ρ_e (ETG). In the plasma turbulence and transport context, the ITG and TEM instabilities are characterized by $k_\perp \rho_i \sim 1$, whereas the ETG instability is characterized by $k_\perp \rho_e \sim 1$. Along the magnetic field these waves have parallel wavelengths of the order of the device size and they tend to form elongated structures along the magnetic field. We have then a clear separation of length scales between $k_\parallel$ and $k_\perp$ ($k_\parallel \ll k_\perp$), a fundamental property of drift waves in magnetically confined toroidal plasmas that will be fully exploited in the scattering experiments presented in this thesis. Concerning the time scales, these are low frequency modes and their characteristic frequency is smaller than the ion gyro-frequency. Drift waves span a wide variety of modes which, when driven unstable by some mechanism, can result in high transport levels. Due to the relevance of drift waves in present day toroidal confinement experiments, it is important to gain some insight into the physical mechanism driving drift waves unstable. The derivation presented in the next section closely follows that of [50,51] and gives the simplest physical picture of drift wave propagation.

2.2.1 Drift waves

We assume a simplified slab geometry. The basic requisite for the existence of drift waves is the presence of a density or temperature gradient. Assume an electron density gradient ∇n_e is directed in the $\hat{x}$-direction, a background magnetic field B_0 coming out of the board in the $\hat{z}$-direction and a constant electron temperature T_e. In the presence of

a density gradient, electrons (and ions) are subject to a diamagnetic drift velocity

$$v_{\star e} = -\frac{\nabla n_e}{n_e}\frac{T_e}{eB_0} \tag{2.2}$$

Drift waves have small but finite $k_{\|}$ ($cf.$ [40]), which allows electrons to flow along B_0 and establish a thermodynamic equilibrium. Electrons will then satisfy the Boltzmann relation

$$\frac{\delta n_e}{n_e} = \frac{e\phi}{T_e} \tag{2.3}$$

We see that small sinusoidal density perturbations in the $\hat{\boldsymbol{y}}$-direction results in space charge accumulation zones ($cf.$ 2-2). Charge perturbations then give rise to an electric field, which in turn translates to $E \times B$ drifts $v_{E\times B}$ in the $\hat{\boldsymbol{x}}$-direction. The $E \times B$ drift created moves the density perturbations in such a way that a wave propagates in the y-direction. The phase velocity of this wave is the electron diamagnetic drift velocity $v_{\star e}$.

$$\frac{\omega}{k_y} = v_{\star e} \tag{2.4}$$

This simple mechanism is unable to capture a net radial flow of particles (in the $\hat{\boldsymbol{x}}$-direction in figure 2-2). In the present discussion, a small parallel wavenumber $k_{\|}$ allows electrons to move freely along B_0 and the Boltzmann relation 2.3 is fulfilled. In this relation, density n_e and electric potential ϕ are in phase and drift waves are stable. However, there exist a certain number of mechanisms such as electron-ion collisions, Landau damping, electron inertia or inductance, that can limit the parallel electron motion and render drift waves unstable. If electrons are not able to move freely along the magnetic field, a lag between the electron density and the electric potential will set in and a phase shift (δ, assumed small in this description) between the two perturbations will appear. The Boltzmann relation 2.3 can then be modified as follows

$$\frac{\delta n_e}{n_e} = \frac{e\phi}{T_e}(1 - i\delta) \tag{2.5}$$

The small modification in equation 2.5 with respect to the Boltzmann relation 2.3 leads to a modification of the dispersion relation 2.4 as follows

$$\frac{\omega}{k_y} \approx v_{\star e}(1 + i\delta) \tag{2.6}$$

A time variation of $exp(-i\omega t)$ and $\delta > 0$ means that the potential perturbation has acquired an additional phase with respect to the density perturbation. In this situation the drift wave is unstable, and the linear growth rate is given, in this simplistic description, by $\gamma = k_y v_{\star e}\delta$.

The particle flux $\mathbf{\Gamma}$ associated with this drift wave is simply given by the time average of the electron density perturbation δn_e times the $E \times B$ velocity produced by the electric potential perturbation ϕ, as follows $\langle \delta n_e \boldsymbol{v}_{\boldsymbol{E}\times\boldsymbol{B}} \rangle_T = k_y \phi \delta n_e / 2B_0 \sin(\delta)\hat{\boldsymbol{x}}$. We see then that, if $\delta = 0$, fluctuations are adiabatic and no particle transport occurs. In the unstable situation where $\delta > 0$ a radial particle flux in the positive $\hat{\boldsymbol{x}}$-direction (down the density gradient) occurs.

Note we have only dealt here with particle flux. Similar considerations will apply to heat flux $\boldsymbol{Q}$ if we consider temperature perturbations and a temperature gradient. We have considered a simple slab geometry that is usually not applicable in standard tokamaks, even less in spherical tokamaks, and geometrical effects can play a very big role in enhancing/stabilizing this drift wave mechanism.

The interested reader will refer to more complete review papers and manuscripts [40, 50, 51] for more detailed explanations and physical insight.

2.2.2 Relevance of the electron temperature gradient instability in transport.

As we have previously mentioned, theory and experiments suggest that drift waves are responsible for anomalous levels of transport observed in magnetically confined experiments. It would take us too far to derive the different drift wave modes (ITG, TEM, ETG) thought to play the most important role in transport and we will simply give an estimate on the transport that originates from these instabilities.

Gyro-Bohm estimates indicate that the electron thermal diffusivity $\chi_e^{gB} \sim \rho_e^2 v_{te}/L_{Te}$ is a factor of $\sqrt{m_i/m_e}$ smaller than the ion thermal diffusivity $\chi_i^{gB} \sim \rho_i^2 v_{ti}/L_{Ti}$, such that $\chi_e^{gB} \sim \chi_i^{gB}/60$ in deuterium plasmas. This estimate suggests that transport of electron

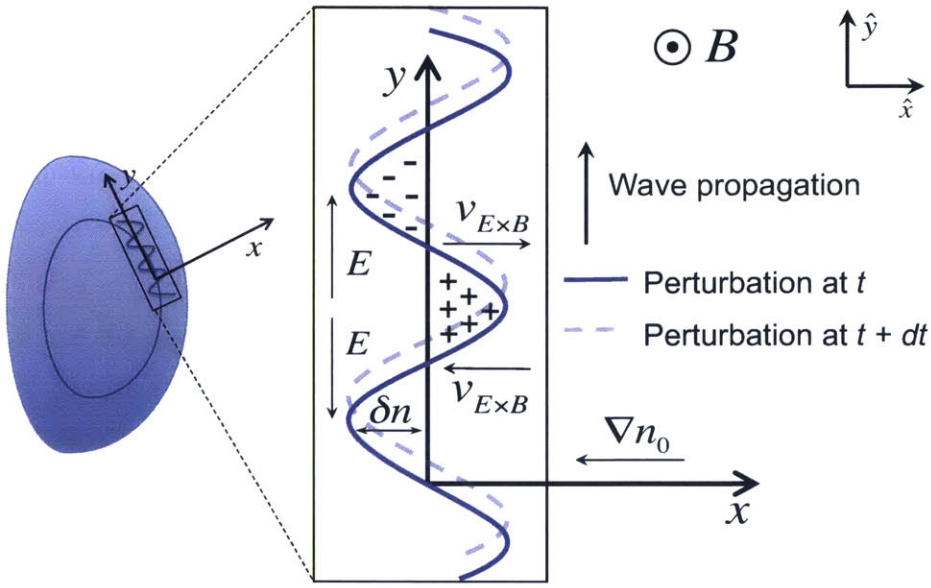

Figure 2-2: Simple physical mechanism for the propagation of a stable drift wave. The toroidal direction is out of the board in this description. The poloidal direction corresponds to the y-axis, and the radial direction corresponds to the x-axis.

energy is not a significant fraction of the total transport in the tokamak and should not be relevant in a reactor.

Nonlinear gyrokinetic simulations predict substantial ion thermal and particle transport due to the TEM mode [55, 56]. Theory and modeling have also predicted that the ITG and TEM modes can give rise to electron thermal transport [40, 53]. Thus, the agreement between theory and simulations on the transport produced by the ITG/TEM modes and the ability of these modes to give rise to electron thermal transport, added to preliminary, small Gyro-Bohm estimates of the electron heat diffusivity χ_e^{gB} (with respect to the gyro-Bohm ion heat diffusivity χ_i^{gB}) all suggest that the ETG mode is not significant to transport. For a long time, the standard model for turbulent transport only included the ITG and TEM modes [53, 57]. Unfortunately, the mentioned predictions cannot account for the experimental levels of electron thermal transport observed in many tokamak plasmas. Electron thermal transport is routinely observed at anomalous levels in present day tokamaks. Spherical tokamaks exhibit neoclassical levels of ion thermal transport [20, 21, 115], but electron thermal transport is never found at neoclassical levels. The problem of electron thermal transport has received much attention in the last decade,

as there is evidence that electron scale turbulence can play an important role in transport levels of tokamak plasmas [103–105]. This thesis is an experimental study of the ETG instability, diagnosed through a micro-wave scattering diagnostic system at NSTX, and it contributes to the understanding of the physical mechanisms of the ETG instability.

2.3 Turbulence and transport in the National Spherical Tokamak Experiment

The spherical tokamak is able to operate in different plasma regimes than those accessible to standard aspect ratio tokamaks. As has been mentioned previously, STs are characterized by a small aspect ratio A, high elongation κ and high magnetic field line curvature, which allows to access different operational space (higher β). Under these conditions, transport processes in spherical tokamaks can be of different nature than in standard tokamaks. In this section we proceed to explain some of these differences.

The toroidal magnetic field in a tokamak plasma (as well as in STs) varies roughly as follows $B_t \sim 1/R$, where R is the major radius location within the plasma. It can be shown by a simple physical argument that the low-field side region of a tokamak plasma (also known as outboard) is subject to an effective acceleration due to the curvature of the field lines and can destabilize a certain number of instabilities (ballooning instabilities). The low field side region of the tokamak is subject to an effective acceleration that tends to destabilize ballooning modes ($cf.$ [29]). For this reason the low-field side region of the plasma is also known as bad-curvature region. On the other hand the high-field side region (inboard) is stable and ballooning instabilities are accumulated on the low-field side. The geometry of STs is optimized to minimize these low-field side instabilities, as can be seen on Fig. 1-6. On a standard tokamak, magnetic field lines wander long distances in the low-field side region of the plasma. Since to a first order approximation plasma particles follow the magnetic field lines, they spend a long time in the low-field side (unstable) region of the plasma. In an ST the curvature introduced in the magnetic field lines shortens the distance that field lines spend on the low-field side region, thus leading to suppression of bad-curvature instabilities and enhanced confinement [19].

In addition to strong field-line curvature, NSTX plasmas exhibit high levels of toroidal flow induced by Neutral Beam Injection (NBI). Toroidal flow in the plasma gives rise to ExB shearing rates that are believed to be responsible for long-wavelength ion-scale (on the ion gyro radius scale ρ_i) turbulence suppression, as routinely observed in NSTX H-mode plasmas [21] and supported by theory and modeling [23, 25]. The ion-scale turbulence suppression observed in NBI heated NSTX H-mode plasmas allows to isolate turbulence and transport studies to the electron thermal channel. The electron thermal transport channel is consistently observed to be the dominant power loss channel in the plasma. Several mechanisms have been recently identified as possible candidates for electron thermal transport. The high beta levels attained in NSTX can destabilize electromagnetic modes such as micro-tearing modes (MT) as discussed in [17, 18], and NBI fast-ion populations destabilize compressional and global Alfvén eigenmodes (CAE/GAE) as discussed in [59, 60]. NSTX has proven to be a valuable laboratory to study electromagnetic and stochastic magnetic field effects on turbulence and transport. Electron temperature gradient driven drift waves (ETG) are small scale turbulence on the electron gyro radius ($k_\perp \rho_e \lesssim 1$) and have also been observed to give rise to experimental levels of electron thermal transport. This thesis describes a particular diagnostic installed at NSTX to diagnose electron scale, high-k density fluctuations by scattering of micro-waves (using a high-k scattering system [92]) that are indicative of ETG turbulence. Previous to the study presented here, several parameters have been predicted and experimentally observed to affect ETG turbulence such as $E \times B$ shearing rates [107,108], reversed shear [109,110] and the electron density gradient [111, 112]. The present thesis develops the study carried out in [111], and further points out the importance of the electron density gradient on high-k electron density fluctuations.

High levels of toroidal rotation in NSTX plasmas is an essential element in achieving high β values. Heating by Neutral Beam Injection (NBI) is a commonly used technique for heating and current drive in tokamak plasmas, and is particularly efficient in producing toroidal flow in the plasma. A simple argument on toroidal angular momentum conservation between fast-ion injected neutrals and plasma particles gives rise to higher angular velocities in STs than in standard high-aspect ratio tokamaks for a given value of heating power. Toroidal rotation is favorable because it can stabilize certain macroscopic instabil-

ities such as edge localized modes (ELMs) and the resistive wall mode (RWM) instability, and can also stabilize certain micro instabilities that are responsible for enhanced transport across the confining magnetic field. Toroidal rotation in NSTX introduces a population of ultra-fast ions whose velocity can exceed the Alfvén speed $v_A = B/\sqrt{\mu_0 \rho}$ (note the magnetic field B is reduced in STs with respect to standard tokamaks, which leads to smaller values of v_A. ρ is the mass density of the plasma) and can resonate with a wide variety of Alfvén waves and destabilize them. These so called Alfvén eigenmodes can lead to particle and energy transport and hence degrade the confinement. However, the study of fast-ion populations is without a doubt of primordial importance towards the development of fusion energy since fusion α-particles and NBI fast-ions in ITER are expected to be unstable to such instabilities. In summary, Alfvén eigenmodes play an important role in NSTX plasmas due to the high values of fast-ion toroidal velocity with respect to the Alfvén velocity (NBI is more efficient in STs and v_A is smaller in STs due to reduced B field). NSTX has arisen as a unique experimental platform for studying the stability and confinement of fast particle populations.

In conclusion, at least four instabilities have been identified as potentially responsible for anomalous electron transport at NSTX: micro-tearing modes (MT [90]), collisionless trapped electron modes (CTEM [45]), electron temperature gradient modes (ETG [46]), and Global Alfven Eigenmodes (GAE [48]). Micro-tearing (electromagnetic), ETG (electrostatic), and GAE modes (Alfvénic) have been correlated with anomalous electron transport in NSTX [18, 48, 49, 59, 60]. Multiple instabilities may be present simultaneously in NSTX plasmas, and isolating the effects of individual instabilities can be difficult. Higher magnetic field and current (as in NSTX-U) will provide access to much lower collisionality allowing suppression of micro-tearing modes [18, 125] (recall that obtaining the low-collisionality confinement scaling is a major research thrust for NSTX-U, as mentioned in 1.4.2). Higher magnetic field will also provide access to reduced fast-ion instability drive and enable the reduction (possibly suppression) of GAE modes [125]. Thus, access to higher magnetic field will enable the ability to control the onset of electromagnetic and Alfvenic modes and to separate the impact of these modes from electrostatic modes.

2.4 ETG and the Jenko critical gradient

The electron temperature gradient instability is a major candidate for explaining anomalous levels of electron thermal transport experimentally observed in some operating regimes. Ion thermal transport however, is observed at neoclassical levels in most NSTX H-mode plasmas, consistent with low-k (ion-scale) turbulence suppression from large $E \times B$ shear driven by neutral beam (NBI) driven plasmas ([20, 21, 115]).

Radial transport of electron thermal heat flux is often modeled with a linear dependence on the electron temperature gradient. In order to account for possible non diagonal transport terms in the electron thermal heat flux, the linear dependence on the electron temperature gradient can be offset by a quantity, which defines a critical gradient $(\nabla T_e)_{crit}$ [116–118], and the expression for the modeled heat flux can be expressed as

$$q_e = n_e \chi_e (\nabla T_e - (\nabla T_e)_{crit}) \tag{2.7}$$

where $\chi_e = 0$ for values of $\nabla T_e < (\nabla T_e)_{crit}$. This formula deserves two important comments: 1) When $\nabla T_e < (\nabla T_e)_{crit}$, the radial electron heat flux predicted by this model is zero. Experimental observations support this conclusion [116, 117]. 2) As its name indicates, the ETG instability is driven by the electron temperature gradient. The critical electron temperature gradient can be also regarded as a threshold for ETG instability.

An analytical expression for the critical gradient was derived in [94] by carrying out many linear gyro kinetic simulations. From now on until the end of this thesis, we will often refer to this expression by the *Jenko critical gradient*. It is given by

$$(R_0/L_{T_e})_{crit} = max \left\{ \begin{array}{c} 0.8 R_0/L_{n_e} \\ (1+\tau)(1.33 + 1.99\hat{s}/q)(1 - 1.5\epsilon)(1 + 0.3\epsilon d\kappa/d\epsilon) \end{array} \right\} \tag{2.8}$$

where $\tau = Z_{eff} T_e/T_i$. In this expression, quantities L_X are defined as $L_X = -\mathrm{d}lnX/\mathrm{d}r$ correspond to typical scale lengths of a quantity X. R_0/L_X are normalized gradients of the quantity X, such as R_0/L_{T_e} and R_0/L_{n_e}, and R_0 is the corresponding flux surface center. Z_{eff} is the effective ion charge, T_e is the electron temperature, T_i is the ion tem-

perature, $\hat{s}$ and q are the magnetic shear and safety factor. ϵ is the inverse aspect ratio. It is important to mention the regime of validity of this formula. The electron temperature critical gradient in equation 2.8 was derived under the assumptions of positive magnetic shear ($\hat{s} \geq 0.2$), low-β and large aspect ratio A. These conditions preclude the use of 2.8 in typical NSTX plasmas, characterized by high-β and small aspect ratio. In this thesis, linear gyrokinetic simulations using the gyrokinetic code GS2 [95] were used to explicitly compute the critical gradient in a particular discharge. Surprisingly, the GS2-computed critical gradient matches the critical gradient formula to a high degree of accuracy. More details will be given in the corresponding section of this thesis.

The Jenko critical gradient formula 2.8 results very useful in practice, as it allows to characterize some of the parametric dependencies of the ETG instability. One direct and obvious dependency is the normalized electron density gradient R_0/L_{n_e}. According to expression 2.8, the electron density gradient is predicted to have a stabilizing effect on the ETG instability. High values of the electron density gradient will make the $0.8R_0/L_{n_e}$ term dominant in expression 2.8, thus it will determine the value of the critical gradient. As we have seen, variations in R_0/L_{n_e} or $\hat{s}$ will give rise to different values of $(R_0/L_{T_e})_{crit}$, thus having an effect on transport, as predicted by 2.7. High enough values of R_0/L_{n_e} will even be able to set the critical ETG to values above the local temperature gradient value. This *should* stabilize the ETG instability. In the past, electron density enhancement and peaked profiles from pellet injection have been reported to improve confinement [119]. More recently, [108, 111] report on the first experimental demonstration of density gradient stabilization of plasma turbulence. In this thesis, we present clear experimental evidence of the electron density gradient stabilization of electron gyro-scale turbulence, and provide arguments to the repetitiveness of this phenomenon. Linear stability analysis carried out with the gyrokinetic code GS2 confirms our observations.

2.5 The gyrokinetic model

The gyrokinetic model is the theoretical framework used to study turbulence in magnetized plasmas. The critical gradient formula 2.8 in the previous section was derived using linear gyrokinetic simulations using the gyrokinetic code GS2 [85, 95]. The equa-

tions solved by GS2 are presented here in a somewhat simplified manner.

We saw in chapter 1 that plasmas such as fusion plasmas are characterized by being weakly coupled ($n_e\lambda_D^3 \gg 1$) which justifies a kinetic description of the plasma based on one-particle distribution functions f_s. The one-particle distribution f_s for species s is such that $f_s(\boldsymbol{r}, \boldsymbol{v}, t)d^3\boldsymbol{r}d^3\boldsymbol{v}$ is the number of species in a volume $d^3\boldsymbol{r}$ located at position $\boldsymbol{r}$ and having a velocity $\boldsymbol{v}$ within a $d^3\boldsymbol{v}$ velocity differential.

The one-particle distribution function satisfies the Boltzmann equation in phase-space $(\boldsymbol{r}, \boldsymbol{v})$

$$\frac{\partial f_s}{\partial t} + \boldsymbol{v} \cdot \nabla f_s + \boldsymbol{a} \cdot \frac{\partial f_s}{\partial \boldsymbol{v}} = C(f_s) \tag{2.9}$$

also known as the Fokker-Planck equation depending on the form of the collision operator C. The collision operator takes into account collisions of species s with all species in the plasma (usually Coulomb collisions, but *nuclear* reactions could also be included on the right hand side in the case of burning plasmas and charged-neutral collisions are also possible). We will not specify here the form of the collision operator, and the reader is referred to [28] for a complete description. The quantity $\boldsymbol{a}$ is the acceleration given here by the Lorentz force

$$\boldsymbol{a} = \frac{e_s}{m_s}[\boldsymbol{E}(\boldsymbol{r}, t) + \frac{\boldsymbol{v} \times \boldsymbol{B}(\boldsymbol{r}, t)}{c}] \tag{2.10}$$

where m_s and e_s are the mass and charge of species s and $\boldsymbol{E}(\boldsymbol{r}, t)$ and $\boldsymbol{B}(\boldsymbol{r}, t)$ are the electric and magnetic field values felt by a particle at position $\boldsymbol{r}$ at a time t. The electric and magnetic fields in the plasma satisfy Maxwell's equations

$$\begin{aligned} \nabla \cdot \boldsymbol{E} &= 4\pi\rho_c \\ \nabla \times \boldsymbol{B} &= \tfrac{4\pi}{c}\boldsymbol{j} + \tfrac{1}{c}\tfrac{\partial \boldsymbol{E}}{\partial t} \\ \nabla \times \boldsymbol{E} &= -\tfrac{1}{c}\tfrac{\partial \boldsymbol{B}}{\partial t} \\ \nabla \cdot \boldsymbol{B} &= 0 \end{aligned} \tag{2.11}$$

where the plasma charge density ρ_c and current $\boldsymbol{j}$ are the sources for Maxwell's equations, and are linked to the distribution function by $\rho_c(\boldsymbol{r},t) = \sum_s e_s \int d^3v f_s(\boldsymbol{r},\boldsymbol{v},t)$, $\boldsymbol{j}(\boldsymbol{r},t) = \sum_s e_s \int d^3v \boldsymbol{v} f_s(\boldsymbol{r},\boldsymbol{v},t)$. We see then that the evolution of the distribution function f_s in eq. 2.9 provides the source terms to Maxwell's equations in 2.11, which in turn impact the evolution of f_s through the Lorentz force. In principle, the full Fokker-Planck-Maxwell equations must be solved to determine f_s.

Although this kinetic description of a fusion grade plasma is fundamentally correct, it is not appropriate from a practical point of view. Analytic solutions to the Fokker-Planck-Maxwell equations are rare, and numerical simulations result extremely time consuming. The full distribution function depends on 7 variables, and assuming steady state reduces the number of variables to 6. Today's most powerful super-computers are not able to numerically solve equations 2.9, 2.11, even in steady state. The theory of gyrokinetics aims to further reduce the number of relevant variables in the distribution function from 6 to 5 (assuming steady state). Numerical codes all around the world (such as GS2) have implemented this *reduction* of equations 2.9 and 2.11 to solve for a 5D distribution function and the electric and magnetic fields. Numerical solutions are now possible.

The basic idea behind gyrokinetic theory is to decouple the fast gyro motion of particles around a background magnetic field from the slower gyro-center dynamics. Time scales associated with turbulent phenomena in magnetically confined plasmas are much lower frequency than the cyclotron frequency Ω_i, such that $\omega/\Omega_i \ll 1$. The gyrokinetic model assumes strongly magnetized plasmas, characterized by $\rho_i/L = \rho_\star \ll 1$, where L is an equilibrium characteristic length scale (typically the minor radius a in tokamak plasmas) and ρ_i is the ion gyro radius $\rho_i = v_{th_i}/\Omega_i$. Parallel length scales are elongated along the background magnetic field $k_\| L \sim 1$ and perpendicular motion scales as the gyro radius $k_\perp \rho_i \sim 1$. We see once more that the assumption $k_\| \ll k_\perp$ made in previous chapters is consistent with the gyro kinetic ordering.

The transformation from a 6D to a 5D dimensional problem is achieved by applying the gyro-center transform as outlined in [80] and shown schematically in Fig. 2-3. The guiding center coordinates $\boldsymbol{R_s}$ are related to the particle position $\boldsymbol{r}$ by $\boldsymbol{r} = \boldsymbol{R_s} - \boldsymbol{v}\times\boldsymbol{b}/\Omega_s$, with $\boldsymbol{v} = v_\| \boldsymbol{b} + v_\perp(\cos\varphi\hat{\boldsymbol{x}} + \sin\varphi\hat{\boldsymbol{y}})$. In the present notation $\boldsymbol{b}$ is the unit vector along the background magnetic field $\boldsymbol{B}$ (subscripted the parallel $\|$ direction), φ is the gyro phase

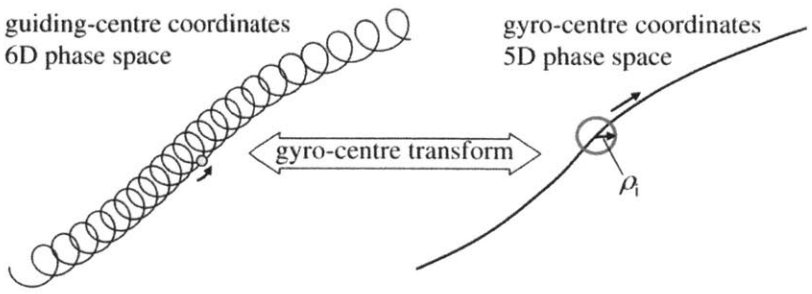

Figure 2-3: Transformation from guiding-center R_s to gyro-center coordinates used in gyrokinetics to reduce the problem for a 6-dimensional one to a 5-dimensional one. Image taken from [79].

and $\hat{\boldsymbol{x}}$ and $\hat{\boldsymbol{y}}$ are the perpendicular coordinates to the background magnetic field (noted with a $\perp$ subscript sign). Roughly speaking, the gyrokinetic equation is solved using a gyro-center coordinate system in which the fast time scale phenomena associated with gyro motion is eliminated, and the gyro phase variable φ (describing gyro motion) is eliminated.

The distribution function f_s and the fields ϕ, $\boldsymbol{A}$ and $\boldsymbol{B}$ are expanded between equilibrium and perturbed quantities, noted with a $\tilde{}$ symbol notation ($f_s = F_{0s} + \tilde{f}_{s1} + ...$, and similarly for $\tilde{\phi}$, $\tilde{\boldsymbol{A}}$ and $\tilde{\boldsymbol{B}}$). Here F_{0s} is the equilibrium distribution function for species s.

Gyrokinetics relies on following ordering assumptions

$$\frac{\omega}{\Omega} \sim \frac{\rho}{L} \sim \frac{\tilde{h}}{F_0} \sim \frac{e\tilde{\phi}}{T} \sim \frac{\tilde{A}_{\parallel}}{B\rho} \sim \frac{\tilde{B}_{\parallel}}{B} \ll 1 \qquad k_{\parallel} L \sim k_{\perp}\rho \sim 1 \tag{2.12}$$

where we omitted the subscript s to denote the species. We have already discussed the time and length scale assumptions related to gyro motion. In equation 2.12, $\tilde{h}$ is the non adiabatic part of the first-order perturbed distribution function defined by $\tilde{h}_s = \tilde{f}_{s1} + \frac{e_s\tilde{\phi}}{T_s}F_{0s}$. The condition $\frac{\tilde{h}}{F_0} \ll 1$ simply assumes that $\tilde{h}$ is a small perturbation to the background distribution function F_0. The following three assumptions on $\tilde{\phi}$, $\tilde{A}_{\parallel}$ and $\tilde{B}_{\parallel}$ assume small perturbations of the electromagnetic fields to background quantities such as temperature T and background magnetic field B.

In depth derivations of the gyrokinetic equations can be found in [79–83]. Here we will simply write the equations solved by the gyrokinetic code GS2. The equations are solved in field-aligned coordinates [84] and using local Miller equilibrium [123]. The

notation is adopted from [82, 85]. The gyrokinetic-Maxwell system of equations is given by

$$\begin{aligned}
&\frac{d\tilde{h}_s}{dt} + v_{\|}\boldsymbol{b}\cdot\nabla\tilde{h}_s + i\omega_d\tilde{h}_s = i\omega_\star\tilde{\chi} - e_s\frac{\partial F_{0s}}{\partial E}\frac{\partial\tilde{\chi}}{\partial t} \\
&\nabla_\perp^2\tilde{\phi} = 4\pi\textstyle\sum_s e_s\int d^3v\left[e_s\phi\frac{\partial F_0}{\partial E} + J_0(\gamma)\tilde{h}_s\right] \\
&\nabla_\perp^2\tilde{A}_{\|} = -\tfrac{4\pi}{c}\textstyle\sum_s\int d^3v e_s v_{\|}J_0(\gamma)\tilde{h}_s \\
&\frac{\tilde{B}_{\|}}{B} = -\frac{4\pi}{B^2}\textstyle\sum_s\int d^3v m v_\perp^2\frac{J_1(\gamma)}{\gamma}\tilde{h}_s
\end{aligned} \tag{2.13}$$

In equations 2.13, the time derivative is equal to $d/dt = \partial/\partial t + (c/B)\{\tilde{\chi}, .\}$ where $\{.,.\}$ is the Poisson bracket defined by $\{U, V\} = \boldsymbol{b}\cdot[\partial U/\partial\boldsymbol{R_s}\times\partial V/\partial\boldsymbol{R_s}]$ and $\tilde{\chi}$ is given by

$$\tilde{\chi} = J_0(\gamma)\left(\tilde{\phi} - \frac{v_{\|}}{c}\tilde{A}_{\|}\right) + \frac{J_1(\gamma)}{\gamma}\frac{mv_\perp^2}{e}\frac{\tilde{B}_{\|}}{B} \tag{2.14}$$

J_0 and J_1 are Bessel functions that take as argument the finite Larmor radius parameter $\gamma = k_\perp v_\perp/\Omega$. The perpendicular curvature and ∇B drifts are incorporated in $\omega_d = \boldsymbol{k}_\perp\cdot\times\left(mv_{\|}^2\boldsymbol{b}\cdot\nabla\boldsymbol{b} + \mu\nabla B\right)/(Bm\Omega)$ and $\omega_\star = cn_o\partial F_0/\partial\Psi$ where n_0 is the toroidal mode number of the perturbation. $\mu = mv_\perp^2/2B$ is the magnetic moment. Note the zeroth-order distribution function $F_{0s} = F_{0s}(E,\Psi)$ only depends on energy $E = mv^2/2$ and flux surface label Ψ.

Equations 2.13 solve self-consistently for the perturbed distribution function of each species. The perturbed fields can be calculated from the perturbed distribution function. Once the distribution function is calculated, gyrokinetic simulations can calculate particle, energy and momentum fluxes by integrating $\tilde{h}_s$ with the right quantities. However, this last step of calculating transport levels using gyrokinetic simulations is only possible when nonlinear effects are properly taken into account in the numerical solution. In the work presented in this thesis we have not attempted to run nonlinear gyrokinetic simulations. Linear gyrokinetic simulations are not able to compute transport levels, but can provide the linear growth rate and real frequenciy of the instability under study, which as we shall

see, can turn to be very valuable information.

Chapter 3

Collective scattering at NSTX

In this chapter we focus on the principles of scattering of electromagnetic waves as a diagnostic tool used to determine relevant quantities of interest in a magnetized plasma. In the first section we give a general introduction to the process of scattering by a plasma, discuss the subtle concepts of incoherent and coherent scattering and some practical applications of scattering for diagnostic purposes in magnetic confinement fusion devices. In the second section we discuss how scattering of electromagnetic radiation can be used to diagnose density fluctuations arising from turbulent processes in the plasma. In the third section we describe the experimental configuration of the high-k scattering diagnostic used at NSTX to detect electron-scale density fluctuations. In the fourth section we present the physical principles towards obtaining highly localized scattering measurements, based on the work carried out by Ernesto Mazzucato at PPPL (*cf.* [68, 113, 114]).

3.1 Collective scattering background

Scattering of electromagnetic radiation is a very powerful method of diagnosis of hot plasma experiments such as fusion plasmas. Most major magnetic confinement fusion experiments world-wide use today some kind of scattering technique for diagnostic purposes. Scattering of electromagnetic radiation is a non-perturbing technique on the plasma, and this is a main advantage when compared to other diagnostic techniques (such as probes). Scattering also has the potential of determining very crucial information about the plasma, such as the electron density and temperature, ion density and temperature, and

electron density fluctuations. In this chapter, I will discuss the scattering process of electromagnetic radiation as a diagnostic technique to measure electron density fluctuations. This technique is a unique diagnostic implemented in the National Spherical Tokamak Experiment (NSTX [11, 12]), and will also be implemented in NSTX-U ([26]).

The physical process of scattering of electromagnetic radiation from plasmas may be understood as follows. The fundamental principles of electromagnetic theory establish that when an electric charge is accelerated, it emits electromagnetic radiation as a result of its acceleration. The scattering process takes place when the acceleration on the electric charge is produced by an electromagnetic wave. When the angular frequency ω of the electromagnetic wave is low compared to the electron rest mass $m_e c^2$, such that $\hbar\omega \ll m_e c^2$, the process is known as Thomson scattering. The scattering processes is primarily dominant for electrons due to their small mass and higher acceleration, giving rise to higher scattered power.

Hot plasmas like fusion plasmas are mainly composed of ions and electrons, and neutral atoms appear in smaller quantities. In the introductory chapter of this thesis we discussed the importance of the Debye length λ_D as a fundamental characteristic scale length in a plasma. The effects of a potential-perturbing charge in a plasma are much shorter-range than in the vacuum. Charges in a plasma tend to redistribute themselves so as to shield the plasma from the electric field generated by the perturbing charge. In thermal equilibrium, perturbing effects of a charge will penetrate into the plasma a distance only of the order of the Debye length λ_D. For distances longer than the Debye length, the charge is screened out by a shielding cloud, and practically nonexistent. To each point charge in the plasma we can associate a Debye sphere of radius λ_D centered on the point charge ($cf.$ Fig 1-3). Charges inside that Debye sphere will be of opposite sign of the test charge, and will be able to interact with it.

In a scattering experiment, an incident electromagnetic wave (typically a laser) interacts with charged particles of the plasma and a scattered wave is radiated. We call $\boldsymbol{k}_i$ the wave number of the incident wave, $\boldsymbol{k}_s$ the wave number of the scattered wave, and $k = |\boldsymbol{k}_i - \boldsymbol{k}_s|$ (the meaning of k will be explained later, but it can be revealed here that we have a conservation law of type $\boldsymbol{k} = \boldsymbol{k}_s - \boldsymbol{k}_i$, $cf.$ Fig. 3.10). The product $k\lambda_D$ measures the correlation between a point charge and its surrounding shielding cloud. The limit

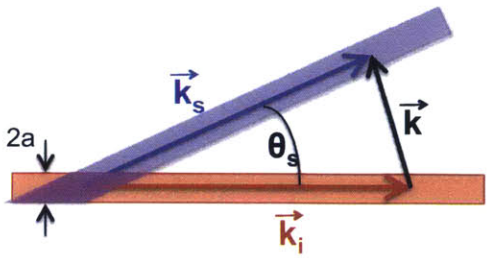

Figure 3-1: Schematic of incident $\mathbf{k}_i$, scattered $\mathbf{k}_s$ and plasma wave-vector $\mathbf{k}$, corresponding to a conservation law of type $\mathbf{k} = \mathbf{k}_s - \mathbf{k}_i$. The incident beam of radiation has a $1/e^2$ radius of a. The intercting volume between the incident and the scattered beams is called the scattering volume. The length of the scattering volume is noted L.

$k\lambda_D \gg 1$ corresponds to the limit of incoherent scattering. In this limit, we are probing length scales in the plasma that are much smaller than the Debye length ($\lambda \ll \lambda_D$) in which electrons are not correlated. Incoherent Thomson scattering (or non collective scattering) thus corresponds to scattering of randomly distributed plasma particles within the scattering volume. Incoherent scattering is employed in the Multi-Pulse Thompson Scattering (MPTS) diagnostic implemented at NSTX. Typical incoherent Thomson scattering systems measure electron density n_e and electron temperature T_e in the plasma. A more detailed description of incoherent Thomson scattering and how to access MPTS data at NSTX data is found in the Appendix.

The limit $k\lambda_D \leq 1$ corresponds to coherent (or collective) scattering. In this regime, we are probing length scales in the plasma that are bigger than the Debye length ($\lambda \geq 2\pi\lambda_D$). As electrons provide shielding to ions and to other electrons in the plasma, the scattering process reveals information about the collective behavior of particles in the plasma. We are able to observe coherent structures and collective motion of plasma particles. Even though it is the electrons that contribute to the shielding (due to their small mass), the shielding on the ions can provide information about the ion temperature, density and flow. Coherent Thomson scattering is being used in tokamaks such as JT60U and Asdex Upgrade for these purposes ([61, 62]). By probing the collective motion of the plasma, coherent scattering is also able to detect coherent structures that can be indicative of turbulent processes. At NSTX, collective Thomson scattering is implemented to measure electron density fluctuations $\tilde{n}_e$ using the high-k scattering diagnostic [92].

3.2 Collective scattering as a turbulence diagnostic

Turbulent fluctuations inside a plasma are characterized by a wavelength λ, or equally a wave-vector k. The ion sound gyro-radius ρ_s is often used as a normalizing quantity for k (ρ_s is calculated using T_e, m_i and the local magnetic field B, as opposed to ρ_i which is calculated using T_i, m_i and B). When the dimensionless quantity $k\rho_s$ is smaller than one, $k\rho_s < 1$, we are dealing with low-k (long wavelength) turbulence such as the ITG or TEM modes we discussed in the previous chapter. When $k\rho_s > 1$, we are dealing with high-k (short wavelength) turbulence. The high-k scattering diagnostic at NSTX-U seeks to measure high-k turbulence, hence its name.

The first experimental confirmation of core turbulence in tokamak plasmas was carried out by E. Mazzucato in the adiabatic toroidal compressor (ATC) [113]. At the time, electron density fluctuations were observed by carrying out spectral analysis of scattered waves. Since then, collective scattering of microwaves continues to play a major role in the analysis of short-scale turbulence in magnetically confined plasmas. The analysis techniques outlined in [113] are very similar to the ones used today in NSTX and soon in NSTX-U, and will be presented in the discussion that follows.

Consider a beam of incident electromagnetic waves with wave vector $\boldsymbol{k}_i$ into a plasma with electron density $n_e(\mathbf{r}, t)$. As the electromagnetic waves propagate in the plasma, they are scattered in *all* directions. Consider a scattered beam of radiation with wave number $\boldsymbol{k}_s$. We are interested to know what is the power that is scattered from the plasma P_s with respect to the incident power of radiation P_i. The full derivation of the scattered power from electron density fluctuations is given in references [65,68,126]. Its expression is the following

$$\frac{d^2 P_s}{d\nu_s d\Omega_s} = P_i r_e^2 L |\mathbf{\Pi} \cdot \hat{\boldsymbol{e}}_{\boldsymbol{i}}|^2 S(\boldsymbol{k}, \omega) \tag{3.1}$$

where r_e is the classical electron radius ($\sim 2\ 10^{-15}$ m), L is the length of the scattering volume ($cf.$ caption in figure 3.10), $\mathbf{\Pi}$ is the polarization tensor and $\hat{\boldsymbol{e}}_{\boldsymbol{i}}$ is the polarization of the incident radiation (direction of the incident electric field). In expression 3.1, ν_s is the value of the scattered frequency and Ω_s is the value of the solid angle (typically the solid angle covered by the collection optics). Equation 3.1 is then an expression

for the scattered power P_s per solid angle Ω_s and per unit frequency ν_s. Note that an incident wave with wave-vector $\boldsymbol{k_i}$ is scattered in all directions according to equation 3.1. The direction of the scattered wave with wave-vector $\boldsymbol{k_s}$ is determined by the fluctuation wave-vector $\boldsymbol{k}$ being probed in the plasma, according to the conservation law $\boldsymbol{k_s} = \boldsymbol{k_i} + \boldsymbol{k}$ ($cf.$ eq. 3.5). It is important to note that $\boldsymbol{k}$ is purely a quantity characteristic of the local turbulence being probed, and it completely determines the propagation of the scattered beam detected by the receiver. Hence, the receiver is oriented beforehand to probe the plasma in a direction where it will be sensitive to fluctuations in the high-k part of the spectrum ($cf.$ Fig. 2-1). In equation 3.1, S is the scattering form factor

$$S(\boldsymbol{k}, \omega) = \frac{|n_e(\boldsymbol{k}, \omega)|^2}{VT} \tag{3.2}$$

and $n_e(\boldsymbol{k}, \omega)$ is given by

$$n_e(\boldsymbol{k}, \omega) = \int_V \int_T n_e(\boldsymbol{r'}, t') e^{i(\omega t' - \boldsymbol{k}\cdot\boldsymbol{r'})} d\boldsymbol{r'} dt' \tag{3.3}$$

where the space integral is taken over the scattering volume V and the time integral over a finite time T. It might be important here to understand the meaning of keeping finite time duration and volume. Note that definition 3.3 does not exactly define a Fourier transform due to finite V and T. The effect of keeping finite V and T is to restrict the wavenumber and frequency resolutions to $\Delta k \sim 1/V^{1/3}$ and $\Delta\omega \sim 1/T$. Density fluctuations are characterized by a typical scale length, known as the correlation length. If the correlation length of density fluctuations is much smaller than the scattering volume length $L \sim V^{1/3}$, then there is no difference between keeping finite V and $V \to \infty$. A similar argument applies to ω and T. For a discussion on the importance of keeping finite Fourier transforms in eq. 3.3, the reader is referred to [65] $pg.$ 295-296.

The scattering form factor S in eq. 3.2 measures the enhancement of the scattered power due collective effects in the plasma (S is directly related to the scattering cross section, $cf.$ equation 3.1 and reference [68]). We see then that the scattered power is proportional to the square of the electron density fluctuations $P_s \propto \tilde{n}_e^2$. We can explicitly calculate the total scattered power from a coherent density fluctuation with amplitude $\tilde{n}_e$ and wavelength λ_i, and it is given by

$$P_s = \frac{1}{4} P_i r_e^2 L^2 \lambda_i^2 \tilde{n}_e^2 \tag{3.4}$$

This equation allows to directly calibrate the electron density fluctuation spectrum of the high-k scattering diagnostic at NSTX, and it provides an estimate to the value of the electron density fluctuations that this system is able to measure. Note that in formula 3.4, P_i, r_e and λ_i are known quantities. The value of P_s detected is calibrated beforehand, so that we're able to obtain a quantitative value of the electron density fluctuations from scattering experiments.

Consider a scattering process between an incident electromagnetic beam of radiation (subscripted i) and a plasma, giving rise to a scattered beam (subscripted s). We call $\boldsymbol{k}_i$ and $\boldsymbol{k}_s$ the wavenumbers of the incident and scattered beams, and $\boldsymbol{k}$ the plasma wavenumber. In diagnosing density fluctuations by collective scattering measurements, $\boldsymbol{k}$ corresponds the wavenumber of the fluctuation that is present in the plasma, and is giving rise to the observed scattering. Typically this fluctuation wave vector is due to some turbulent process in the plasma. At NSTX, the high-k scattering diagnostic measures wavenumbers that are characteristic of the ETG turbulent mode (such that $k_\perp \rho_s > 1$) as we will see. We denote by ω_i and ω_s the angular frequencies of the incident beams, and ω the angular frequency of the fluctuation in the plasma. In a scattering process we have conservation laws between energy and momentum

$$\begin{aligned} \omega &= \omega_s - \omega_i \\ \boldsymbol{k} &= \boldsymbol{k}_s - \boldsymbol{k}_i \end{aligned} \tag{3.5}$$

where $k_i = |\boldsymbol{k}_i| = \omega_i/c$ and $k_s = |\boldsymbol{k}_s| = \omega_s/c$. Fluctuations probed by the high-k system at NSTX are typically low frequency, such that $\omega \ll \omega_i$, which means $\omega_i \approx \omega_s$ and thus $k_i \approx k_s$. In this situation, we have $|\boldsymbol{k}_s - \boldsymbol{k}_i|^2 \approx 2k_i^2 - 2\boldsymbol{k}_s \cdot \boldsymbol{k}_i$, which leads to the well known Bragg condition

$$k = 2k_i \sin(\theta_s/2) \tag{3.6}$$

where θ_s is the scattering angle between $\boldsymbol{k}_i$ and $\boldsymbol{k}_s$ ($cf.$ Fig. 3.10). One of the main advantages of a scattering diagnostic is the ability to produce a frequency and wavenumber

spectrum of the turbulent process under study. The wavenumber and frequency spectrum are the basic signatures a turbulent mode, the ETG mode in our case. Equation 3.6 is a very useful and important relation keep in mind. It relates the wavenumber k of the plasma fluctuations that are being probed with the wavenumber of the incident electromagnetic wave k_i and the scattering angle θ_s. k_i is well determined by the wavelength of the incident beam ($k_i = 2\pi/\lambda_i$) and θ_s is determined by the viewing geometry and the collection optics (Fig. 3.10, 3-2). These two quantities alone are well determined beforehand in a scattering experiment, and they alone completely determine the wavenumber of the measured fluctuations. The high-k scattering diagnostic presented in this thesis uses a 280 GHz incident beam with $\lambda_i \approx 1.07$ mm. Typical scattering angles are $\theta_s \sim 5 - 30^o$, which allows to probe plasma fluctuations with wavenumbers $k \approx k_\perp \lesssim 30$ cm^{-1} (recall $k_\parallel \ll k_\perp$), or $k_\perp \rho_s \lesssim 20$. These values correspond to high-k fluctuations, typical of the ETG instability. Owing to particularly low values of the magnetic field, NSTX is able to diagnose high-k turbulence due to particularly high values of $k_\perp \rho_s$ (typically $k_\perp \rho_s \sim 20$). These values of $k_\perp \rho_s$ are very hard to measure in conventional aspect ratio tokamaks, and makes the high-k scattering system at NSTX the unique diagnostic in the world that measures electron-scale turbulence in tokamak plasmas.

3.3 Experimental configuration of the high-k scattering system at NSTX

Due to the importance of electron scale turbulence and its relation to the problem of electron thermal transport, a 280 GHz microwave coherent scattering system (the high-k scattering system) was implemented on NSTX [92, 127]. This high-k scattering diagnostic measures electron scale density fluctuations on the order of the electron gyro radius $k_\perp \rho_e \lesssim 1$ (ρ_e is the electron gyro-radius). The high-k system has 5 channels available, which allows it measure 5 distinct fluctuation wavenumbers. Each channel 'looks' at the plasma with a different angle. In virtue of the Bragg condition (eq. 3.6), each channel is sensitive to a different fluctuation wavenumber. By detecting fluctuations from the 5 channels, one is able to produce a wavenumber spectrum of fluctuations, as will be shown

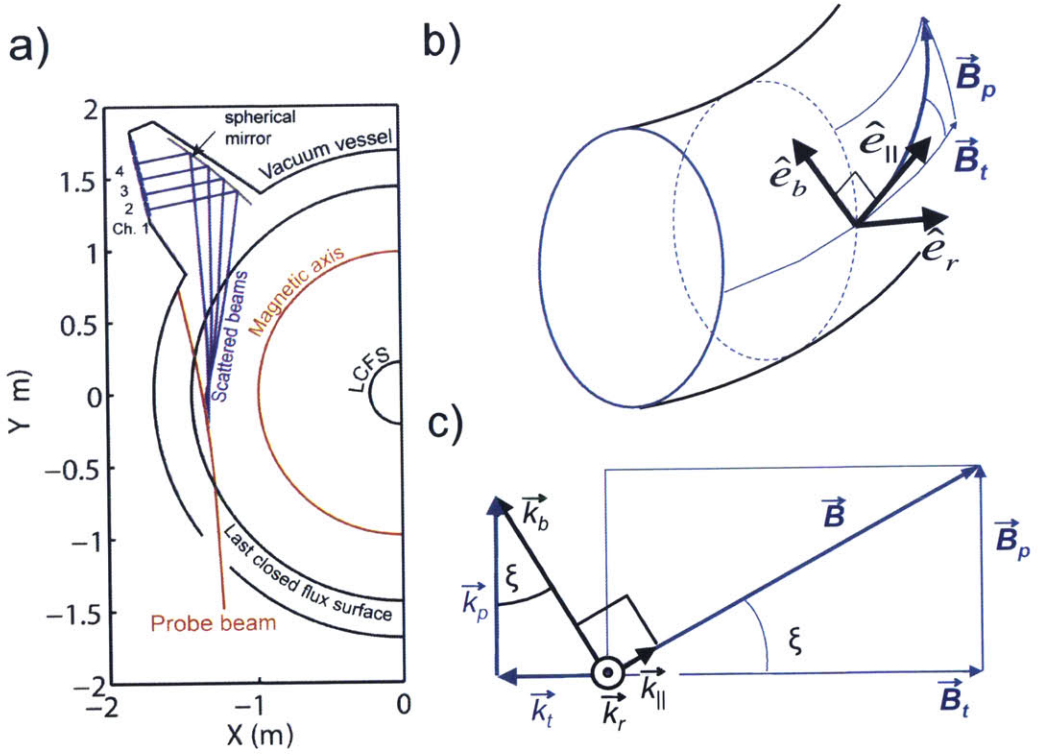

Figure 3-2: $a)$ Experimental configuration of NSTX shot 141767 (view from the top). The probe beam is launched nearly on the midplane. Gaussian beam propagation is calculated using a ray-tracing code. The different channels of the scattering system each measure a different fluctuation wavenumber k. $b)$ Orthonormal basis $(\hat{\boldsymbol{e}}_r, \hat{\boldsymbol{e}}_{\|}, \hat{\boldsymbol{e}}_b)$ used to denote the radial, parallel and binormal components. $c)$ In black are the $(k_r, k_{\|}, k_b)$ components of the fluctuation wavenumber $\boldsymbol{k}$. One can also decompose k into radial, poloidal and toroidal components (k_r, k_p, k_t)(in purple). Both decompositions completely determine $\boldsymbol{k}$. The perpendicular wavenumber $k_\perp$ is given by $k_\perp = \sqrt{k_r^2 + k_b^2}$. In this thesis we work with a decomposition along the basis $(\hat{\boldsymbol{e}}_r, \hat{\boldsymbol{e}}_{\|}, \hat{\boldsymbol{e}}_b)$.

in a later chapter of this thesis. The beam propagation geometry for 4 of the channels is shown in figure 3-2 (beam propagation is carried out using a ray-tracing code).

The propagation of the incident beam is chosen to be nearly on the midplane for a tangential scattering geometry, and is shown in figure 3-2. As we have seen in this chapter, collective scattering theory shows that the detected scattered power P_s is proportional to the mean square of electron density fluctuations $\tilde{n}_e^2$ ($c.f.$ eq. 3.4). The scattering system consists of five collection channels that simultaneously measure five different wave numbers in the range $5 \lesssim k_\perp \lesssim 30$ cm^{-1}. The trajectory of the probe beam and the k response are computed using a ray tracing code. Heterodyne receivers installed on each channel allow one to determine the direction of propagation of the observed fluctuations [92, 127] in the lab-frame. (As we will later see, the detected fluctuation spectrum in the lab-frame is subject to a Doppler shift. Determining the Doppler shift ω_D will allow us to determine the propagation direction of fluctuations in the plasma-frame, $cf.$ the Doppler subtraction section for more details). The wavenumber resolution of the observed electron density fluctuations $\Delta k \ \pm 0.7$ cm^{-1} is well determined by the gaussian beam diameter of the probe beam [127]. A remote control system of launching and receiving optics allows for between shot adjustment. The radial coverage of the detected electron density fluctuations is $R = 106 - 144$ cm, and the radial resolution $\Delta R = \pm 2$ cm. This small radial resolution is the unique feature of the high-k scattering system at NSTX.

The near tangential geometry of the NSTX high-k scattering system forces measured wave vectors to be primarily radial k_r, with a small binormal component k_b satisfying $k_b/k_r \approx 0.2 - 0.3$. Note the binormal direction (along $\hat{\boldsymbol{e}}_b$, Fig. 3-2 b), c)) is perpendicular to $\boldsymbol{B}$ and on the flux surface, and it does not correspond to the poloidal direction (subscripted p in Fig. 3-2.b) and c)). The radial direction (along $\hat{\boldsymbol{e}}_r$, Fig. 3-2 b), c)) is perpendicular to the flux surface ($cf.$ Fig. 3-2, 4-3). Typical values for the parallel wavenumber $k_\parallel$ satisfy $k_\parallel/k_\perp < 0.01$, so we assume here $k_\parallel = 0$. Taking $k_\parallel = 0$, we can map the flux surface components of $\boldsymbol{k}$ from $(k_\parallel, k_b)$ to (k_p, k_t) ($cf.$ Fig. 3-2) as follows

$$\begin{aligned} k_p &= k_b \cos\xi \\ k_t &= k_b \sin\xi \end{aligned} \tag{3.7}$$

Fig. 3-2 clarifies the notation. Additionally, the perpendicular component $k_\perp$ is equal

in this notation to $k_\perp = \sqrt{k_b^2 + k_r^2}$.

It is a common practice to express the measured wavenumber values as dimensionless quantities by using the ion sound gyro-radius ρ_s (ρ_s is computed using local values of electron temperature T_e and magnetic field from equilibrium reconstruction $\rho_s = c_s/\omega_{ci}$ with $c_s = \sqrt{T_e/m_i}$ and $\omega_{ci} = q_i B_0/m_i$).

In this thesis we focus on a particular experiment, shot 141767 in which the scattering system is sensitive to fluctuations taking place at $R \approx 135 - 136$ cm with radial resolution $\Delta R \approx \pm 2$ cm. Channel 1 measures $k_r \rho_s \sim 13 - 17$ and $k_b \rho_s \sim 3 - 4$, which in physical units typically corresponds to $k_r \sim 18 - 25$ cm^{-1} and $k_b \sim 5$ cm^{-1}. As the reader will notice, the high-k system is mostly sensitive to the radial component of the fluctuation wavenumber k_r, and it does not capture the dominant k_b component of ETG turbulence, which is usually a much higher wave number. Most of the figures and results presented in this thesis will come from channel 1 (unless otherwise specified).

For a complete description of the NSTX high-k scattering system, the microwave source and waveguide, the launch and receiving hardware, the quasi-optical beam propagation and the heterodyne receiver, the reader is referred to D.R. Smith's PhD thesis [127] and Rev. Sci. Instruments article [92].

3.4 Detection of short-scale anisotropic turbulence at NSTX

The first evidence of the existence of the turbulent modes driven by the electron temperature gradient (ETG modes) was obtained by Mazzucato first using reflectometry [63] and later repeated using scattering experiments with microwaves [64]. Since then coherent scattering of microwaves from small scale electron density fluctuations in fusion plasmas has struggled to obtain high spatial resolution measurements. Based on the work done by Park in [76, 77] and Devynck *et al* in [75], a proposal for a new high-resolution diagnostic system was approved and installed in NSTX. We present here the principle of spatial localization and wave-number resolution employed in the NSTX high-k scattering system.

As was shown in equation 3.4, the length of the scattering volume L is essential to determining the value of the scattered power P_s (for calibration purposes). The length of

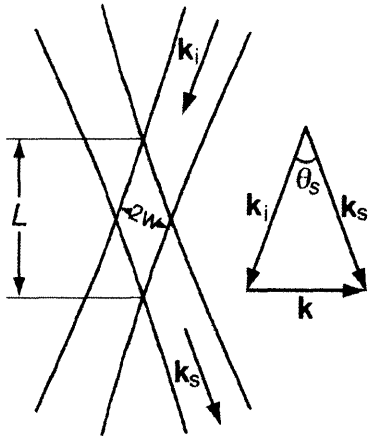

Figure 3-3: Geometry of the incident and scattered beams. The overlap volume is the region of intersection between the two beams. On the left, the measured wavenumber satisfies the conservation relation $\boldsymbol{k} = \boldsymbol{k}_s - \boldsymbol{k}_i$ (image courtesy of [68]).

the scattering volume is a measure of the spatial resolution of the measured fluctuations. A rough estimate of the scattering volume can be obtained by simply considering the overlap volume between the incident and scattered beam, as is shown in figure 3-3. One obtains

$$L/2 = w/\sin(\theta_s/2) = 2wk_i/k \tag{3.8}$$

For typical NSTX parameters $\lambda_i = 1.07$ mm, $w = 2$ cm, $k = 15$ cm^{-1} one finds $L \approx 30$ cm. This very rough estimate of the scattering volume length L can be greatly reduced by making use of our understanding of the turbulence being probed and the magnetic geometry at NSTX.

The previous estimate we found for the scattering volume length (eq. 3.8) did not make any assumption on the type of turbulence being probed, and is only valid for the case of isotropic turbulence (turbulence that is isotropic in all dimensions: along the perpendicular and parallel directions to $\boldsymbol{B}$). However, we already mentioned in the previous chapters that drift wave turbulent modes under investigation in this thesis are highly anisotropic: they form elongated structures along the magnetic field $\boldsymbol{B}$ but have small spatial length scales perpendicular to $\boldsymbol{B}$ (note we do not address here the question of anisotropy in the perpendicular (k_r, k_b) plane). The typical spatial dimension along the magnetic field lines

scales as $k_{\|} \sim 1/qR$ [40] where q is the safety factor and R is the major radius. The particular case of ETG turbulence diagnosed by the high-k scattering diagnostic has a length scale perpendicular to the field lines that scales as $k_{\perp}\rho_e \lesssim 1$. In other words, the turbulence under investigation satisfies $k_{\|} \ll k_{\perp}$. For practical purposes we will assume $\boldsymbol{k} \cdot \boldsymbol{B} = 0$ in the discussion that follows. In other words we will assume that the wave vector of detected fluctuations is purely perpendicular to the local magnetic field (this is indeed a very good approximation, as not only theory [40] but ray-tracing calculations carried out for the particular discharges presented in this thesis provide wave-vector components that satisfy $k_{\|}/k_{\perp} < 10^{-2}$).

The Bragg relation in equation 3.6 gives yet a further constrain on the detected wave-vector k. The two constrains a measured wave-vector $\boldsymbol{k}$ must satisfy can be summarized as follows

$$\begin{aligned} \boldsymbol{k} \cdot \boldsymbol{B} &= 0 \\ k &= 2k_i \sin(\theta_s/2) \end{aligned} \tag{3.9}$$

The first condition of equation 3.9 makes the probed wave-number dependent on the magnetic geometry. As the reader will see, highly curved magnetic field lines will have an impact on the measured $\boldsymbol{k}$, more precisely it will constrain the scattering volume and highly improve spatial resolution. This can be easily understood in the simple case where the propagation of the probe beam and receiving beam is on the midplane, as is shown on figure 3-4. Given a fluctuation wavenumber k, the reader will convince himself that conditions 3.9 are only satisfied at points P_1 and P_2. First, the condition $\boldsymbol{k} \cdot \boldsymbol{B} = 0$ forces P_1 and P_2 as the only possible scattering locations along the incident probe beam, for a given fluctuation wavenumber k. Second, the Bragg condition forces the *direction* of $\boldsymbol{k}$ to be outward at P_1 and inward at P_2 as is shown in figure 3-4. The scattered beam propagates along $\boldsymbol{k_s}$, and its direction of propagation is highly sensitive to the magnetic field line curvature, for a given fluctuation wavenumber k. The red shaded area shows the propagation of the incident microwave beam and the blue shaded area shows the scattered microwave beam that is *actually detected* by the receiver (note that in the configuration presented in Fig. 3-4 the receiver *does not* detect wave-vectors originating from P_1 and P_2, but it is sensitive to a smaller k that gives rise to the scattered beam in blue arriving to the

receiver). It might not be completely obvious in this situation as to why we have so many scattered beams on Fig. 3-4 (in P_1, P_2 and the scattered beam detected by the receiver in blue). We can understand this as follows: as the probe beam propagates through the plasma, it scatters at all locations along the probe beam and in all directions, with an intensity given by equation 3.1. What is unique in a scattering experiment is that the collection optics are oriented in a particular direction that selects a particular wave-vector k at a particular location ($cf.$ Fig. 3-2.a) and 3-4).

An important comment to make here is that the detected wavenumber is purely in the radial direction k_r for the case of midplane propagation. In the actual experiment, the beam propagation of the high-k system at NSTX is nearly in the midplane, but not exactly. As it turns out, slightly off midplane propagation can further improve the spatial localization of the scattering experiment, and at the same time will introduce a finite binormal component k_b in the detected wavenumber $\boldsymbol{k}$. The NSTX high-k scattering diagnostic has adopted an off-midplane probe beam and collection optics, which as we shall see enhances the spatial resolution of the measurement.

The detection efficiency of the receiver is quantified by the instrumental selectivity function F. Following the derivation outlined in [68, 113, 114], we turn to compute the instrumental selectivity function F. We assume a probe beam with Gaussian amplitude profile $A(r_\perp)$ =exp$(-r_\perp^2/w^2)$, where $r_\perp$ is the perpendicular direction to the propagation direction (set by $\boldsymbol{k_i}$ for the incident beam and $\boldsymbol{k_s}$ fo the scattered beam. Note $r_\perp$ is perpendicular to $\boldsymbol{k_i}$ and not to $\boldsymbol{B}$). The beam spectrum is simply the Fourier transform of A and is given by $G(\kappa_\perp)$ =exp$(-\kappa_\perp^2/\Delta^2)$ where $\kappa_\perp$ is the component of the beam wave-vector perpendicular to the propagation direction.

Consider an spherical coordinate system (u, v, t) in which the t-axis is along $\boldsymbol{k_i}$ and θ_s is the angle between $\boldsymbol{k_i}$ and $\boldsymbol{k_s}$, i.e. the scattering angle ($c.f.$ Fig. 3-5.a)). In this coordinate system we can write $\boldsymbol{k_i}$ and $\boldsymbol{k_s}$ as follows

$$\boldsymbol{k_i} = \begin{vmatrix} 0 \\ 0 \\ k_i \end{vmatrix} \qquad \boldsymbol{k_s} = \begin{vmatrix} k_i \sin\theta_s \cos\varphi \\ k_i \sin\theta_s \sin\varphi \\ k_i \cos\theta_s \end{vmatrix} \tag{3.10}$$

which form an angle θ_S as expected, and satisfy $|\boldsymbol{k_s}| = |\boldsymbol{k_i}|$. The idea is to find an

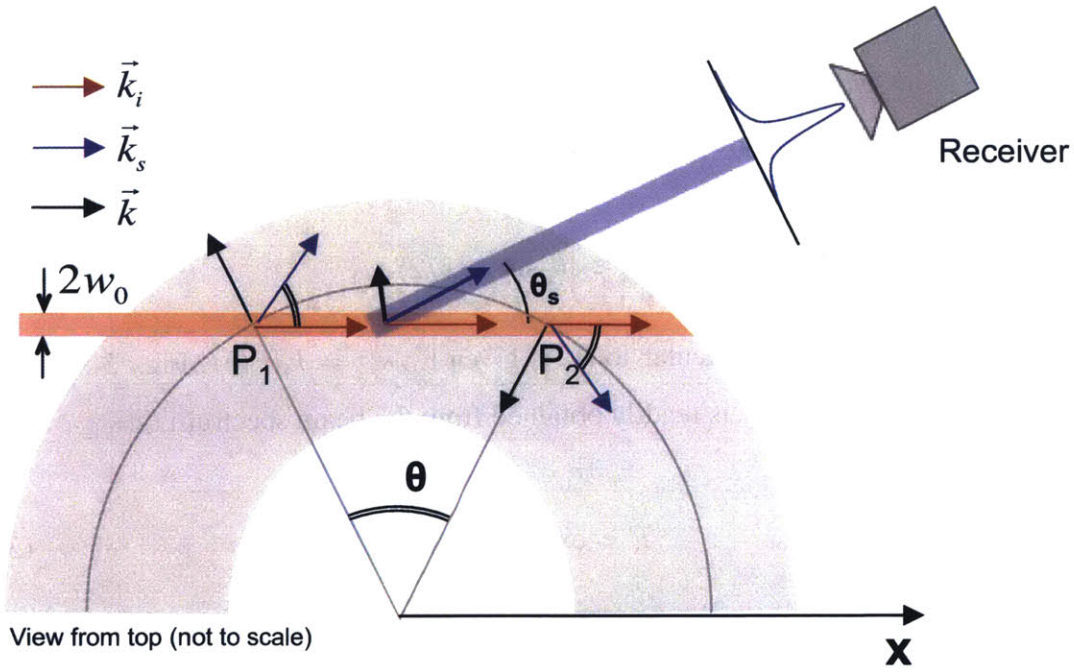

Figure 3-4: Scattering geometry for midplane propagation. Given a wavenumber k, conditions 3.9 are only satisfied at P_1 and P_2. The disparity between the scattered wave-vectors $\boldsymbol{k_s}$ at P_1 and P_2 is due to the curvature of the magnetic field lines, which constricts the scattering volume as shown. The receiver is not sensitive to fluctuation wavenumbers originating from P_1 and P_2, but it is detects a smaller k that in turn gives rise to the scattered beam in blue arriving to the receiver.

expression for $\kappa_\perp$ (value of wavenumber perpendicular to the direction of propagation) as a function of the geometry and other known quantities, such that the beam spectrum $G(\kappa_\perp)$ will provide the collection efficiency given by the instrument selectivity function F. In practice, the scattering receiver is set to point in the direction where efficiency is maximum. Assume this direction is given by $\boldsymbol{k_s}$ (bold blue line in Fig. 3-5.a) and c)). Since the receiver has a finite wavenumber resolution, we refer to any other detected wave-vector by $\boldsymbol{k_s}'$ (see Fig. 3-5.a) and c)).

First, we're interested in determining the angle α between $\boldsymbol{k_s}$ and $\boldsymbol{k_s'}$ assuming $|\boldsymbol{k_s}| = |\boldsymbol{k_s'}|$. The result is readily obtained by a simple dot product $\boldsymbol{k_s} \cdot \boldsymbol{k_s'}/k_i^2$. After simple algebraic manipulations (follow [68, 113, 114]), one finds

$$\alpha^2 \approx 4\theta_s^2 \sin^2(\delta\varphi/2) \tag{3.11}$$

The wavenumber perpendicular to $\boldsymbol{k_s}$ is given by $\kappa_\perp = k_i\alpha$ ($cf.$ Fig. 3-5.c)). The angular collection efficiency is readily obtained from the beam spectrum $G(\kappa_\perp)$

$$F = \exp(-\alpha^2/\alpha_0^2) \tag{3.12}$$

where $\alpha_0 = \Delta/k_i$. Note the Gaussian depence of F with α. The Bragg condition for small scattering angles is written as $k = k_i\theta_s$. Putting everything together yields the instrument selectivity function

$$F = \exp[-(2k\sin(\delta\varphi/2)/\Delta)^2] \tag{3.13}$$

As one might expect, the collection efficiency is maximum at $\alpha = 0$ and decreases as α increases. One can obtain an expression for φ as a function of the local magnetic field using the relation $\boldsymbol{k} \cdot \boldsymbol{B} = 0$ in our particular geometry. The expression is rather cumbersome and not particularly enlightening, so we invite the reader to refer to [68, 113, 114] for all the details. However, it is interesting to point to one important consequence of that derivation. Given a magnetic geometry (from model or EFIT reconstruction) one is able to plot the instrument selectivity function as a function of $\boldsymbol{x}$ (coordinate along the incident probe beam, $cf.$ Fig 3-4). The result is given in figure 3-6 (with permission

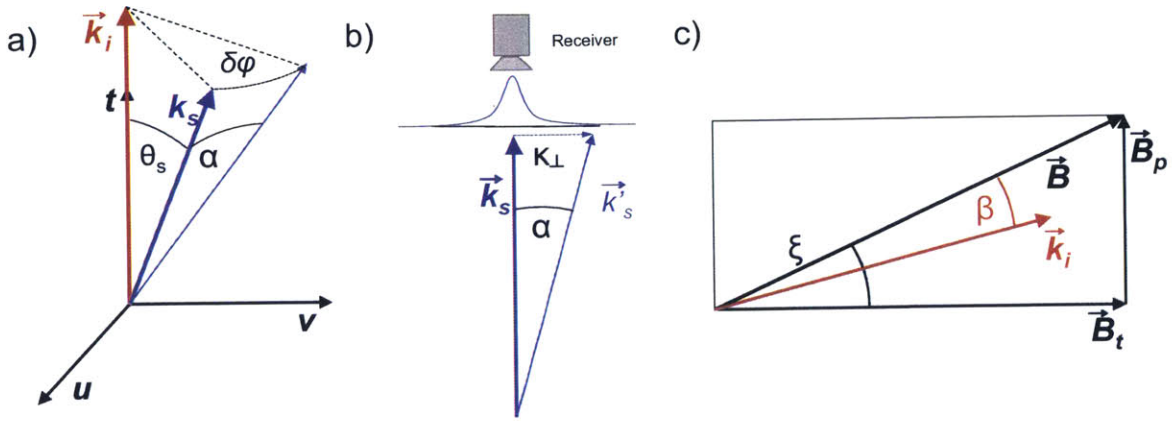

Figure 3-5: a). Orthogonal coordinate system used to derive the instrumental selectivity function F, following [68, 113, 114]. Incident wave-vector $\boldsymbol{k_i}$ in red, and scattered $\boldsymbol{k_s}$ for which efficiency is maximum ($F = 1$) is in bold blue. In thin blue is an additional scattered wave-vector k'_s detected by the receiver, but for which the detected efficiency has decreased with respect to $\boldsymbol{k_s}$ by F =exp$[-(2k\sin(\delta\phi/2)/\Delta)^2]$ b). Geometry within the flux surface at the scattering location. β is the angle formed between the incident wave-vector $\boldsymbol{k_i}$ and the local magnetic field $\boldsymbol{B}$ (note $\boldsymbol{k_i}$ is tangential the scattering location, thus inside the flux surface). c) Definition of $\kappa_\perp$ as the component of the detected wave-vector that is perpendicular to $\boldsymbol{k_s}$. $\boldsymbol{k_s}$ is the wave-vector that produces a maximum efficiency ($F = 1$).

of [68]) for an ITER scenario with major radius 5.2 m and minor radius 2 m [78].

As we mentioned previously, off-midplane propagation can lead to a further enhancement in the spatial resolution of the scattering system. We call β the angle between the local magnetic field $\boldsymbol{B}$ and $\boldsymbol{k_i}$ ($cf.$ Fig. 3-5.c) for clarification). The idea behind this is that the conditions in expression 3.9 become extremely sensitive to the angle β as it gets to smaller values. For midplane propagation, β takes the value of the magnetic pitch angle ξ ($cf.$ Fig. 3-5.c)).

In Fig. 3-6 is plotted the instrument selectivity function F for different values of beta (with permission from Mazzucato [68]). Panel a) corresponds to a value of $\beta = 4.3^o$, b) corresponds to $\beta = 14^o$ and c) corresponds to $\beta = 18^o$. The width of the instrument selectivity function clearly increases with increasing β, meaning that minimizing β is the good strategy to further improve the spatial localization of the scattering measurement. Off-midplane propagation of the probe and scattered beams can achieve this by helping *align* $\boldsymbol{k_i}$ with $\boldsymbol{B}$. For this reason, NSTX adopted off-midplane propagation to implement

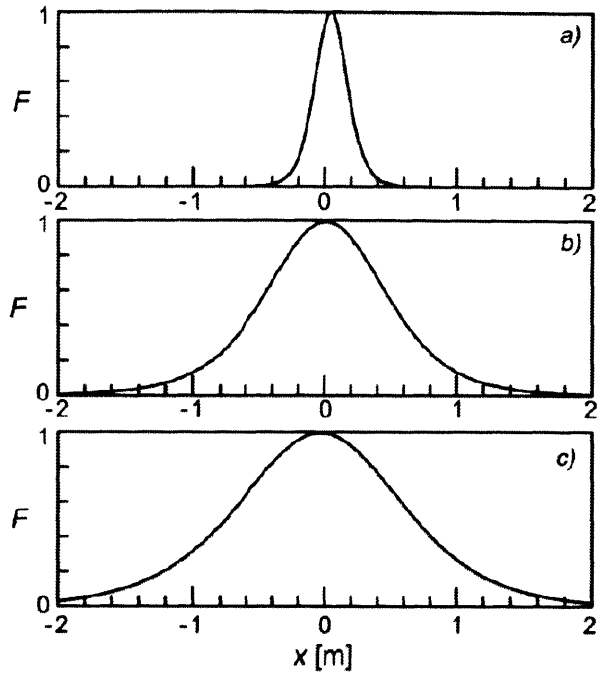

Figure 3-6: Instrument selectivity function F along the x coordinate set by the probe beam propagation direction (Fig. 3-4). *a*) Angle $\beta = 4.3^o$. *b*) Angle $\beta = 14^o$. *c*) Angle $\beta = 18^o$. Note how lower angle β between $\boldsymbol{k_i}$ and $\boldsymbol{B}$ enhances the localization of the measurement.

the high-k scattering diagnostic. The probe beam and collection optics are set to make $\sim 4 - 5^o$ with respect to the midplane.

Concerning the wavenumber resolution, a similar procedure can be carried out. Dropping the condition $|\boldsymbol{k_s}| = |\boldsymbol{k'_s}|$, the instrument selectivity function now takes the form

$$F = \exp[-((k' - k)^2 + 4k'k\sin^2(\delta\varphi/2))/\Delta^2] \tag{3.14}$$

from which the wavenumber resolution $\Delta k = \Delta$ is readily obtained. The radial resolution of the scattering system is limited by the beam width w. For typical NSTX parameters, one finds a wavenumber resolution $\Delta k \approx 2/w \approx 1$ cm^{-1} and a radial resolution of $\Delta R \approx w \approx 2$ cm.

We have shown in this section how high spatial and wavenumber resolution is achieved using the high-k scattering diagnostic at NSTX. This condition makes the NSTX high-k system unique in the world in the detection of highly resolved, short-scale electron density fluctuations. Obtaining a highly localized measurement is crucial to study the

dependencies of the observed density fluctuations on local equilibrium quantities, such as electron temperature and density gradients, safety factor, magnetic shear etc. In this thesis, we report on the influence of the local electron density gradient on the observed electron density fluctuations measured with the high-k scattering system at NSTX.

Chapter 4

Analysis tools

In the previous chapter we described the principles of the scattering process and its use for diagnostic purposes, and we described the experimental configuration of the high-k scattering system at NSTX. In this chapter, we turn to the practical side to provide the reader some useful information necessary to reproduce the work presented in this thesis.

4.1 On-site and remote users from PPPL

The National Spherical Torus Experiment is based at the Princeton Plasma Physics Laboratory (PPPL) in Princeton, NJ. PPPL is a U.S. Department of Energy national laboratory dedicated to fusion energy research. The first thing to do for on-site and remote users is to create a PPPL account. In the framework of the present project and contract between MIT and PPPL I was working under the supervision of Dr. Stanley M. Kaye ($kaye@pppl.gov$), Principal Research Physicist and Head of the NSTX Physics Analysis. Stanley and Lena Scimeca ($lscimeca@pppl.gov$), Technical Assistant at PPPL provided me the information necessary for creating a PPPL account and a UNIX account. In the case where the user will be running TRANSP, it is important to contact Lena or Stanley for establishing TRANSP account.

The previous information is valid both for on-site and remote users. Remote users further need to procure a SecurID token to connect through VPN to the PPPL network (contact Lena for obtaining the SecurID token). Information for VPN access is detailed at $https://vpn.pppl.gov$. Once VPN is established, the user has the choice of connecting

to the PPPL servers by SSH connection or using NoMachine. For both purposes the contact is Ashwini Borkar, Unix/Linux System Engineer at PPPL ($aborkar@pppl.gov$). For downloading NoMachine to a Student Workstation at PSFC-MIT or to a personal/work computer, the user should go to the website $https://www.nomachine.com$.

Once all these connections are established, the user is now able to access NSTX data from the tree and proceed with the physics analysis.

4.2 Accessing NSTX data

In this chapter we refer to *NSTX data* as data stored in the MDSplus tree from each diagnostic corresponding to past NSTX discharges. Typical data used in this thesis comes from the magnetics (Mirnov coils, Rogowski coil, etc.), profile diagnostics (Thomson scattering MPTS, charge exchange CHERS etc.), high-k scattering, and other such as the D_α signal and interferometer for the line-integrated density.

There are several ways to access data stored from past NSTX experiments, and one could choose either options depending on the purpose. One method is using the Web, namely the Web Tools platform provided by PPPL available at $http://nstx.pppl.gov/nstx/Software/$. Web Tools are particularly useful for finding MDSplus signal names as well as for preliminary data visualization and analysis. However the most efficient way to perform a detailed analysis of NSTX experiments is to access MDSplus data directly from UNIX clusters or personal computers without used the Web. The software Matlab was used in the course of this work as a tool to access and perform analysis of NSTX data. Matlab routines $mdsconnect('lark.pppl.gov:8501')$, $mdsopen('activespec', shot)$, $mdsclose$ and $mdsdisconnect$ need to be included in the beginning and the end of each Matlab script to access MDSplus data. The routine $mdsvalue('signalname')$ is also necessary for accessing a particular signal data.

All the Matlab routines used to create the work presented here can be found in my personal directory at PPPL $/u/jruizrui/matlab/myroutines$. A list of the routines used is given in the appendix. Of particular importance in this work is the access of data from the high-k scattering diagnostic, and the subsequent frequency analysis.

The routine $get\_hkdata.m$ provides two arrays of time and raw signal from the high-

k scattering system, for each channel. Measurements presented in this thesis were performed using 7.5 MS/s. The time history of the high-k data was subdivided in Hann windows of 546 μs. Fast Fourier Transforms (FFTs) were calculated within each Hann window using 8192 time samples. The frequency resolution is 1.83 kHz. For each time window with $N = 8192$ time points, the time averaged signal power is

$$P = \frac{1}{N}\sum_{j=1}^{N}|V(t_j)|^2 = \sum_{k=1}^{N}|\hat{V}(f_k)|^2 \tag{4.1}$$

where $\hat{V}$ is the Fourier Transform of V over the time interval of the Hann window

$$\hat{V}(f_k) = \frac{1}{N}\sum_{j=1}^{N}V(t_j)\exp(-2i\pi f_k t_j) \tag{4.2}$$

Using this technique of frequency analysis with Hann windows on raw high-k data one is able to reconstruct figure 4-1. Figure 4-1.a) shows the spectrogram of measured fluctuations channels 1, 2 and 3 of the high-k scattering diagnostic, along with time slices of channel 1 in 4-1.b) as reconstructed using the Matlab routine $plot\_highk\_spec.m$. Fig. 4-1 is plotted in log scale and units are in dB. Note that the high central peak at $f = 0$ is due to stray radiation. The high-k features of electron density fluctuations we focus on are at negative frequencies ($f < 0$).

As was mentioned in the previous chapter, each channel of the high-k scattering system is oriented at a given angle with respect to the incident beam of radiation, which selects a different wavenumber of fluctuations for each channel. The wavenumbers $k_\perp \rho_s$ that each channel is sensitive to are explicit in Fig. 4-1.a).

One additional analysis tool used in this thesis is accessing TRANSP data. TRANSP is a time dependent numerical transport code used in tokamak experiments [71–73]. In the field of transport one is often interested in knowing what are the particle, energy and momentum fluxes within the plasma. It is impossible to calculate these fluxes by inserting probes into the plasma due to the hot conditions of fusion plasmas, and probes can only be implemented at the plasma edge. TRANSP has figured a way to calculate fluxes of particles, energy and momentum based on power balance calculations. TRANSP takes as input experimental profiles along with detailed models of unavailable data from exper-

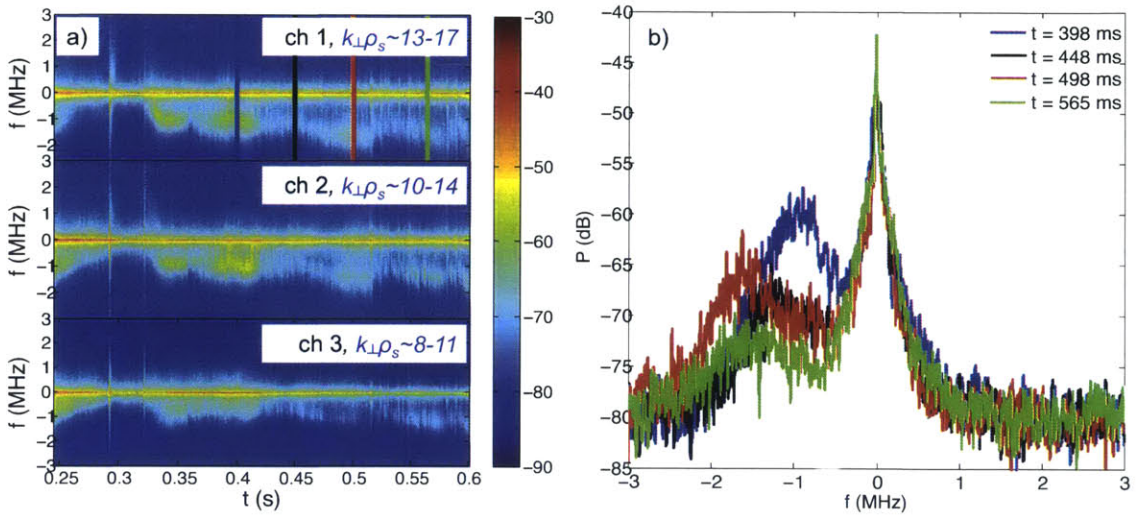

Figure 4-1: $a)$ Spectrogram of high-k density fluctuations from channels 1, 2 and 3 of shot 141767 of the high-k scattering system at NSTX. $b)$ Frequency spectrum of fluctuations corresponding to times as shown on $a)$ by vertical color lines from channel 1. Note $b)$ are simply time slices of channel 1 at the vertical color lines. Each channel is sensitive to a different wavenumber $k_\perp\rho_s$ as is indicated in $a)$.

iments (such as NBI heating absorption by the plasma using Monte Carlo calculations) and neoclassical calculations to solve the power balance equation for all species in the plasma, and arrive to an expression for the particle, heat and momentum diffusivities (transport coefficients corresponding to fluxes). The interested reader is encouraged to turn to references [71–73] for all the details of using TRANSP from the physics foundation to the practical matters. The Matlab routine $get\_transp.m$ is used in this thesis to access TRANSP data from previous TRANSP runs. In particular for shot 141767, we used the transp ID '$B01$' and '$C02$'.

Apart from being able to calculate transport coefficients such as the electron or ion heat diffusivities, TRANSP was of particular use in this thesis to obtain values of the $E \times B$ shearing rate according to the Waltz-Miller definition [74]. TRANSP was also used to obtain values of the radial electric field used in the Doppler shift frequency subtraction (see section on Doppler shift in this chapter). One important use of TRANSP was as being an input file to linear gyro-kinetic simulations using GS2. The use of linear gyro-kinetic simulations is explained in the following section. As will be mentioned, linear gyro-kinetic simulations require experimental profiles from the diagnostics as well as input files

from TRANSP. All these aspects of using TRANSP will be explained in the corresponding sections of this thesis.

The suppression of turbulence by $E \times B$ shear flow is a universal turbulence suppression mechanism in tokamak plasmas [22–24]. The $E \times B$ shearing rate is defined as

$$\gamma_{E\times B} = \frac{(RB_\theta)^2}{B}\frac{\partial}{\partial\psi}\left(\frac{E_r}{RB_\theta}\right) \tag{4.3}$$

The $E \times B$ shearing rate is usually compared with the linear growth rate γ of the particular turbulent mode under study. A general rule of thumb to determine the reduction or suppression of a turbulent mode is the following: when $\gamma \leq \gamma_{E\times B}$, the turbulent mode is said to the reduced or suppressed by $E \times B$ shear [74]. In figure 5-8.a) we plot precisely the linear growth rates of ion-scale and electron scale turbulent instabilities along with the $E \times B$ shearing rate. In that situation we have $\gamma \sim \gamma_{E\times B}$, and we conclude that ion scale turbulence is suppressed by $E \times B$ shear.

Performing a transport analysis using TRANSP and comparing results with nonlinear gyro-kinetic simulations is the next step of the piece of work presented in this thesis. I have not made extensive use of TRANSP in the work presented in this thesis. For making TRANSP runs, obtaining a TRANSP account the reader is referred to $http$: $//w3.pppl.gov/transp/DigiCert/Instructions.html$ and reference [73].

4.3 The gyrokinetic code GS2

GS2 is a δf gyrokinetic code that solves equations 2.13 using a field aligned, flux tube geometry [123]. In the work presented in this thesis, GS2 is run in its linear mode. Linear gyrokinetic simulations are able to provide linear growth rate, real frequency and mode structures of instabilities such as ITG, TEM, ETG, etc. Linear gyrokinetic simulations can also provide critical gradients for instability, following the procedure outlined in [94] and also at the end of this section.

On this work we focus on instabilities having zero radial wavenumber ($k_r = 0$) corresponding to the most unstable mode. The binormal wavenumber k_b (perpendicular to the

magnetic field and inside the flux surface) is a free parameter. In GS2, the convention is that positive real frequencies correspond to propagation in the ion drift direction (ITG) and negative real frequencies correspond to propagation in the electron drift direction (ETG, TEM). Typical wavenumbers for the ITG and TEM instability are $k_b\rho_s \sim 0.3 - 0.8$. Simulations where $k_b\rho_s \sim 0.3 - 0.8$ will be referred to in this thesis as ion-scale simulations. The ETG instability that we focus on this particular work has wavenumbers $k_b\rho_s \sim 20 - 50$, and we will refer to simulations in that particular regime as electron-scale simulations. Drift wave instabilities such as ITG, TEM and ETG exhibit parallel mode structure with even parity for $\tilde{\phi}$ ($cf.$ Fig. 4-2 c)), and micro-tearing mode exhibit parallel mode structures with odd-parity [90]. The linear simulations presented are fully electromagnetic, and include fluctuations in $\tilde{A}_\parallel$, $\tilde{B}_\parallel$ and $\tilde{\phi}$.

GS2 evolves the distribution function in a field aligned, flux tube geometry [84]. The computational domain follows a magnetic field line and can extend several toroidal lengths around the torus. In the perpendicular direction only several gyro radii are simulated. This elongated, or flux tube, computational domain is well suited for calculating properties of local instabilities and transport (if run in the nonlinear mode). The geometry specification used is based on the Miller local equilibrium model [123]. For information concerning the GS2 implementation of the Milller local equilibrium model, please refer to [86, 87].

The simulation time step in GS2 is set by the namelist parameter `delt`. `delt` is normalized to units of a/c_s, where a is the LCFS minor radius and c_s is the sound speed. The parallel spatial grid is determined by `nperiod` and `ntheta`. The number of 2π cells along the field line is 2*`nperiod` -1. The number of grid points per 2π cell is `ntheta` (needs to be an even number). In this work, we set `delt` $= 0.01$ for ion scale simulations and `delt` $= 0.001$ for electron scale simulations, `nperiod` $= 4 - 6$ and `ntheta` $= 48 - 96$.

The energy computational parameters are `negrid`, `ngauss` and `ecut`. `negrid` is the number of energy grid points, `ngauss` is the number of passing pitch angles, and `ecut` is the energy grid points cover. We typically used `negrid` $= 16$, `ecut` $= 2.5$ and `ngauss` $= 10$, and those parameters were not varied in all simulations presented here.

GS2 allows to import numerically generated output from other numerical codes used

in the fusion community. We used output files from the MHD equilibrium reconstruction codes EFIT [88] and LRDFIT [89]. We also used output files from the numerical transport code TRANSP. All this was implemented in the routine $gs2\_submit.m$, and will be detailed in the appendix.

The routine used in this work to create GS2 input files is called $gs2\_submit.m$. Additional numerical parameters related to the type of implicit scheme used can be specified as input in $gs2\_submit.m$. Ion-scale simulations use values `bakdif` $= 0.9$ and `fexpr` $= 0.1$, and electron scale simulations use `bakdif` $= 0.03$ and `fexpr` $= 0.45$. The routine $gs2\_submit.m$ is also able to perform local scans of equilibrium quantities such as the electron temperature gradient. When local scans are computed, all experimental input parameters are set fixed, and only the quantity under scan was varied. The electron temperature gradient is specified as a normalized quantity $R_0/L_{T_e} = R_0|\nabla T_e|/T_e$ where R_0 is the flux surface center (major radius). Note R_0 does not correspond to the major radius location where the gradient is computed.

Following the procedure outlined in [94], local scans on R_0/L_{T_e} were performed to calculate the critical electron temperature gradient using GS2 (Fig. 4-2). We compute the critical electron temperature gradient at a given time and radial location. Given a particular wave number $k_b\rho_s$, linear growth rates γ were computed. Then the value of R_0/L_{T_e} (recall that R_0/L_{T_e} is the driving mechanism for ETG under study here) was varied until we approached marginal stability ($\gamma = 0$) for that given wavenumber. Linear extrapolation provides the value of R_0/L_{T_e} value that saturates γ for *for that particular wavenumber*, and we call that value $(R_0/L_{T_e})^k$. The same procedure was carried out for different wavenumbers, and the corresponding value of $(R_0/L_{T_e})^k$ was recorded. The critical electron temperature gradient $(R_0/L_{T_e})_{crit}$ is defined as the minimum value among the previously recorded $(R_0/L_{T_e})^k$ values, such that $(R_0/L_{T_e})_{crit} = \min_k\{(R_0/L_{T_e})^k\}$. This value will indeed saturate the linear growth rate associated to *all* the wavenumbers calculated, and will correspond a stable ETG regime.

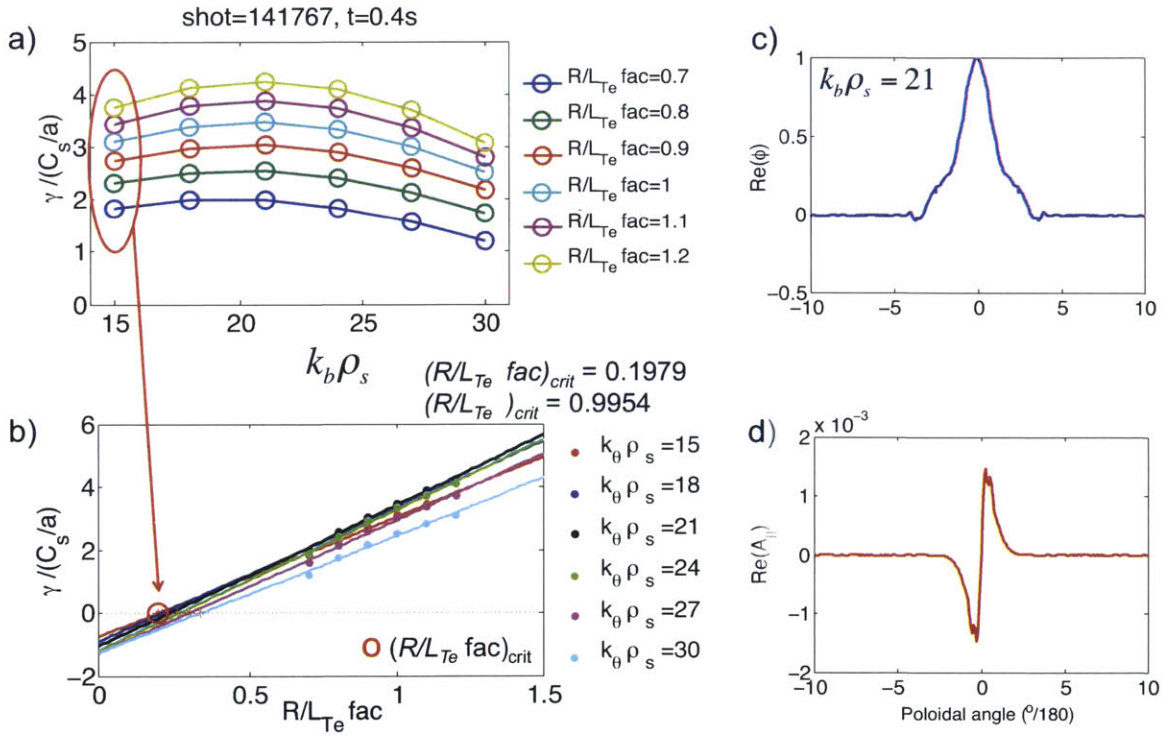

Figure 4-2: $a) = b)$ Schematic representation of the procedure carried out to numerically compute a critical electron temperature gradient R_0/L_{T_e}. This procedure is explained in full detail in [94]. $c)$ Electric potential perturbation $\tilde{\phi}$ for shot 141767, t = 400 ms, R = 135 cm and $k_b\rho_s = 21$. $d)$ Parallel vector potential perturbation $\tilde{A}_{||}$ for the same values as in $c)$. Note how the real part of $\tilde{\phi}$ is an even function of poloidal angle.

4.4 Ray tracing calculations

Scattering experiments are a vey powerful method of diagnosing turbulent fluctuations in magnetized plasmas. Unlike other diagnostic techniques, multichannel scattering experiments are able to provide a wavenumber spectrum of the measured fluctuations, as we will see in the next chapter. It is thus very important to determine the correct value of the wavenumber k detected by each channel of the scattering diagnostic. As was mentioned already in this chapter, the measured wavenumber can be determined beforehand by the Bragg condition $k = 2k_i \sin(\theta_s/2)$. However, this can only provide an estimate of the measured k. Morover, as well will see shortly, inhomogeneities present in the plasma such as density gradients give rise to refraction of the incident probe beam of radiation, thus complicating the calculation of the the measured wavenumber. Simple analytical calculations are thus not appropriate for these kind of experiments and one has to rely on numerical simulations to access the measured wavenumber, and this is the purpose of ray tracing calculations.

Refraction effects of the incident beam of radiation are usually small, but certainly not negligible and result to be very important in the implementation of the high-k scattering diagnostic. In addition to determining the measured fluctuation wavenumber by the scattering system, ray tracing is also able to account for refraction, calculate the exact scattering location, the scattering volume, and the instrument selectivity function, which will be defined later.

The conditions of validity for ray tracing can be summarized in a simple condition $|\nabla k| \ll k^2$, known as the geometrical optics approximation or WKB approximation. This approximation states we can treat each individual ray of incident radiation as independent from the rest of the rays. The geometrical optics approximation also states that the wavelength of the incoming radiation does not vary significantly as the wave propagates a distance of one wavelength in the plasma (weakly inhomogeneous medium), and one could easily convince himself of this fact $|\nabla k| \ll k^2 \Leftrightarrow 2\pi|\nabla\lambda| \ll 1$. We can calculate the value of $|\nabla k|/k^2$ easily in the following way. By definition of the refractive index $N = ck/\omega$, we have $|\nabla k|/k^2 = c/\omega(\nabla N/N^2)$. As a rough estimate, we can approximate $N \approx 1$ (high frequency limit and far from cutoffs). The gradient

∇N is easily approximated by $\nabla N \approx \alpha/L$, where α is the refraction angle given in appendix ($\alpha \approx n_e L/2n_c L_{n_e}$). Thus we find the expression $|\nabla k|/k^2 \approx c\alpha/\omega L$. Taking typical values for $\alpha \approx 10^o$, $L \sim 1$ m, $f = 280$ GHz and $c = 3.10^8$ m/s, we find $c\alpha/\omega L \sim 10^{-4}, 10^{-5} \ll 1$ and the geometrical optics approximation is well suited here for ray tracing calculations in typical NSTX plasmas.

The starting point of ray-tracing calculations is the dispersion relation of waves in the plasma. The cold plasma model is well suited in NSTX like plasmas for frequencies far from cutoffs and resonances. Typical time scales of the plasma are the electron plasma frequency $f_{pe} = \omega_{pe}/2\pi = 1/2\pi(n_e e^2/m_e\epsilon_0) \approx 60$ GHz ($n_e \sim 5.10^{19}\text{m}^{-3}$), the electron cyclotron frequency $f_{ce} = \omega_{ce}/2\pi = 1/2\pi(eB_0/m_e) \approx 14$ GHz ($B_0 \sim 0.5$T). The electron thermal speed $v_{te} = \sqrt{2T_e/m_e}$ takes the value $\approx 10^7$ m/s ($T_e \sim 0.5$ keV). In comparison, the probe frequency of the incident beam is 280 GHz. At this frequency we're in the high frequency regime, far from cutoffs and resonances ($\omega \gg \omega_{pe}, \omega_{ce}$), and the cold plasma model is valid. In fact, $\omega/k_\parallel v_{te} \gg 1$ for typical $k_\parallel \ll k_\perp \approx 2.10^3$ m^{-1}, and $k_\perp^2 \rho_e^2 \ll 1$, where $\rho_e = v_{te}/\omega_{ce} \approx 10^{-4}$ m. We proceed then to compute the cold plasma dispersion relation in the high frequency regime, known as the Appleton-Hartree dispersion relation ($c.f.$ for example reference [65] for a proper derivation).

Maxwell's wave equations in $(\omega, \boldsymbol{k})$ space can be written as

$$\boldsymbol{k} \times (\boldsymbol{k} \times \boldsymbol{E}(\omega, \boldsymbol{k})) + \frac{\omega^2}{c^2}\boldsymbol{\epsilon} \cdot \boldsymbol{E}(\omega, \boldsymbol{k}) = 0 \tag{4.4}$$

where $\boldsymbol{\epsilon}$ is the dielectric tensor and $\boldsymbol{E}$ is the wave electric field. Note that here $\boldsymbol{k}$ does not correspond to the plasma fluctuation wavenumber but to the probe beam wavenumber denoted as $\boldsymbol{k_i}$ in the rest of this thesis. In this section we will make no use of the plasma fluctuation wavenumber and we will simply use $\boldsymbol{k}$ to denote the probe beam wavenumber.

We use the orthonormal coordinate system $(\hat{\boldsymbol{e}}_x, \hat{\boldsymbol{e}}_y, \hat{\boldsymbol{e}}_z)$ obtained from the previous $(\hat{\boldsymbol{e}}_r, \hat{\boldsymbol{e}}_\parallel, \hat{\boldsymbol{e}}_b)$ by the correspondence $\hat{\boldsymbol{e}}_x = \hat{\boldsymbol{e}}_r$, $\hat{\boldsymbol{e}}_y = \hat{\boldsymbol{e}}_b$ and $\hat{\boldsymbol{e}}_z = -\hat{\boldsymbol{e}}_\parallel$. We call θ the angle between $\boldsymbol{k}$ and the background magnetic field $\boldsymbol{B_0}$. From equation 4.4 we can define the dispersion tensor

$$\boldsymbol{\mathcal{D}} = \boldsymbol{kk} - k^2\boldsymbol{I} + \frac{\omega^2}{c^2}\epsilon = \frac{\omega^2}{c^2}\begin{pmatrix} S - N^2\cos^2\theta & -iD & N^2\cos\theta\sin\theta \\ iD & S - N^2 & 0 \\ N^2\cos\theta\sin\theta & 0 & P - N^2\sin^2\theta \end{pmatrix} \tag{4.5}$$

with $N = ck/\omega$ and S, P, D are Stix parameters given by

$$\begin{aligned} S &= 1 - \textstyle\sum_s \frac{\omega_{ps}^2}{\omega^2 - \Omega_s^2} \\ D &= \textstyle\sum_s \frac{\Omega_s \omega_{ps}^2}{\omega(\omega^2 - \Omega_s^2)} \\ P &= 1 - \textstyle\sum_s \frac{\omega_{ps}^2}{\omega^2} \end{aligned} \tag{4.6}$$

Where the sum $\sum_s$ is performed over the species present in the plasma. Note the definition of $\Omega_s = q_s B/m_s$ includes the sign convention: $\Omega_e < 0$ and $\Omega_i > 0$. The condition $\boldsymbol{\mathcal{D}} \cdot \boldsymbol{E} = 0$ provides a non trivial solution for $\boldsymbol{E}$ provided $\mathcal{D} = det(\boldsymbol{\mathcal{D}}) = 0$, which gives the dispersion relation

$$AN^4 - BN^2 + C = 0 \tag{4.7}$$

where $A = S\sin^2\theta + P\cos^2\theta$, $B = (S^2 - D^2)\sin^2\theta + PS(1+\cos^2\theta)$, $C = P(S^2 - D^2)$. Equation 4.7 is quadratic in N^2, and can be solved to provide two solutions

$$N^2 = \frac{B \pm \sqrt{B^2 - 4AC}}{2A} = \frac{2C}{B \mp \sqrt{B^2 - 4AC}} \tag{4.8}$$

which ultimately gives rise to the Appleton-Hartree dispersion relation [65,66]

$$\mathcal{D} = 1 - N^2 - \frac{X(1-X)}{1 - X - \frac{1}{2}Y^2\sin^2\theta \pm \sqrt{(\frac{1}{2}Y^2\sin^2\theta)^2 + (1-X)^2Y^2\cos^2\theta}} = 0 \tag{4.9}$$

where $X = \omega_{pe}^2/\omega^2$ and $Y = \Omega_e/\omega$. This dispersion relationship describes O-Mode (+ solution) and X-Mode (- solution) at perpendicular propagation $\theta = \pi/2$ and parallel propagation at $\theta = 0$.

We can now write the ray equations using the dispersion relation 4.9. They are given by [66,68]

$$\frac{d\boldsymbol{r}}{d\tau} = \left.\frac{\partial \mathcal{D}}{\partial \boldsymbol{k}}\right|_{\mathcal{D}=0} \qquad \frac{d\boldsymbol{k}}{d\tau} = -\left.\frac{\partial \mathcal{D}}{\partial \boldsymbol{r}}\right|_{\mathcal{D}=0} \tag{4.10}$$

where τ parametrizes the distance along a ray. Given initial conditions $(\boldsymbol{r}(0), \boldsymbol{k}(0))$ one is able to compute the ray trajectory $(\boldsymbol{r}(\tau), \boldsymbol{k}(\tau))$ by integrating equations 4.10. Equations 4.10 are a system of 6 nonlinear ordinary differential equations, which can be solved numerically using the Runge-Kutta method [69]. Equations 4.10 typically have to be solved in toroidal geometry which introduces an axisymmetry condition around the toroidal angle ϕ. For more details on solving the ray equations in toroidal geometry, the reader is referred to [68, 70].

The ray-tracing code used during the course of this work was implemented by Y. Ren and D. R. Smith, both currently scientists from the Princeton Plasma Physics Laboratory. The matlab routines used in this thesis are all noted in the appendix. For more details about the ray tracing code used in this work, the reader is referred to D. R. Smith's PhD thesis [127].

4.5 Doppler shift frequency subtraction

Neutral Beam Injection heated (NBI) plasmas at NSTX exhibit high levels of toroidal rotation. It was emphasized in section 1.4.3 the importance of achieving high levels of toroidal rotation in tokamak plasmas. For the purposes of our scattering experiment, high levels of toroidal rotation in tokamak plasmas have a direct consequence on measured frequency spectra of fluctuations.

One important feature of the type of turbulence that is being diagnosed is the propagation direction of the measured frequency of fluctuations in the plasma frame. We need to distinguish the laboratory frame (*lab frame*), which is the frame of reference where the scattering signal is detected and the plasma frame in which the plasma is stationary. We mentioned in the previous section that heterodyne detection is able to determine the propagation direction of the detected electron density fluctuations in the *lab frame*. However, to access the propagation direction in the *plasma frame*, we need to perform the Doppler subtraction of the measured signal.

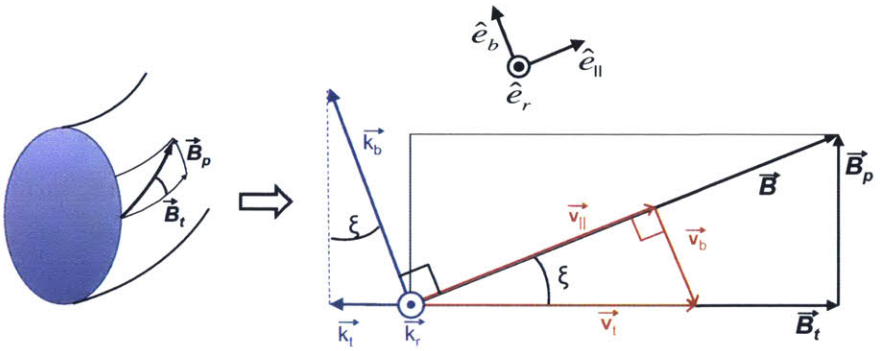

Figure 4-3: Flux surface geometry used to compute the Doppler shift frequency ω_D of fluctuations introduced due to toroidal rotation. We use the orthonormal coordinate system $(\hat{\boldsymbol{e}}_{\boldsymbol{r}}, \hat{\boldsymbol{e}}_{\|}, \hat{\boldsymbol{e}}_{\boldsymbol{b}})$ in the radial, parallel and binormal directions respectively. ξ is the magnetic pitch angle.

In order to explain the direction of propagation of fluctuations in the plasma frame, it is important to define the geometry we will use. Consider the orthonormal coordinate system $(\hat{\boldsymbol{e}}_{\boldsymbol{r}}, \hat{\boldsymbol{e}}_{\|}, \hat{\boldsymbol{e}}_{\boldsymbol{b}})$ on figure 3-2 and 4-3. We call ω_p the frequency of fluctuations as they were emitted in the plasma frame, and ω_{lab} the frequency of fluctuations as we detect them in the lab frame. The general Doppler shift frequency can be proven to be $\omega_D \approx k_t v_t$ (the reader is encouraged to turn to the appendix for a proper derivation of this expression). Due to toroidal rotation, measured frequencies of fluctuations in the lab-frame will be Doppler shifted from plasma-frame fluctuation frequencies. The lab frame frequency of detected fluctuations is related to the plasma frame frequency of fluctuations by

$$\omega_{lab} = \omega_p + \omega_D \approx \omega_p + k_t v_t \tag{4.11}$$

Theory states that plasma fluctuations due to the electron temperature gradient (ETG) instability propagate along the electron diamagnetic drift direction $v_{D_e} = \nabla p_e \times \boldsymbol{B}/en_eB^2$ in the plasma frame [97, 98] (due to toroidal geometry and other effects, the propagation phase speed for ETG instability fluctuations is not exactly v_{D_e}, but it is on the same direction as v_{D_e}). We call these *electron modes*. Conversely, fluctuations due to the ion temperature gradient (ITG) instability propagate in the ion diamagnetic drift direction $v_{D_i} = -\nabla p_i \times \boldsymbol{B}/en_iB^2$, and we call them *ion modes*. Determining experimentally the propagation direction of the measured fluctuations *in the plasma frame* is thus an

important step towards resolving the kind of turbulent mode that is being diagnosed with the high-k scattering system.

As we have mentioned, $\omega_D \approx k_t v_t$, where the toroidal direction is along $\boldsymbol{B_t} = B_t \hat{\boldsymbol{e}}_{\boldsymbol{t}}$. Here $\hat{\boldsymbol{e}}_{\boldsymbol{t}} = \cos(\xi)\hat{e}_{\|} - \sin(\xi)\hat{\boldsymbol{e}}_{\boldsymbol{b}}$ ($cf.$ Fig. 3-2 and 4-3). It is important to mention here that the direction of the plasma current I_p in NSTX plasmas is along $-\hat{\boldsymbol{e}}_{\boldsymbol{t}}$, $i.e.$ in opposite direction to the toroidal magnetic field $\boldsymbol{B_t}$. Looking at the toroidal component of v_{D_e} and v_{D_i} we have

$$\begin{aligned} \boldsymbol{v_{D_e}} \cdot \hat{\boldsymbol{e}}_{\boldsymbol{t}} &= \frac{|\frac{dp_e}{dr}|B\sin\xi}{en_eB^2} = \frac{|\frac{dp_e}{dr}|B_p}{en_eB^2} > 0 \\ \boldsymbol{v_{D_i}} \cdot \hat{\boldsymbol{e}}_{\boldsymbol{t}} &= -\frac{|\frac{dp_i}{dr}|B_p}{en_iB^2} < 0 \end{aligned} \tag{4.12}$$

From these expressions, we can conclude that *plasma co-rotation* ($i.e.$ along $-\hat{\boldsymbol{e}}_{\boldsymbol{t}}$) *shifts the lab-frame frequency spectrum of electron and ion modes towards the* ***ion direction***. This is an important statement. Having access to toroidal rotation data allows us to determine the propagation direction (in the plasma frame) of the measured frequency spectrum by the high-k scattering system.

We would like to comment here on the value of v_t used in this thesis to compute the Doppler shift frequency $f_D \approx k_t v_t / 2\pi$. Our final goal is to compare Doppler subtracted, plasma frame frequency of fluctuations with real frequencies given by linear gyrokinetic simulations using GS2. Linear gyrokinetic simulations are carried in the plasma frame. The toroidal velocity of the plasma frame is related to the radial electric field through the radial force balance equation

$$E_r = -\frac{\nabla p_i}{Z_i n_i e} + v_t B_p - v_p B_t \tag{4.13}$$

where the subscripts p, t indicate respectively the poloidal and toroidal components of the velocity v and magnetic field B. Under usual conditions in tokamak plasmas, the poloidal velocity term $v_p B_t$ is negligible. In regions outside the pedestal or internal transport barriers, the pressure gradient term $\nabla p_i / Z_i nie$ is also negligible and the toroidal velocity term usually the dominant term. In the particular plasma discharge presented in this work, the poloidal velocity term typically accounts for a $\sim 5\%$ contribution to E_r

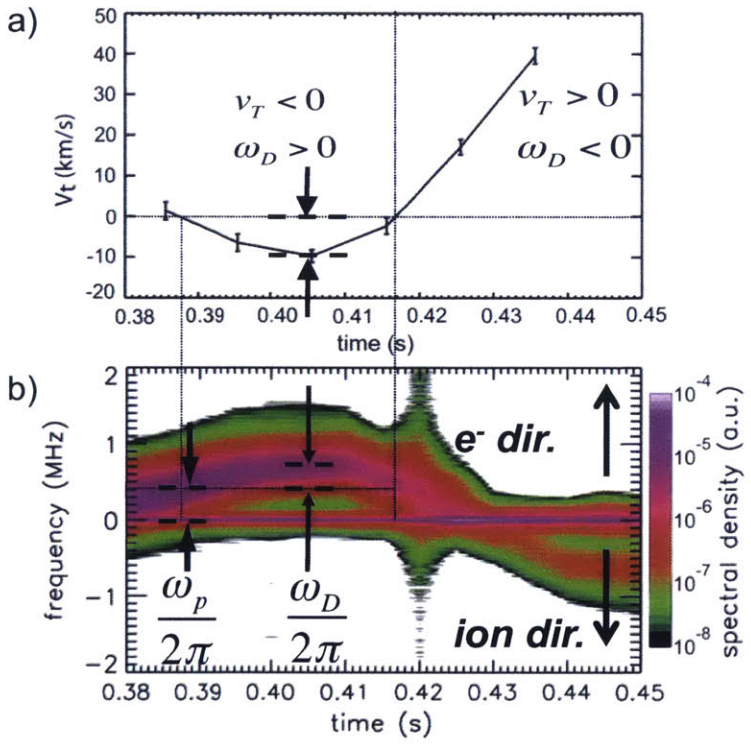

Figure 4-4: a) Plasma toroidal velocity suffers a change in sign in the time of interest. b) High-k frequency spectrum of fluctuations. Note how the change in v_t translates into a shift in the measured lab frame frequency of fluctuations. This example shows how plasma co-rotation produces a Doppler shift in the ion diamagnetic drift direction. Figure adapted from [67].

and the pressure gradient term typically has a $\sim 15\%$ contribution. Based on this approximation, the radial electric field in GS2 is calculated using uniquely the toroidal velocity term, which sets the toroidal velocity of the plasma frame in which GS2 calculations are performed. TRANSP simulations can provide the value of all terms in equation 4.13. The toroidal velocity is then computed as follows $v_t = E_r/B_p$. This is the definition used in this thesis to compute the Doppler shift frequency f_D.

Figure 4-4 provides an example of the Doppler shift effect on measured fluctuation spectra. In this particular discharge, the plasma toroidal velocity was subject to a change in direction, and the effect was observed on the high-k frequency fluctuation spectrum. Positive toroidal velocity corresponds to plasma co-rotation and negative toroidal velocity corresponds to plasma counter-rotation. At $t \sim 0.39$ s, the toroidal velocity is close to 0 ($v_t \sim 0$) and the plasma frame frequency of fluctuations $f_p = \omega_p/2\pi$ can be read directly from the frequency spectrum in 4-4 .b) as indicated (note how at $t \sim 0.417$ s the toroidal velocity $v_t \sim 0$ and a similar frequency is observed from the high-k spectrum in 4-4.b)). Recall that fluctuations measured by the high-k system propagate in the electron diamagnetic drift direction. This defines the ion drift direction as being in the $f < 0$ direction. As time increases, at $t \sim 0.4 - 0.41$ s, the toroidal velocity has a negative value, and the frequency spectrum from the high-k is shifted in the electron direction ($v_t < 0$ corresponds to plasma counter-rotation). At later times $t > 0.42$ s, the toroidal velocity becomes positive which corresponds to a Doppler shift in the ion diamagnetic drift direction as was previously argued. Figure 4-4 was adapted from [67] to provide a clear example of the toroidal velocity effect on measured lab frame high-k frequency spectra.

On the next chapter will be presented the experimental observation of the density gradient effect on high-k electron density fluctuations. In particular, we will present a systematic method of obtaining the plasma-frame frequency of high-k fluctuations, and how this will provide an experimental dispersion relation of the measured frequency spectra. This will then be compared to real frequency of fluctuations calculated using the gyrokinetic code GS2 and the influence of the electron density gradient will be highlighted.

Chapter 5

Experimental observation and analysis of density gradient effects on high-k turbulence

The influence of electron density gradient on ETG turbulence was first pointed out by Y. Ren *et al.* in [111]. The normalized local electron density gradient (R_0/L_{n_e}) was reported to stabilize longer wavelength modes ($k_\perp \rho_s \lesssim 10$), and reduced the plasma effective diffusivity. Nonlinear ETG gyrokinetic simulations carried out for the same NSTX discharge 140620 were reported in [112], and showed in fact that the fractional electron heat flux was greatly reduced at lower ETG wavenumbers and at the same time shifted towards higher wavenumbers.

This chapter presents the measurements, ray-tracing calculations and linear stability analysis carried out with the gyrokinetic code GS2 for a particular NSTX NBI-heated H-mode plasma discharge. Experimental measurements show an absence of electron density fluctuations detected by the high-k system when the experimental temperature gradient is at marginal stability levels with the critical gradient for ETG (eq. 2.8). Measurements also show how the local value of the electron density gradient affects the amplitude of the electron density fluctuations when the experimental temperature gradient surpasses the critical gradient linear threshold. According to the ETG critical gradient ($cf.$ eq. 2.8), the discharge presented here is electron density gradient dominated. The electron density

gradient is shown to experimentally have a big impact on density fluctuation data. Linear gyrokinetic simulations using GS2 show that ETG is indeed unstable at the scattering location and the local electron density gradient is shown to have a big impact on the linear growth rate and real frequencies from GS2. Experimentally measured wavenumbers corresponding to peak values of the wavenumber fluctuation spectrum exhibit a positive correlation with the local electron density gradient. Wavenumber values corresponding to peak linear growth rates from GS2 simulations also show a correlation with the local electron density gradient and a similar behavior is observed from linear gyrokinetic simulations and experimental measurements. The plasma frame frequencies of fluctuations obtained by Doppler subtraction of lab frame frequencies from the high-k system exhibit a correlation with the local electron density gradient, and a similar trend is observed with real frequencies calculated by GS2. The similar behavior between density fluctuations measured by the high-k system and linear gyrokinetic simulation results shows a good connection between experiment and simulation.

5.1 Experimental study of electron density gradient dependence

Here we focus on a particular experiment of an NBI-heated NSTX H-mode plasma (shot 141767). The general characteristics of the discharge are shown in Fig. 5-1. The NBI heating power is stepped down from a maximum value of 6 MW to a value of 2 MW, and stays constant during the time range of interest. The time range of interest is chosen to be $t \gtrsim 0.3$ s (see vertical dashed line in black in Fig. 5-1), corresponding to a time span where MHD activity (indicated in the low-frequency Mirnov signal) is quite low (Fig. 5-1.d)). Plasma current is ramped up until a time slightly before 0.3 s, when it reaches the flat top phase, followed by a controlled current ramp-down phase between 0.4 s to 0.45 s from a value of ~ 1.1 MW to ~ 0.9 MW. An ELM-like feature is observed at $t \approx 0.292$ s from the D_α and low-f Mirnov signal followed by a smaller ELM-like feature at $t \approx 322$. Low-f Mirnov fluctuations quiet down after the big ELM event at $t \approx 292$ ms (black dashed line), and high-k electron density fluctuations start to develop

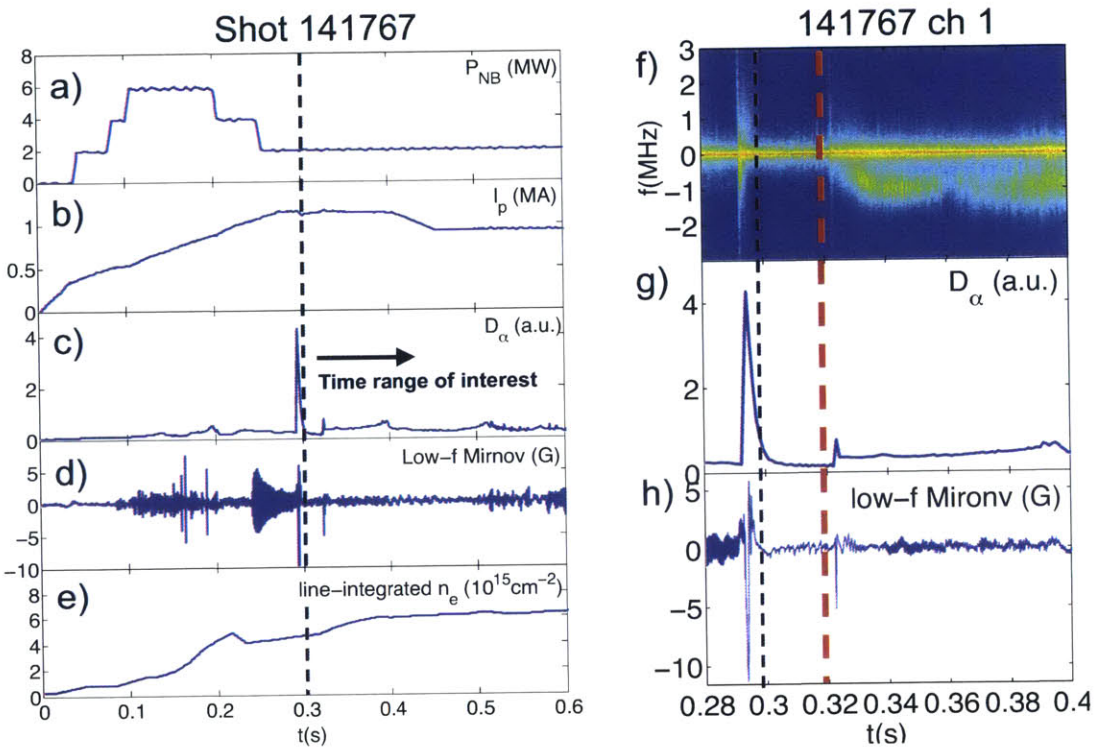

Figure 5-1: General characteristics of shot 141767. $a)$ NBI heating power P_{NB} (MW), $b)$ plasma current I_p (MA), $c)$ D_α emission (not calibrated), $d)$ low frequency magnetic fluctuations (G), $e)$ line-integrated density $\overline{n}_e$ (10^{15} cm^{-2}), $f), g), h)$ Zoom on fluctuation spectrogram, D_α signal and low-f Mirnov signal showing the onset of ETG fluctuations after a small ELM feature at $t \approx 322$ ms (red dashed line).

after the small ELM event at $t \approx 322$ (red dashed line in Fig. 5-1.g)). The line-integrated electron density (Fig. 5-1.e)) and toroidal magnetic field ($B_t \sim 4.6 - 5$ kG) are fairly constant during the time range of interest. Preceding 0.3 s the low-f Mirnov signal shows high MHD activity. High amplitude MHD activity will contaminate the scattering system fluctuation measurements, thus we will only focus on the time range after t = 0.3 s where MHD activity is observed to be weak.

In figure 5-2.a) is plotted the frequency fluctuation spectrogram from channel 1 of the high-k system, along with time slices showing the frequency spectrum of fluctuations at $t = 398, 448, 498, 565$ ms in 5-2.b). The colored lines in 5-2.a) correspond to the analysis times in 5-2.b). Radial profiles of electron density and temperature are shown in 5-2.c) and 5-2.d). The electron temperature gradient is the driving mechanism for ETG turbulence, and it does not significantly change at the scattering location. The electron density

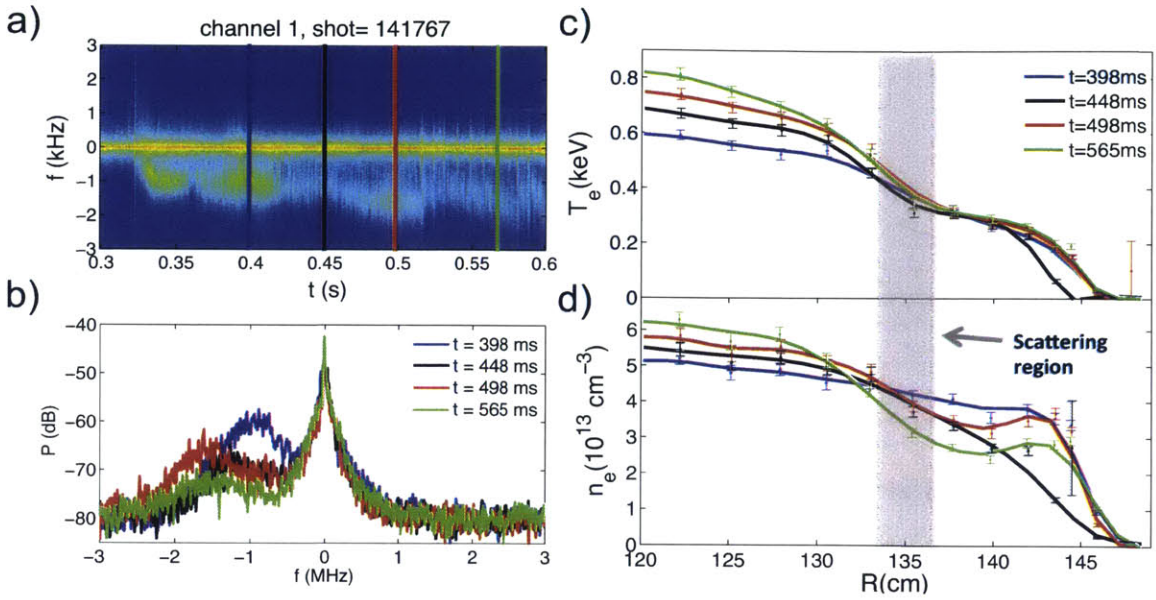

Figure 5-2: $a)$ Frequency fluctuation spectrogram from channel 1. $b)$ Fluctuation spectrum from channel 1 at times corresponding to the vertical color lines in $a)$. $c) - d)$ Electron temperature and density profiles.

gradient undergoes a large change in the scattering region. The electron density gradient is weak at $t = 398$ ms ($R_0/L_{n_e} \approx 1.5$), and it corresponds to a time where the fluctuation level on 5-2.a) and 5-2.b) is highest. As the electron density gradient increases at later times, the fluctuation amplitude decreases and a correlation can be established. Note how the electron density gradient is highest at $t = 565$ ms ($R_0/L_{n_e} \approx 6.4$), and the fluctuation amplitude is lowest at that time. This qualitative preliminary correlation between the electron density gradient and density fluctuations from the scattering diagnostic will be explored.

Theory suggests that the electron density gradient can have a stabilizing influence on the ETG turbulent mode. As its name indicates, the ETG drift wave turbulent mode is driven by the electron temperature gradient. Theory suggests that the relevant driving parameter for ETG is η_e [98–100]

$$\eta_e = L_{n_e}/L_{T_e} = (n_e \nabla T_e)/(T_e \nabla n_e) \tag{5.1}$$

The parameter η_e incorporates temperature gradient as driving mechanism, but also takes into account the density gradient value in the denominator. Since ∇n_e is in the de-

nominator of eq. 5.1, the electron density gradient can be seen as a stabilizing mechanism for ETG. This is also in agreement with the critical gradient formula derived by Jenko *et al* [94] and shown in eq. 2.8. For reference, we reproduce the critical gradient formula once more

$$(R_0/L_{T_e})_{crit} = max \left\{ \begin{array}{c} 0.8R_0/L_{n_e} \\ (1+\tau)(1.33+1.99\hat{s}/q)(1-1.5\epsilon)(1+0.3\epsilon d\kappa/d\epsilon) \end{array} \right\} \quad (5.2)$$

where $\tau = Z_{eff}T_e/T_i$. The first term very closely relates to the η_e parameter, except for the factor 0.8 of little relevance here. Once more, the electron density gradient term appears as a stabilizing mechanism. High enough values of R_0/L_{n_e} will raise the critical gradient value, thus having a stabilizing influence on turbulence. The first term in 5.2 corresponds to the slab limit of ETG, since R_0 is simplified out when $(R_0/L_{T_e})_{crit} = 0.8R_0/L_{n_e}$. The second term in eq. 5.2 corresponds to a toroidal term, where the complexity of the geometry is introduced by the inverse aspect ratio ϵ, elongation κ and magnetic geometry through $\hat{s}/q$.

We want to highlight the condition under which this formula was derived, and presumably most valid. The electron temperature critical gradient in equation 5.2 was derived under the assumptions of positive magnetic shear ($\hat{s} \geq 0.2$), low-β and large aspect ratio A (*cf.* [94]). These conditions *preclude* the use of eq. 5.2 for typical NSTX plasmas, characterized by high-β and small aspect ratio. To test the applicability of the Jenko critical gradient formula, we computed explicitly the critical gradient using GS2, following the procedure outlined in the previous chapter.

The Jenko critical gradient value (eq. 5.2) is calculated for the particular discharge under study here, and is shown on Fig. 5-3. The two terms in the *max* function are also plotted in blue (density gradient term) and green (toroidal term). The *local* values of electron density n_e and electron temperature T_e present in the Jenko critical ETG formula are measured with the Multi Point Thomson Scattering diagnostic at NSTX (MPTS, [121]). Ion temperature T_i and effective ion charge Z_{eff} are measured with the Charge Exchange Recombination Spectroscopy system (CHERS [120]). Magnetic shear $\hat{s}$, safety factor q and inverse aspect ratio ϵ are obtained using LRDFIT (LR circuit model with Data Fitting

capabilities) equilibrium reconstructions constrained by magnetic pitch angle measurements from the Motional Stark Effect (MSE) diagnostic [122]. All these experimental values are *local* values, meaning they are computed at the scattering location.

In figure 5-3, triangles show the critical gradient computed using GS2. The first comment to note here is that the GS2 computed critical gradient agrees with the Jenko critical gradient for most part of the discharge. This rather surprising result allows us to use the Jenko critical gradient to estimate the linear threshold for instability in this particular discharge. From now until the end of this thesis, we will assume eq. 5.2 is correct and applicable in our case of study. It can also be noted from Fig. 5-3 that the electron density gradient term in blue is dominant for most part of the discharge. According to formula 5.2 (which we assume correct according to our previous discussion), the local value of the electron electron density gradient completely determines critical electron temperature gradient value, which will affect ETG turbulence as predicted by theory. High enough values of R_0/L_{n_e} will be able to raise the critical gradient linear threshold above the experimental temperature gradient value, and thus stabilize turbulence. This motivates the study of the electron density gradient effects on ETG turbulence diagnosed by the high-k scattering diagnostic. The characteristics of this particular discharge are very favorable for the study of the electron density gradient influence on high-k fluctuations, since this discharge is density gradient dominated as can be seen from Fig. 5-3.

We want to compare the critical gradient value at the scattering location with actual density fluctuation data from the high-k system. In figure 5-4 is plotted the total scattered power from channel 1 (integrated spectrogram in frequency from Fig. 5-2.a)) along with the experimental and critical electron temperature gradient at the scattering location (black and red respectively in Fig. 5-2.b)), and the difference between the two in Fig. 5-2.c). Recall that the total scattered power is directly proportional to electron density fluctuation amplitude according to equation 3.1 ($P_{\text{tot}} \sim \int (\delta n_e/n_e)^2 d\nu$), and we will use both terms interchangeably in the following discussions.

For early times ($t \lesssim 0.33$ s), the experimental temperature gradient is at marginal stability levels with respect to the critical gradient, and no high-k fluctuations are observed at that time in Fig. 5-4.a). Note the high spike at $t \sim 292$ ms from 5-4.a) corresponds to a powerful ELM event and does not correspond to ETG fluctuations. As the critical gradient

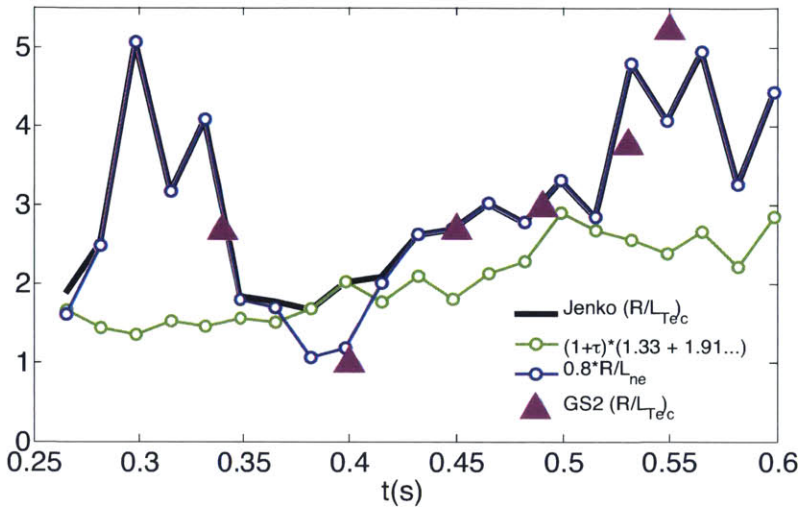

Figure 5-3: Jenko critical gradient (black) and both terms in the max function (green and blue curves). Triangles show the critical gradient explicitly computed using GS2, following the procedure outlined in the previous chapter.

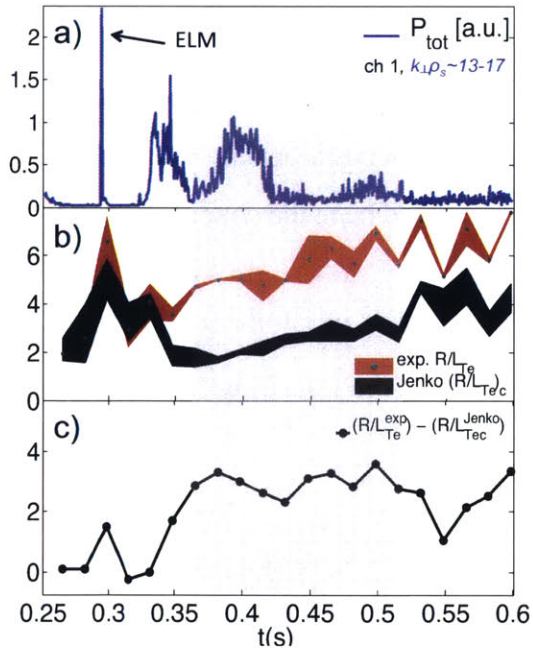

Figure 5-4: $a)$ Total scattered power from channel 1 of the high-k scattering system. The total scattered power is found integrating the frequency spectrogram in Fig. 5-2.$a)$ in frequency. $b)$ Experimental (red) and critical temperature gradient (black) at the scattering location. $c)$ The difference $R/L_{T_e}^{exp} - R/L_{T_eC}^{crit}$ indicates whether ETG is unstable or not, and should correlate to the presence of electron density fluctuations.

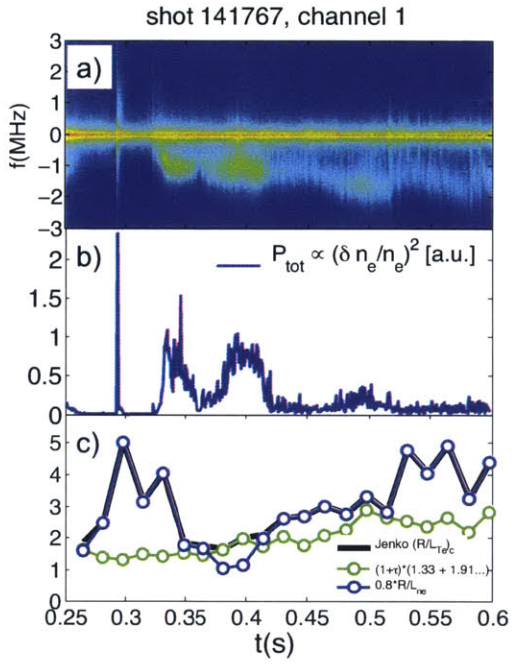

Figure 5-5: $a)$ Fluctuation spectrogram from channel 1. $b)$ Total scattered power from channel 1 of the high-k scattering system. $c)$ Jenko critical gradient (black) and both terms in the max function (green and blue curves).

suddenly decreases at $t \sim 330$ ms, $R/L_{T_e}^{exp} - R/L_{T_eC}^{Jenko}$ increases in Fig. 5-4.c), and ETG becomes unstable. At that time, electron density fluctuations start to develop in Fig. 5-4.a). An important comment should be made concerning this figure. During the time span $t \sim 0.36-0.53$ s (grey time panel), $R/L_{T_e}^{exp} - R/L_{T_eC}^{Jenko}$ has a very similar value. However, this very similar value of $R/L_{T_e}^{exp} - R/L_{T_eC}^{Jenko}$ gives rise to a very different fluctuation amplitude in 5-4.a). This suggests the following form of the modelled turbulent electron radial heat flux

$$q_e^{turb} = \chi_e^{GB} f(\nabla n_e, \hat{s}, \gamma_{E\times B}, ...)(R_0/L_{T_e} - R_0/L_{T_e}^{crit}) \tag{5.3}$$

such a model contains a linear threshold for instability given by $R_0/L_{T_e}^{crit}$ (which can depend on various plasma parameters as shown by eq. 5.2), as well as a nonlinear dependence of q_e^{turb} on other plasma parameters. We aim to show in this work the nonlinear dependence of such a function f on the local electron density gradient.

In figure 5-5 is shown the influence of the electron density gradient on the fluctuation amplitude of the high-k scattering system. We argued from figure 5-4 that the difference

$R/L_{T_e}^{exp} - R/L_{T_eC}^{Jenko}$ determines the presence of electron scale density fluctuations. We saw how at $t \sim 0.33$ s, $R/L_{T_e}^{exp} - R/L_{T_eC}^{Jenko} > 0$ and fluctuations develop at the same time. Looking at Fig. 5-5.c), we see that the sudden decrease of $R/L_{T_eC}^{Jenko}$ at $t \sim 0.33$ s is due to a big decrease of the density gradient (term in blue). This experimental remark is in agreement with dependence of the linear threshold on the density gradient given by equation 5.2. ETG remains unstable and high-k fluctuations persist until the end of the discharge ($cf.$ Fig. 5-4).

The electron density gradient term ($0.8R_0/L_{n_e}$, blue curve in Fig. 5-5.c)) is dominant for most part of the time range of interest (t > 0.3 s). The fast broadband ELM event seen at $t \approx 292$ ms from the total scattered power (Fig. 5-5.b)) precedes a high increase in the electron density gradient, as can be seen from the $0.8R_0/L_{n_e}$ term increase on panel 5-5.c). These high levels of R_0/L_{n_e} make it the dominant term in the Jenko critical gradient ($260 \lesssim t \lesssim 330$ ms), and set the critical gradient to marginal stability levels with respect to the experimental temperature gradient value: ETG is marginally stable during that time and no high-k scattered power is detected. As the electron density gradient drops at $t \approx 330$ ms, the critical gradient drops well below the experimental temperature gradient ($cf.$ Fig. 5-4.b)), and ETG is unstable. At that time, high-k fluctuations (Fig. 5-5.a)) start to develop and the total scattered power increases. In fact, ETG remains unstable and high-k fluctuations persist until the end of the discharge (Fig. 5-5.a)). Between $360 \lesssim t \lesssim 410$ ms, the electron density gradient term becomes subdominant (blue curve on Fig. 5-5.c)), and an enhancement of high-k fluctuations is observed in figure 5-5.a) and b). As the electron density gradient becomes the dominant term in the Jenko formula at $t \sim 420$ ms, high-k fluctuations appear to mitigate. Recall that $360 \lesssim t \lesssim 410$ ms corresponds to a time span where $R/L_{T_e}^{exp} - R/L_{T_e}^{crit}$ is practically constant ($cf.$ gray panel in Fig. 5-4.c)). The previous comments support the claim of a nonlinear dependence of q_e^{turb} on the local density gradient ∇n_e as suggested in eq. 5.3. After a sudden increase in the electron density gradient at $t \approx 520$ ms, high-k fluctuations appear to mitigate once more (Fig. 5-5.a) $-$ b)). The current ramp-down phase from $t = 400$ and $t = 450$ ms (Fig. 5-1).b) does not appear to have a big impact on the critical gradient, since the $\hat{s}/q$ term remains subdominant during the current ramp-down phase (Fig. 5-5.c)).

We have seen how in this particular discharge, the electron density gradient can affect

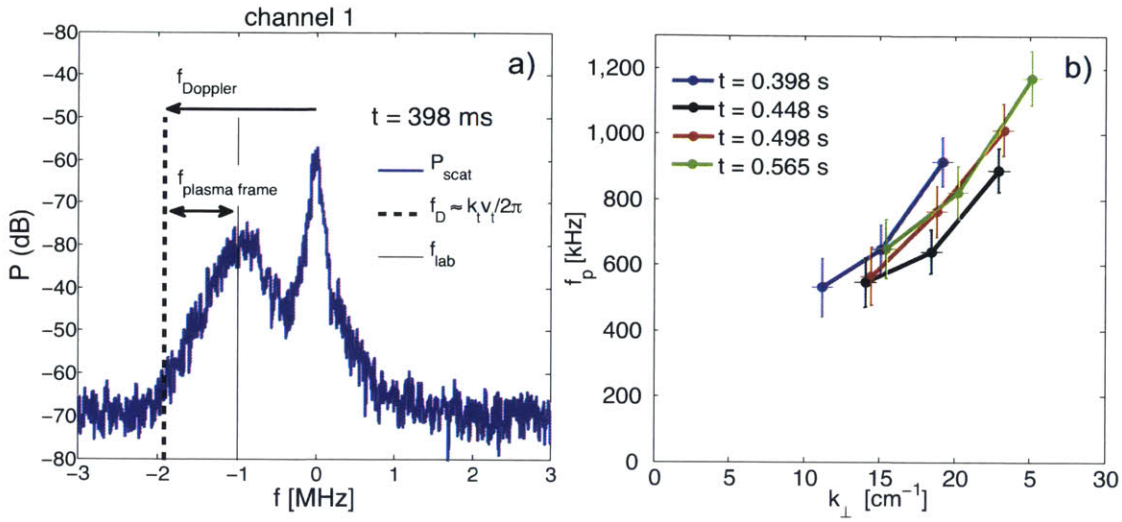

Figure 5-6: $a)$ Scattered power from channel 1 of high-k scattering diagnostic, at time t = 398 ms. Fluctuation frequencies are Doppler shifted by $f_D \approx k_t v_t/2\pi$. The plasma frame frequency of fluctuations f_p is obtained by $f_p = f_{lab} - f_D$. $b)$ Dispersion relation obtained experimentally from measured electron density fluctuations.

transport related quantities such as electron density fluctuations. We now wish to study the dependence of the real frequency of fluctuations with the density gradient. In the previous chapter we saw how the measured frequencies in the lab frame (f_{lab}) are Doppler shifted from intrinsic frequencies of measured fluctuations in the plasma frame f_p, by a quantity $f_D \approx k_t v_t/2\pi$, and $f_p = f_{lab} - f_D$ (Fig. 5-6.a)). A proper justification of the Doppler shifted frequency expression $f_D \approx k_t v_t/2\pi$ is given in the appendix. Here k_t is the toroidal component of the fluctuation wavenumber (obtained from a ray-tracing code), and v_t is the toroidal velocity at the scattering location, obtained from charge exchange recombination spectroscopy (CHERS) measurements [120] and TRANSP calculations ($cf.$ section on Doppler shift in previous chapter). The quantity f_{lab} is defined as $\int fS(f)df / \int S(f)df$, and is shown on figure 5-6.a) for the time $t = 398$ ms, as a black line passing roughly through the maximum of the spectral peak of fluctuations at $f \approx -1000$ kHz. $S(f)$ is the frequency spectral power on figure 5-6.a) at $t = 398$ ms.

At each time in the analysis, the Doppler-subtracted, plasma frame frequency of fluctuations f_p can be plotted against the experimental perpendicular wavenumber (obtained by a ray-tracing code). This provides an experimental dispersion relation of the measured fluctuations, and can be compared with a dispersion relation obtained from a linear gy-

rokinetic simulation. On figure 5-6.b), the plasma frame frequency f_p is plotted against the perpendicular wavenumber $k_\perp$ of the measured fluctuation by the high-k scattering system. In this notation $k_\perp = \sqrt{k_b^2 + k_r^2}$, where k_b is the binormal component of the measured wavenumber and k_r is the radial component ($cf.$ Fig. 3-2). At a given time, the different wavenumbers correspond to the different channels of the high-k scattering diagnostic. The experimental dispersion relation shown on Fig. 5-6 is plotted at four different times. We note that the uncertainties in f_p come from k_t and v_t. Higher wavenumbers give rise to higher plasma frame frequencies. In the following sections, we wish to compare the plasma frame real frequency with real frequencies calculated by GS2 linear analysis.

A wavenumber spectrum of fluctuations can be obtained by integrating the frequency spectrum (Fig. 4-1.a)) from the different channels. In figure 5-7, the wavenumber values are calculated using a ray-tracing code. At $t = 398$ ms the fluctuation level is high, and corresponds to a time when the electron density gradient term (Fig. 5-7.b)) is subdominant in the Jenko critical gradient. At $t = 448$ ms the fluctuation level at low and mid wavenumbers ($k_\perp \rho_s \lesssim 12$) has been greatly reduced. At this time the electron density gradient term has become dominant in the Jenko critical gradient. At $t = 498$ ms the electron density gradient term is still dominant (marginally dominant) in the ETG critical gradient formula. At the same time, lower-k ($k_\perp \rho_s \sim 10$) density fluctuations have no significant change with respect to $t = 448$ ms, but higher-k ($k_\perp \rho_s \gtrsim 12$) density fluctuations at $t = 498$ ms have noticeably increased from $t = 448$ ms levels. At $t = 565$ ms, the fluctuation wavenumber spectrum is similar to the spectrum at $t = 498$ ms at higher-k wavenumbers ($k_\perp \rho_s \gtrsim 13 - 14$) but the lower-k fluctuation level has also increased with respect to $t = 498$ ms. The electron density gradient seems to be most efficient in stabilizing *lower-k* fluctuations ($k_\perp \rho_s \lesssim 10$, still high-k), and also in shifting the spectrum towards higher k.

We have seen in this section how the local value of the electron density gradient is correlated to the density fluctuation amplitude. It is shown how the linear threshold for instability has a clear dependence on the electron density gradient through the Jenko critical gradient formula. In addition, the electron density gradient is shown to have a stabilizing influence on high-k density fluctuations during ETG unstable time periods.

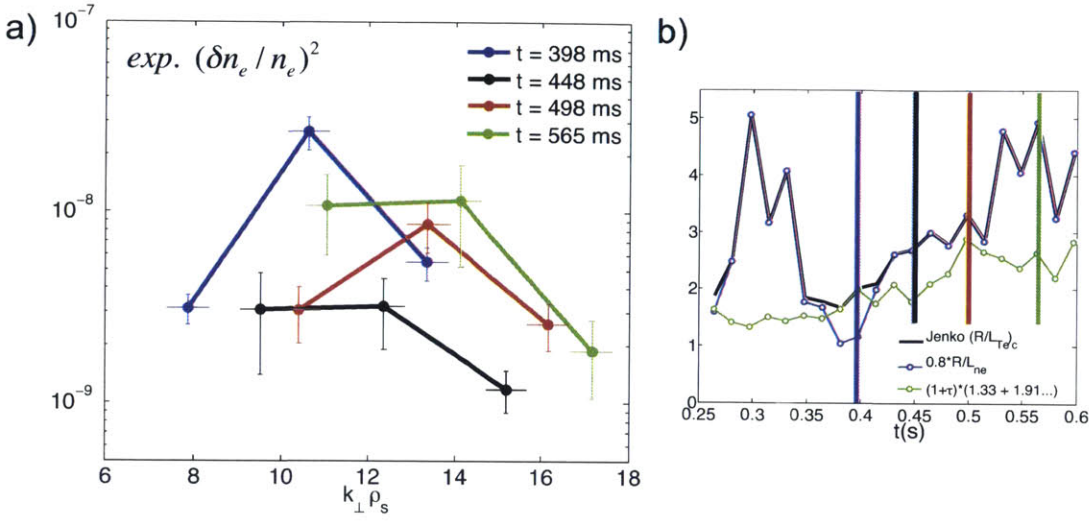

Figure 5-7: *a)* Wavenumber spectrum of electron density fluctuations. Note $k_\perp = \sqrt{k_b^2 + k_r^2}$. *b)* Jenko critical gradient and the two terms in the max function composing it. Note the electron density gradient term is the blue curve. Vertical color lines correspond to the analysis times in *a)*.

5.2 Linear stability analysis

In this section we report on the influence of the electron density gradient on high-k linear growth rates and real frequencies corresponding to linearly unstable wavenumbers from the GS2 gyrokinetic code [95]. GS2 is an initial value gyrokinetic code that uses flux tube geometry. In its linear version, GS2 tracks the fastest growing modes for a given pair of radial and poloidal wavenumbers. In the linear simulations presented in this thesis, the radial component k_r was set to 0 to find the most unstable mode. Electromagnetic effects were also included in these linear runs. The linear simulations shown in this section use local Miller equilibrium [123].

In the first subsection, computed linear growth rates are compared with observed electron density fluctuations from the high-k scattering diagnostic. Experimental profiles were used as input in our linear gyrokinetic simulations. In the second subsection, a scan of the electron density gradient was carried out to confirm the effect of the electron density gradient on high-k linear growth rates and real frequencies from GS2. In the third subsection is shown the impact of the local electron density gradient on real frequency from GS2 and compared with the Doppler subtracted, plasma frame frequency of fluctuations

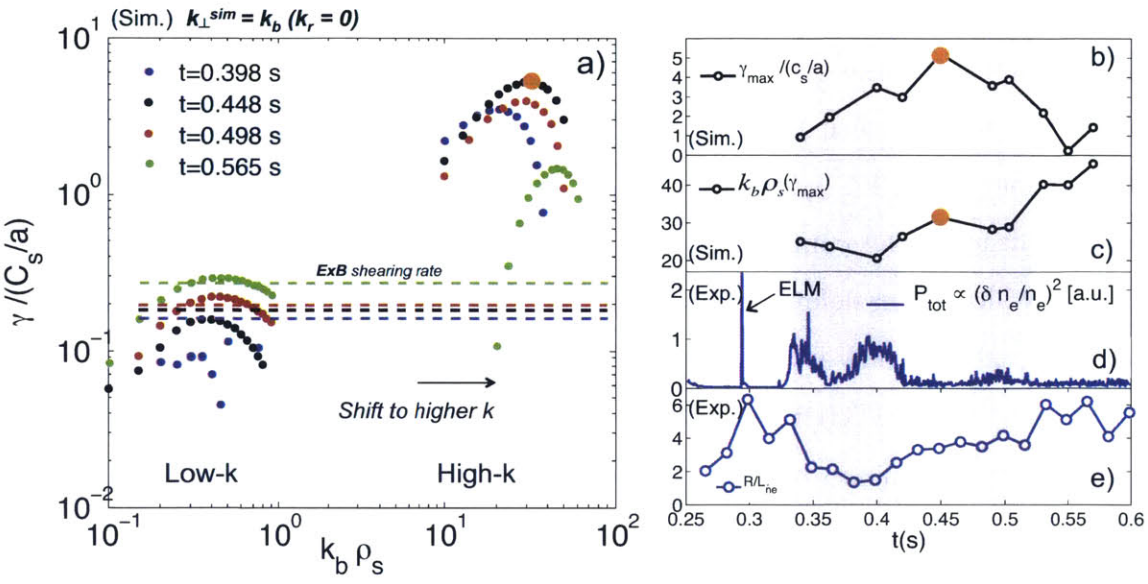

Figure 5-8: a) Linear growth rates computed with GS2 for low-k ($0.1 \lesssim k_b\rho_s \lesssim 1$) and high-k wavenumbers ($10 \lesssim k_b\rho_s \lesssim 60$). Notice the linearly unstable high-k wavenumbers are shifting to even higher wavenumbers as time progresses. Horizontal lines correspond to $E\mathrm{x}B$ shearing rate from TRANSP calculations (Waltz-Miller definition [74]). b) Maximum linear growth rate computed with GS2. c) Wavenumber corresponding to the maximum growth rate computed with GS2. d) Total scattered power (integrated in frequency) from channel 1 of the high-k scattering diagnostic. e) Normalized electron density gradient R_0/L_{n_e} computed at the scattering location. Notice the similarity between figures 5-8.c) and 5-8.e).

from experiment. In subsection four we gather the visual, qualitative correlations in this chapter and try to present them in a more quantitative, systematic way.

5.2.1 Correlation between unstable wave numbers and observed fluctuations.

Linear stability analysis was carried out for low-k ($k_\perp\rho_s \lesssim 1$) and high-k ($k_\perp\rho_s >> 1$) wavenumber values. The wavenumber k_b is normalized with respect to the ion sound gyro radius ρ_s, and the computed linear growth rates are normalized by the quantity c_s/a, where c_s is the ion sound speed, and a is the minor radius.

The computed linear growth rates are shown on figure 5-8 for times $t = 0.398, 0.448, 0.498$ and 0.565 s. In order to calculate linear growth rates GS2 uses experimental profiles at the closest experimental time points. Those times correspond to Thomson scattering diagnos-

tic time points (MPTS), and electron density and temperature values at those times were used as input for linear gyrokinetic calculations on Fig. 5-8. Low-k linear simulations on the ion-scale were carried out for wavenumbers $0.1 \lesssim k_b\rho_s \lesssim 1$ and high-k simulations for wavenumbers $10 \lesssim k_b\rho_s \lesssim 60$, while k_r was set to 0 to find the most unstable mode. $E \times B$ shearing rates computed using TRANSP calculations [71] are also plotted in Fig. 5-8.a) (Waltz-Miller definition [74]) at the analysis times. Similar levels between ExB shearing rates and low-k linear growth rates corresponding to the most unstable mode suggest that low-k (ITG) turbulence is suppressed.

Figure 5-8.a) shows that low-k linear growth rates monotonically increase in time throughout the shot and are substantially lower than high-k linear growth rates. High-k linear growth rates increase from $t = 0.398$ s to $t = 0.448$ s and they decrease afterwards. Linear growth rates (low-k and high-k) from Fig. 5-8.a) are not correlated with the total scattered power from the high-k scattering diagnostic ($P_{tot} \propto (\delta n_e/n_e)^2$ in Fig. 5-8.d)). In fact, at $t = 0.448$ s the high-k linear growth rate attains the highest value among the four times in the analysis (see orange dot), but the fluctuation level in panel 5-8.d) is lowest at that time.

At each time in the analysis the maximum linear growth rate ($\gamma_{max}/(c_s/a)$) and the wavenumber corresponding to that maximum linear growth rate $k_b\rho_s(\gamma_{max})$ are calculated. These two quantities are then computed for several times, and are plotted in Fig. 5-8.b) $-$ c). From the orange dot in 5-8.a) at $t = 0.448$ s, the values of $\gamma_{max}/(c_s/a)$ and $k_b\rho_s(\gamma_{max})$ are retrieved and mapped in 5-8.b) and c). As we previously noticed, no correlation is observed between $\gamma_{max}/(c_s/a)$ and P_{tot} (indicative of electron density fluctuations) from Fig. 5-8.d), however a correlation can be established with the wavenumber at the maximum linear growth rate $k_b\rho_s(\gamma_{max})$. During the time $0.33 \lesssim t \lesssim 0.42$ s (grey time panel), low $k_b\rho_s(\gamma_{max})$ corresponds to a high level of fluctuations. As $k_b\rho_s(\gamma_{max})$ increases between $0.4 \lesssim t \lesssim 0.45$ s, a clear reduction in density fluctuations is observed. A period of slight decrease of $k_b\rho_s(\gamma_{max})$ between $0.45 \lesssim t \lesssim 0.5$ s corresponds to a higher level of scattered power P_{tot}, and a clear increase in $k_b\rho_s(\gamma_{max})$ for $0.5 \lesssim t \lesssim 0.57$ s agrees with a further reduced level of fluctuations.

One additional correlation might be established with the experimental value of the electron density gradient. A similar shape in the curve $k_b\rho_s(\gamma_{max})$ in time (Fig. 5-8.c)

) and the local value of R_0/L_{n_e} (Fig.5-8.e)) suggests a clear correlation. An analysis of these two curves provides an R^2 linear correlation coefficient between $k_b\rho_s(\gamma_{max})$ and R_0/L_{n_e} of $R^2 \approx 85\%$ (note here R^2 denotes a linear correlation coefficient and not major radius). The previous correlation between fluctuations (P_{tot} in Fig. 5-8.d) and $k_b\rho_s(\gamma_{max})$ (Fig. 5-8.c) can be extended to include the local electron density gradient R_0/L_{n_e} (fig. 5-8.e). Low values of R_0/L_{n_e} correspond to higher level of electron density fluctuations and vice-versa.

A remark should be made on the similarity between $k_b\rho_s(\gamma_{max})$ and R_0/L_{n_e}: the previous comments allow us to argue that it is the electron density gradient that is driving high-k turbulence levels (Fig. 5-8.d) to even higher wavenumbers, and at the same time suppressing *lower-k* high-k turbulence. The fluctuation level in Fig. 5-8.d) is indicative of high-k turbulence, and it seems to be driven to even higher wavenumbers by the effect of the local electron density gradient. To confirm this effect a local scan on the electron density gradient is carried out using GS2 and is described in the following subsection.

5.2.2 Electron density gradient scan with GS2.

In the previous subsection, a correlation was established between the fluctuation level from the high-k scattering diagnostic, the linearly unstable wavenumbers corresponding to the maximum growth rate ($k_b\rho_s(\gamma_{max})$) and the local value of the electron density gradient (R_0/L_{n_e}). In this subsection, we give further evidence that supports our previous conclusions of a correlation between the electron density gradient and the linearly unstable wavenumbers at maximum growth rate $k_b\rho_s(\gamma_{max})$.

A scan of the electron density gradient is performed about its experimental value, keeping all other experimental parameters constant. This *scan* is carried out at two different times in the discharge ($t = 398, 565$ ms). Figure 5-9 shows real frequencies and linear growth rates computed for different values of the electron density gradient, and at two different times. At $t = 565$ ms, the electron density gradient has a high value (Fig. 5-8.e)) and is the dominant term in the Jenko critical gradient formula (Fig. 5.2). A scan on the local R_0/L_{n_e} shows a big effect on the real frequency and linear growth rate at $t = 565$ ms computed with GS2 (Fig. 5-9.c) $-$ d)). In fact, additional scans carried out at different

times (and not shown here) show that more the electron density gradient is dominant, the bigger the observed effect on linear growth rates. At $t = 398$ ms, R_0/L_{n_e} has a small value and is subdominant ($cf.$ Fig. 5-8.e) and 5.2). At that time, the real frequency and linear growth rate appear to be practically insensitive to small changes in R_0/L_{n_e} (Fig. 5-9.a) $-$ b)). We have shown in Fig. 5-8 that a direct correlation between the high-k linear growth rates and the local electron density gradient R_0/L_{n_e} cannot be established, so establishing a correlation between linear growth rates in Fig. 5-9 and R_0/L_{n_e} would be inappropriate. Notwithstanding, a correlation between the wavenumber at the maximum linear growth rate and R_0/L_{n_e} can be once more established in the local scan, as is clearly shown on Fig. 5-9.d) as the R_0/L_{n_e} changes. This is once more in agreement with the previous statement that the electron density gradient is driving high-k linearly unstable wavenumbers towards even higher-k values. The local density gradient scan appears to have a very noticleable change on the real frequency at $t = 565$ ms. In the following section we proceed to compare this change in real frequency with experimental plasma frame real frequencies measured by the scattering diagnostic at NSTX.

5.2.3 Electron density gradient and real frequency

In this subsection we show a comparison between the real frequency obtained from linear gyrokinetic simulations using GS2, and the Doppler subtracted, plasma frame real frequency of fluctuations as detected by the high-k scattering diagnostic at NSTX. The Doppler subtraction was performed following the procedure outlined in the previous section of this chapter.

In Figure 5-10 the plasma frame frequency of detected fluctuations is shown in a), and the real frequency of instability is shown in b). An important remark should be made here before the *comparison* is made. The experimental frequencies in a) are plotted against the experimentally detected wavenumbers $k_\perp \rho_s^{exp}$ determined by ray tracing calculations. We saw in chapter 3 on collective scattering measurements at NSTX that the measured wavenumber by the scattering system is mostly radial, but has a small binormal component k_b, and $k_r \gg k_b$. In the present convention, $k_\perp = \sqrt{k_r^2 + k_b^2}$. Recall that typical detected wavenumbers satisfy $k_\perp \sim 20$ cm^{-1}. Concerning the simulation wavenumbers

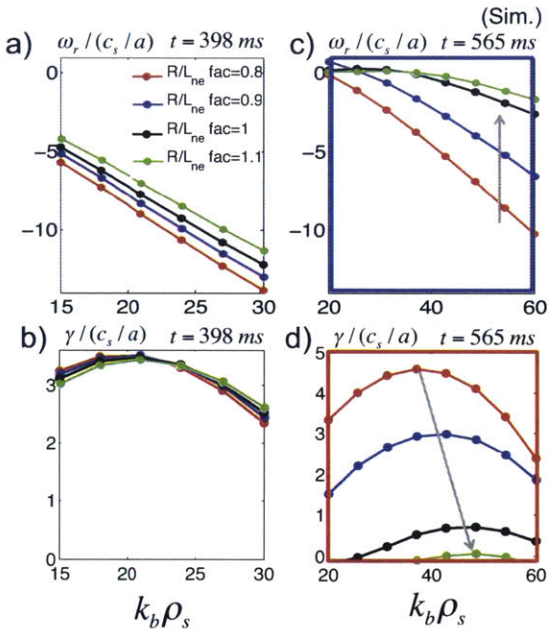

Figure 5-9: A local scan on the electron density gradient is carried out at two times. At $t = 398$ ms, the electron density gradient is low and subdominant in the Jenko critical gradient (Fig. 5-8.d) and 5.2), and is shown to have negligible impact on the real frequency and linear growth rate. At $t = 565$ ms, the electron density gradient is high and dominant in the Jenko critical gradient (Fig. 5-8.d) and 5.2). At that time, a small change in the electron density gradient is shown to have a big impact on the real frequency and linear growth rate.

in b), they are all set to have a null radial component $k_r = 0$. This condition corresponds to the most unstable mode of the instability. In that sense, k_b is the only component left in $k_\perp$, and the real frequencies in b) are plotted against $k_b \rho_s^{sim}$. The difference between the experimental and simulation wavenumbers *precludes* plotting the two curves together. In the discussion that follows we do not attempt to make quantitative comparisons between experiment and simulation and obtain agreement within errorbars. Our goal here is to look for a qualitative trend that might be present in both experiment and the simulation. One reasonable thing to do would be to run linear gyrokinetic simulations specifying the experimental value of the wavenumber as input, instead of setting $k_r = 0$ from the start. These linear simulations were carried out and showed that the mode is linearly stable at the experimental wavenumber value. A convincing explanation of this fact is not currently available. Nonlinear gyrokinetic simulations might be needed to further explore the experimentally detected wavenumber.

We see in Figure 5-10 that the Doppler subtracted experimental frequency seems to increase in time from a lowest value at $t = 398$ ms to a highest value at $t = 565$ ms. This same trend is observed from the linear simulations carried out. In fact, from $t = 398$ ms to $t = 565$ ms, the electron density gradient is increasing, as can be seen from Fig. 5-8.e). As the electron density gradient increases, the frequency is decreased (in absolute value) and approaches 0. This is the same trend observed in the local density gradient scan in the previous subsection.

In the next subsection we go even further and attempt to make a more direct comparison between experiment and simulation, and correlations with the density gradient.

5.2.4 Density gradient and comparison between experiment and linear simulations

In this section we attempt to present the density gradient effects on density fluctuations, linear growth rates and real frequencies that we explained in the previous sections in a slightly different manner. We seek a compact way to quantify the correlations previously found.

In Figure 5-11 are the linear simulation results. Following the procedure established

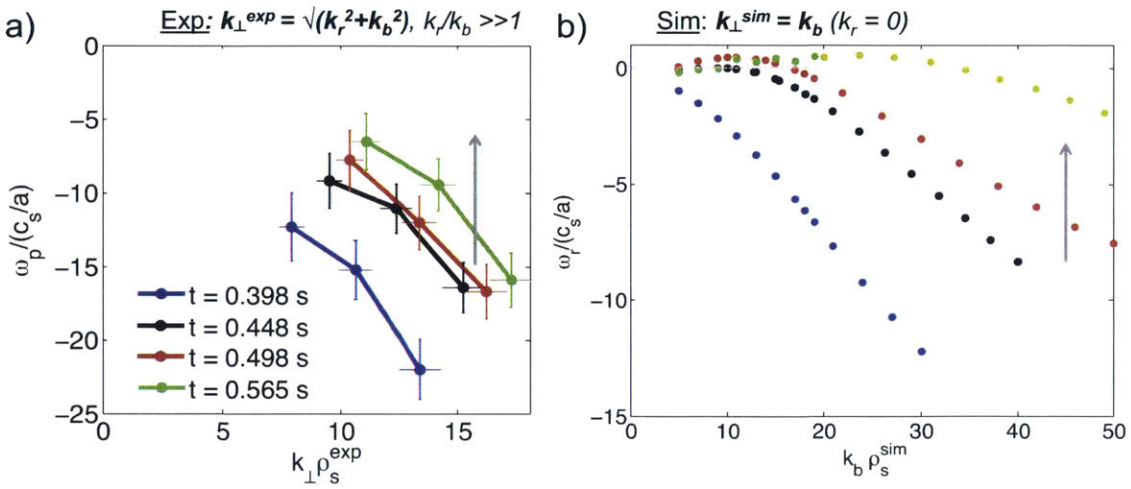

Figure 5-10: $a)$ Doppler subtracted, plasma frame frequency of fluctuations. $b)$ Real frequency of instability from GS2 linear gyrokinetic simulations. Note the very similar behavior of the real frequencies from experiment and simulation.

previously, at each time we calculate the maximum linear growth rate $\gamma_{max}/(c_s/a)$ and the wavenumber corresponding to the maximum growth rate $k_b\rho_s(\gamma_{max})$. At the particular time of $t = 0.42$ s, these values are taken from the orange dot in Fig. 5-11.a). Linear simulations are run at different times, and the corresponding values of $\gamma_{max}/(c_s/a)$ and $k_b\rho_s(\gamma_{max})$ are retrieved. At each time, a local value of the electron density gradient is also obtained, and one can plot $\gamma_{max}/(c_s/a)$ and $k_b\rho_s(\gamma_{max})$ as a function of the local value of the electron density gradient. The plots are shown in 5-11.c) and d). A very weak correlation is observed between $\gamma_{max}/(c_s/a)$ and R_0/L_{n_e}, and was previously mentioned in this chapter. However, a clear correlation is observed between the wavenumber at maximum linear growth rate and the electron density gradient R_0/L_{n_e}, and the linear correlation coefficient is found to be $R^2 \approx 85\%$. This correlation was already observed previously in this chapter, and is presented here once more in a different manner.

To exploit the correlation between real frequency and density gradient, we choose to pick a fixed wavenumber, and calculate at each time, the frequency corresponding to that fixed wavenumber. We chose the wavenumber $k_b\rho_s = 30$, and the real frequencies at four of the analysis times are shown in figure 5-11.b). The orange dots correspond to the real frequency values at $k_b\rho_s = 30$ (Fig. 5-11.e)). In a similar way as was done with the linear growth rates, $\omega_r(k_b\rho_s = 30)$ is plotted against the local value of R_0/L_{n_e} at the

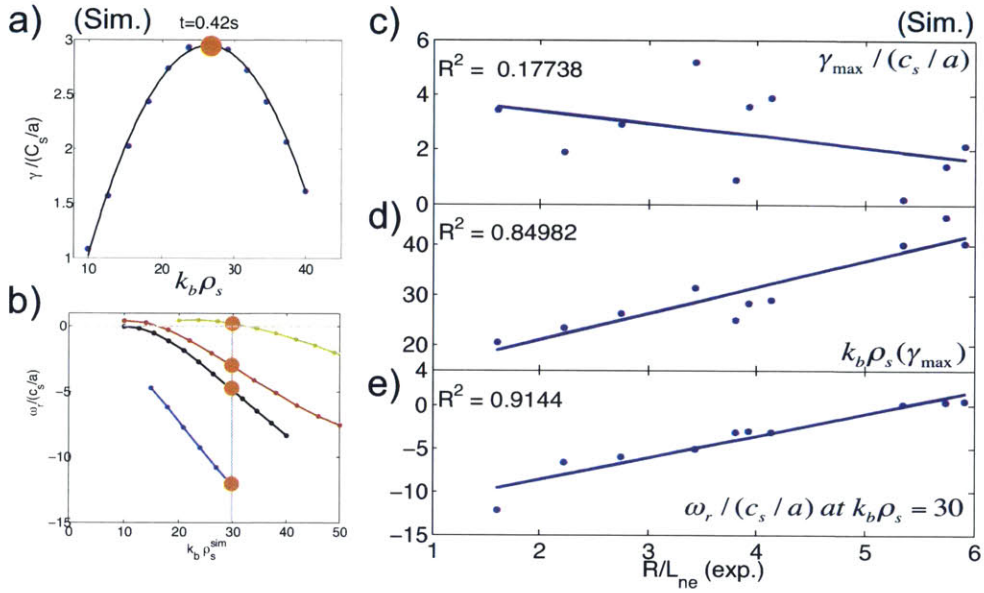

Figure 5-11: At each time, the maximum linear growth rate $\gamma_{max}/(c_s/a)$ and the wavenumber corresponding to the maximum linear growth rate $k_b\rho_s(\gamma_{max})$ are recorded (a)), and are plotted against the local value of the density gradient in $c)$ and d). To analyze the real frequency, the real frequency is calculated at a fixed wavenumber ($k_b\rho_s = 30$) and is plotted in $e)$ as a function of density gradient.

corresponding time. A very clear correlation is observed, and a correlation coefficient of $R^2 \approx 91\%$ is obtained. This once more is a very clear indication, from the simulation, of the effect of the local density gradient on real frequency of instability calculated by GS2.

In figure 5-12 we try to make a very analogous analysis, but this time using experimental measurements. A very clear parallel between figure 5-11 and 5-12 can be made if linear growth rates are substituted with the wavenumber spectrum of fluctuations from experiment, as shown in figure 5-7.a). This can be argued by a simple mixing length argument ($cf.$ [124]). The real frequency from GS2 is replaced with the Doppler subtracted, plasma frame frequency of fluctuations from experiment. The maximum fluctuation level $(\delta n_e/n_e)^2_{max}$ is plotted against the density gradient in fig. 5-12.c) and the wavenumber corresponding to the maximum fluctuation level is plotted in 5-12.d). It should be mentioned here that this analysis was only carried for times when there was a clear maximum in the wavenumber fluctuation spectrum, as in figure 5-12.a). Cases where a maximum in the wavenumber fluctuation spectrum could not be easily determined were rejected. In practice, when the fluctuation level was determined by 3 points (3 wavenumbers corre-

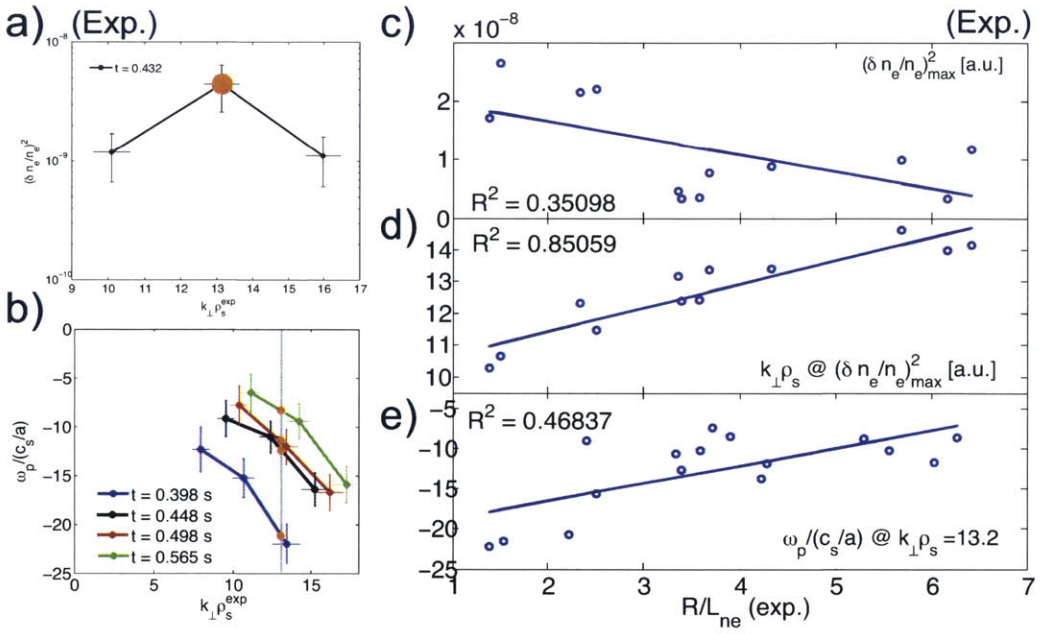

Figure 5-12: This figure is the experiment analog of figure 5-11. At each time, the maximum fluctuation level $(\delta n_e/n_e)^2$ and the wavenumber corresponding to the maximum fluctuation level $k_b\rho_s@(\delta n_e/n_e)^2_{max}$ are recorded (a)), and are plotted against the local value of the density gradient in $c)$ and d). The real frequency is calculated at a fixed wavenumber ($k_\perp\rho_s = 13.2$) and is plotted in $e)$ as a function of density gradient.

sponding to 3 channels, as in a)), were kept only those cases where the maximum clearly lied in the mid-wavenumber, in order to clearly keep track of the maximum of the fluctuation level and the corresponding wavenumber. Concerning the plasma frame frequency, we picked a fixed wavenumber, $k_\perp \rho_s = 13.2$, and plot on 5-12.e) the frequency corresponding to that wavenumber as a function of density gradient. The same trends found from the linear simulation are reproduced from experimental data. The best correlation is observed between the wavenumber at maximum fluctuation level and the density gradient.

The correlation found between the wavenumber at maximum fluctuation level and density gradient in fig. 5-12.d) can have a tricky interpretation and we would like to discuss it here. Concerning the experiment, it is true that a gradient in the electron density affects the measurement wavenumber from the different channels by refracting the incident beam of radiation. The measurement wavenumber from each channel slightly changes in time, and in fact, if one were to plot the measured wavenumber from a particular channel with respect to the density gradient, one would find a very clear correlation. Refraction acts to increase the detected wavenumber by each channel of the scattering diagnostic. This effect has nothing to do with plasma turbulence but is purely a refraction effect due to density gradient. In the appendix we discuss how a density gradient can give rise to beam refraction using a simple model, and one can see that the refraction angle $\alpha \propto dn_e/dr$. Following this argument, one could interpret fig. 5-12.d) as being purely a refraction effect. However, figure 5-12.d) is picking the wavenumber that gives rise to a maximum fluctuation level, which itself *is* a turbulence-related quantity. Even though a density gradient is indeed bending the probe beam and resulting in bigger detected wavenumbers, when the measurement records a maximum in fluctuation level for a mid-wavenumber (a case with a clear maximum in $(\delta n_e/n_e)^2$), this is telling us that turbulence is strongest at that particular wavenumber, and is the crucial point behind figure 5-12.d). As we have seen from figure 5-11, linear gyrokinetic simulations from GS2 are in agreement with the experimental observation.

We have shown in this section a quantitative way of presenting the several correlations observed throughout this chapter. Throughout this chapter we have tried to emphasize the different correlations observed from simulations and experiment with the density gradient, and are *condensed* in figures 5-11 and 5-12. The same qualitative trends are observed both

from simulation and experiment. The local value of the density gradient seems to be a main actor affecting high-k turbulence levels in the plasma discharge presented here. One distinctive feature of this discharge might be the fact that the ETG appears to be density gradient dominated, as indicated from figure 5-3, and this seems to be the explanation of the large influence of the electron density gradient in this plasma. Further work might encompass studying the density gradient dependence in similar discharges, and certainly one major step in the present analysis would be to study the impact of density gradient on transport using TRANSP and nonlinear gyrokinetic simulations.

Appendix A

Expression of Doppler shift frequency

We want to establish a reliable and simple formula for the Doppler shift frequency ω_D from first physics principles. The widely used expression $\omega_D \approx k_t v_t$ is here justified in a proper manner. I will first carry out the derivation and state the assumptions made one by one as the reasoning progresses. I will justify the use of these assumptions at the end of this appendix.

Assume the plasma frame is moving at a uniform velocity $\boldsymbol{\beta} = \boldsymbol{v}/c$ with respect to the lab frame. It is well known from first physics principles that the relation between ω_{lab} and ω_p is

$$\omega_{lab} = \omega_p(1 + \boldsymbol{\beta} \cdot \boldsymbol{n}) = \omega_p + \omega_D \tag{A.1}$$

where $\boldsymbol{n}$ is directed from the source of emission (plasma frame) to the observation point (lab frame). ω_D is the Doppler shift, and it is in general given by $\omega_D = \boldsymbol{k} \cdot \boldsymbol{v}$. However, we can try to simplify this expression thanks to our knowledge of the turbulent fluctuation wave vector $\boldsymbol{k}$ and the velocity of the plasma frame $\boldsymbol{v}$, dominated by toroidal rotation. We use the orthonormal coordinate system $(\hat{\boldsymbol{e}}_{\boldsymbol{r}}, \hat{\boldsymbol{e}}_{\|}, \hat{\boldsymbol{e}}_{\boldsymbol{b}})$ of figure 4-3. We can decompose the dot product $\boldsymbol{k} \cdot \boldsymbol{v}$ into its parallel and perpendicular components (with respect to the magnetic field $\boldsymbol{B}$)

$$\boldsymbol{k} \cdot \boldsymbol{v} = k_{\|} v_{\|} + \boldsymbol{k}_{\perp} \cdot \boldsymbol{v}_{\perp} \tag{A.2}$$

We make a first assumption[1] stating that $k_{\|} v_{\|} \ll \boldsymbol{k}_{\perp} \cdot \boldsymbol{v}_{\perp}$. Second, we can decompose

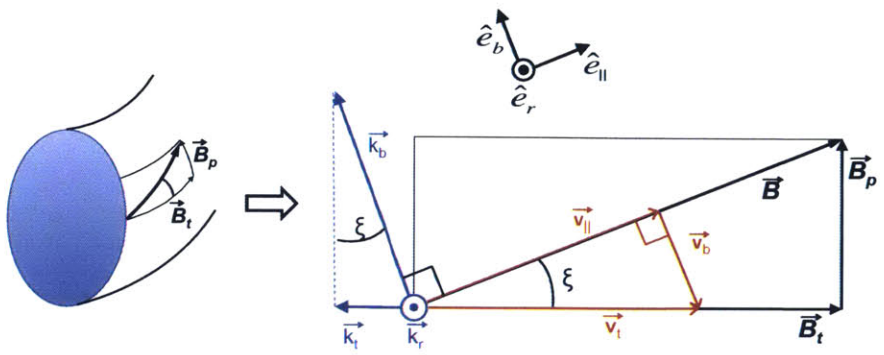

Figure A-1: Flux surface geometry used to compute the Doppler shift frequency ω_D of fluctuations introduced due to toroidal rotation. We use the orthonormal coordinate system $(\hat{e}_r, \hat{e}_{\parallel}, \hat{e}_b)$ in the radial, parallel and binormal directions respectively. ξ is the magnetic pitch angle.

the perpendicular component into the binormal and radial components introduced in figure 4-3. We have

$$\boldsymbol{k} \cdot \boldsymbol{v} \approx \boldsymbol{k}_{\perp} \cdot \boldsymbol{v}_{\perp} = k_b v_b + k_r v_r \tag{A.3}$$

We make a second assumption[2] stating that $k_r v_r \ll k_b v_b$, and we obtain

$$\boldsymbol{k} \cdot \boldsymbol{v} \approx k_b v_b \tag{A.4}$$

Here v_b is the binormal component of the plasma frame velocity (not directly available from diagnostics) and k_b is the binormal component of the detected fluctuation wavenumber $\boldsymbol{k}$. By use of simple geometry, we can further simplify this expression. From figure 4-3 we have $sin(\xi) = k_t/k_b$. At this stage we make yet a third simplifying assumption[3] stating that the total velocity of the plasma is uniquely in the toroidal direction, and it is the sum of the parallel and binormal components of the plasma velocity. More formally, we assume

$$\boldsymbol{v}_{\parallel} + \boldsymbol{v}_{\boldsymbol{b}} \approx \boldsymbol{v}_{\boldsymbol{t}} \tag{A.5}$$

This is the underlying assumption made in fig. 4-3. Knowing this, we have $sin(\xi) = v_b/v_t$, which allows us to express A.4 as

$$\omega_D = \boldsymbol{k} \cdot \boldsymbol{v} \approx k_b v_b = \frac{k_t}{sin(\xi)} v_t sin(\xi) = k_t v_t \tag{A.6}$$

This expression for the Doppler shift frequency ω_D is the desired expression, and the one used in the analysis of Doppler subtraction performed in this thesis to obtain plasma frame frequency of fluctuations, as explained in chapter 5.

I now turn to justify the use of the previous assumptions made in the derivation of A.6.

1. This assumption states $k_\parallel v_\parallel \ll \boldsymbol{k}_\perp \cdot \boldsymbol{v}_\perp = k_\perp v_\perp$.

   It is well established from magnetized plasma turbulence theory that $k_\parallel \sim 1/qR$, where q is the safety factor and R is the major radius [97]. Knowing this we have

   $$\frac{k_\parallel v_\parallel}{k_\perp v_\perp} \sim \frac{1}{qR}\frac{1}{k_\perp}\frac{v_\parallel}{v_\perp} \sim \frac{1}{qR}\frac{1}{k_\perp}\frac{1}{tan\xi} \tag{A.7}$$

   where we made use of $v_r \ll v_b$, or equally $v_\perp \approx v_b$ (which gives $v_\parallel / v_b = tan\xi$). Plugging in typical values from experiment we have

   $$\frac{k_\parallel v_\parallel}{k_\perp v_\perp} \sim \frac{1}{qR}\frac{1}{k_\perp}\frac{v_\parallel}{v_\perp} \sim \frac{1}{5 \times 1m}\frac{1}{2000m^{-1}}\frac{1}{tan\xi} \sim \frac{1}{10000}\frac{1}{tan\xi} \ll 1 \tag{A.8}$$

   where use was made of typical perpendicular wavenumbers $k_\perp \approx 2000$ m^{-1} as obtained from ray tracing calculations. The quantity in A.8 is much smaller than 1 for typical values of the magnetic pitch angle ξ in experiment. Note we could've also used values of $k_\parallel$ obtained from ray tracing calculations. In either case, the conclusion would've been the same. With this we have justified assumption 1.

2. This assumption states that $k_r v_r \ll k_b v_b$

   We rely once more of typical values of k_r and k_b from ray tracing, and v_r and v_b from TRANSP calculations. We have

   $$\frac{k_r v_r}{k_b v_b} \sim \frac{20cm^{-1}}{5cm^{-1}}\frac{v_r}{v_b} \sim 4\frac{v_r}{v_b} \ll 1 \tag{A.9}$$

   which justifies assumption 2.

3. The third assumption states $\boldsymbol{v}_{\|} + \boldsymbol{v}_{\boldsymbol{b}} \approx \boldsymbol{v}_{\boldsymbol{t}}$.

   Note this is an assumption on the flux-surface plasma velocity components. Making no approximation whatsoever, we can always write

$$\boldsymbol{v}_{\|} + \boldsymbol{v}_{\boldsymbol{b}} = \boldsymbol{v}_{\boldsymbol{t}} + \boldsymbol{v}_{\boldsymbol{p}} \tag{A.10}$$

   where $\boldsymbol{v}_{\boldsymbol{p}}$ is the poloidal component of the velocity. In A.10 we simply expressed the flux-surface velocity components in a different coordinate system (toroidal t and poloidal p components, instead of parallel $\|$ and binormal b components). The approximation $\boldsymbol{v}_{\|} + \boldsymbol{v}_{\boldsymbol{b}} \approx \boldsymbol{v}_{\boldsymbol{t}}$ thus simply translates that $v_p \ll v_t$, which is generally justified in tokamak plasmas. TRANSP calculations are in accordance with this assumption in our particular experiment.

Neoclassical theory is able to justify assumptions 2 and 3 in a proper manner. The reader is referred to reference [28] for a more theory based justification of these two assumptions. Here we simply used experimental values for our particular experiment as calculated using TRANSP to justify our assumptions.

We have thus justified the widely used expression of the Doppler shift frequency $\omega_D \approx k_t v_t$ from first physics principles.

Appendix B

Comments about beam refraction and diffraction and gaussian beam propagation

It is instructive to understand the origin of the refraction effects from plasma inhomogeneities. We have seen that the scattering angle θ_s is selected beforehand by the collection geometry. We will see that refraction effects can produce a bending of the probe beam, (see Fig. 3-2) thus affecting the value of the scattering angle θ_s with respect to straight line propagation of the probe beam. Since the scattering angle θ_s is directly related to the measured wavennumber k by the Bragg relation (eq. 3.6), it is important to correctly determine the value of θ_s by properly taking into account refraction effects. Here we turn to explain how plasma inhomogeneities (the electron density gradient) explain the process of beam refraction.

Assume an incident beam of electromagnetic radiation of frequency ω_i (and finite width d) enters a plasma of electron density n_e. The electric field of the incident beam varies as $\boldsymbol{E} = Ee^{i(\boldsymbol{k_i}\cdot\boldsymbol{x}-\omega_i t)}$. As the beam propagates a distance L into the plasma, its phase varies as $\phi = \int_L \boldsymbol{k_i}\cdot\boldsymbol{dl}$, where $\boldsymbol{dl}$ follows the ray trajectory. This can also be written as $\phi = \int_L (N\omega_i/c)dl$.

Due to the finite width of the probe beam and a plasma density gradient (inhomogeneity in the plasma makes $N = N(\boldsymbol{r}, t)$), each ray in the beam will experience a different

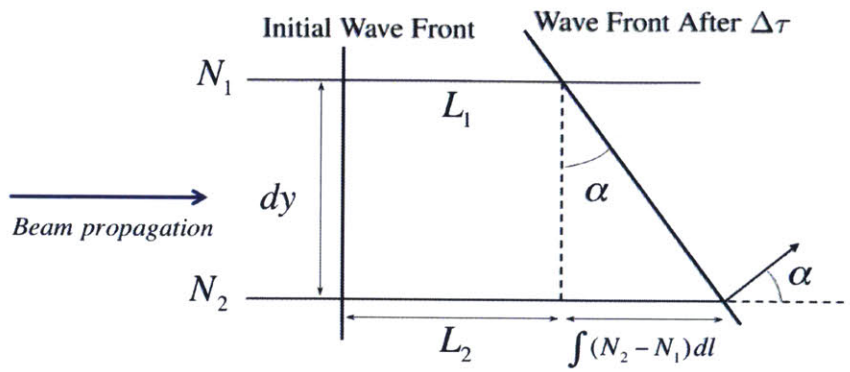

Figure B-1: Deviation of light rays in an inhomogeneous plasma. The inhomogeneity manifests itself as a variation of the refractive index N with position. Note how each ray in the probe beam traverses a medium with different refractive index N. This gives rise to differences in the optical path for each ray (assume finite beam width), which ultimately translates into a bending of the wave front.

refraction index N, which will give rise to a phase shift between the rays and subsequently refraction of the beam. As we can see from figure B-1, the refraction angle of the probe beam α due to the phase shift between the rays is

$$tan(\alpha) \approx \alpha \approx \left(\int_{L_2} N_2 dl_2 - \int_{L_1} N_1 dl_1 \right) / dy \approx \int_L (N_2 - N_1) dl/dy \tag{B.1}$$

At high frequencies, we have seen that the refractive index of the medium satisfies the Appleton-Hartree dispersion relation 4.9, which can be further simplified (at high frequencies) by $N^2 = 1 - \omega_{pe}^2/\omega^2$. Since $\omega_{pe} \ll \omega$ ($c.f.$ section 4.4), we have $N \approx 1 - n_e/2n_c$, where n_c is the cutoff frequency given by $n_c = \omega^2 m_e \epsilon_0 / e^2$. Knowing this, we can find a simple expression for the refraction angle as the beam traverses the plasma

$$\alpha \approx \int_L (N_2 - N_1) dl/dy \approx \int_L -(n_{e_2} - n_{e_1})/2n_c dl/dy \approx \int_L -(\partial n_e/\partial y) dl/(2n_c dy) \approx \frac{n_e}{n_c} \frac{L}{2L_{n_e}} \tag{B.2}$$

where L is the length of the propagation of the beam inside the plasma, and L_{n_e} is the density gradient scale length of the plasma as the probe beam traverses it $L_{n_e} = n_e/|\nabla n_e|$. Here we shall assume $L \sim R_0, 2R_0$. Using typical NSTX values $R_0/L_{n_e} \approx 4$,

$n_e \approx 4.10^{19}$ m^{-3} and $n_c \approx 10^{21}$ m^{-3}, one finds $\alpha \sim 10^o$. This value of the beam refraction angle is of the same order as typical scattering angles θ_s in collective scattering experiments with the high-k system at NSTX. We see the importance of using ray-tracing calculations: a simple minded estimate of the scattering angle assuming straight line probe beam propagation would be off by a value of $\alpha \sim 10^o$. This erroneous value of θ_s would in turn propagate to an erroneous value of the detected avenumber k by the high-k system (using the Bragg condition $k = 2k_i \sin(\theta_s/2)$). Not taking refraction effects into account gives a very poor estimate of the measured wavenumber k.

We have thus given a physical intuitive explanation of the scattering of the probe beam as it propagates in the plasma from first physics principles. It is important to realize that the density gradient effect on beam propagation is not a plasma turbulence effect. The density gradient effect here is independent of the electron-scale turbulence stabilization by density gradient discussed in chapter 5. The effect that the electron density gradient has on electron scale turbulence is independent of the refraction process by density gradient.

The probe beam launched into the plasma is approximately gaussian. As is described in [92, 127], the beam is quasi-optically transformed as it exits the waveguide to produce a probe beam suitable for scattering experiments. The 2-D beam intensity profiles are measured with a pyroelectric detector and are fit to a gaussian function. The beam radius w and the radius of curvature of the wave front R_c characterize a gaussian beam (note that for a plane wave $R_c = \infty$, as is the case for $z = 0$) and they are given by

$$w(z) = w_0(1 + z^2/z_R^2)^{1/2} \qquad R(z) = (z^2 + z_R^2)/z \tag{B.3}$$

where z_R is the Rayleigh length $z_R = k_i w_0^2/2$ and z is the coordinate along the direction of propagation of the central ray (see Fig. B-2). Typical value of $z_R \approx 80$ cm (using $\lambda_i = 1.07$ mm, $w_0 = 1.65$ cm). For values of $z \gg z_R$, w has a linear dependence with z and the beam divergence angle is $\theta_R \approx 4/k_i w_0 \approx 2.36^o$. For the purpose of scattering of microwaves a plane phase front is required, so the scattering volume should be located at the beam waist (region near $z = 0$ where $R_c \to \infty$). The diffraction process on the probe beam propagation manifests itself as the divergence θ_R. Diffraction effects will be negligible at short wavelength, and the condition is $\theta \ll \lambda/\pi w_0$. We have thus in hand

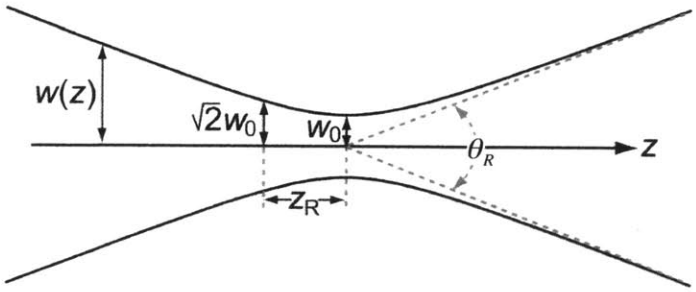

Figure B-2: Schematic of propagation of of Gaussian beam. The probe beam is prepared to scatter at the beam waist w_0 is the beam waist (where wave-front is plane), z_R is the Rayleigh length and θ_R is the beam divergence angle (image modified from [68]) pg. 46.

a useful condition for the importance of the diffraction effects on the probe beam, as we did for refraction. Note that the refraction condition depends on the plasma condition (density gradient) while the refraction effects depend exclusively on the characteristics of the launched beam λ and w_0.

Appendix C

List of Matlab routines used in this thesis

The routines used in the course of this work were written in Matlab. Some of the routines used were written by myself, although I would like to show my gratitude especially to Yang Ren for having put his personal routines available, which were of great use and continue to be. The routines presented here are used to access and plot NSTX data, perform ray tracing calculations, prepare and analyze input and output files for using GS2 and for using TRANSP. The routines are located in my personal directory $/u/jruizrui/matlab/myroutines$.

The following routines were used to access NSTX and TRANSP data

- get_shot_charact Get general characteristics of the plasma dicharge (see details in the acutual routine).
- get_mirnov.m Get signal from Mirnov coils.
- get_bfield.m Get components of magnetic field B.
- get_efit.m Get data from EFIT equilibrium reconstruction.
- get_lrdfit.m Get data from LRDFIT equilibrium reconstruction.
- get_s.m Get magnetic shear $\hat{s}$ and other equilibrium reconstruction parameters.
- get_mpts.m Get MPTS data.

- get_chers.m Get CHERS data.
- get_transp.m Get TRANSP data.
- plot_chi_transp.m Produce plots from TRANSP data.
- mean_freq_dop.m Perform Doppler shift frequency subtraction.
- get_hkdata.m Get data from high-k fluctuation data.
- get_kspec_more_nofit.m Get wavenumber spectrum of fluctuations from high-k diagnostic.
- k_spectrum_t.m Obtain wavenumber spectrum of high-k fluctuations.
- plot_highk_spec.m Construct and plot high-k fluctuation spectrogram.
- analysis_routine_3.m Analyze correlations between equilibrium quantities and high-k data.

The ray-tracing routines used in this thesis are the following:

- call_raytracing.m main routine that calls ray_tracing_nstx.m.
- ray_tracing_nstx.m (function) inputs: (shot, time, lxang, lzang, cmxang, ew_win, ew_xang,ew_yang,varargin). outputs: matlab structure (rt) with information from probe beam (pb), scattered beam (sb), and other relevant information.
- ray_tracing_2010.m Equivalent routine to ray_tracing_nstx.m.

The following routines are used to create input files for GS2 and also to plot and analyze GS2 output.

- gs2_submit.m Create input file and submit to GS2.
- call_gs2_submit.m Routine that calls $gs2\_submit.m$ with proper input data.
- plot_gs2.m This routine extracts the proper output data from GS2 to plot it conveniently.
- plot_plot_gs2.m Plot GS2 linear growth rate, real frequency and eigenfunctions.

Bibliography

[1] A. M. Bradshaw et al., Fusion Engineering and Design **86**, 2770 (2010).

[2] H. S. Bosch and G. M. Hale, Nucl. Fusion **32**, 611 (1992).

[3] J D Lawson, 1957 Proc. Phys. Soc. B **70** 6.

[4] $http://www.ideen2020.de/$, Max Planck Institute for Plasma Physics.

[5] Shafranov V D, Bondarenko B D, Goncharov G A, On the history of the research into controlled thermonuclear fusion, Physics ? Uspekhi **44** (8) 835-865 (2001).

[6] I. E. Tamm, *Plasma Physics and the Problem of Controlled Thermonuclear Reactions*, Vol. 1, Edited by Leontovich M. A., Pergamon Press, New York, 1962, p.1.

[7] A. D. Sakharov, *Plasma Physics and the Problem of Controlled Thermonuclear Reactions*, Vol. 1, Edited by Leontovich M. A., Pergamon Press, New York, 1962, p 21.

[8] J. P. Freidberg, *Ideal MHD*, Cambridge University Press, 2014.

[9] Y.-K.M. Peng and D.J. Strickler, Nucl. Fusion, **26** 769 (1986).

[10] R.T.C Smith, *et al.*, *"Design of the START Experiment."*Proceedings- Symposium of Fusion Engineering 2 (1989): 866-68.

[11] S. M. Kaye, *et al.*, Fusion Technol. **36** (1999) 16.

[12] M. Ono, *et al.*, Nucl. Fusion **40** (2000) 557.

[13] A. Sykes, *et al.*, Nucl. Fusion **39** 1271 (1999).

[14] Y.-K.M. Peng, *et al.*, Fusion Sci. Technol. **56** 957 (1986).

[15] T. Brown, J. Menard, P. Titus, A. Zolfaghari, L. El-Guebaly, and L. Mynsberge, "Progess in developping the STFNSF configuration." These proceedings. [25th Symposium on Fusion Engineering (SOFE), San Francisco, June 10-14, 2013].

[16] ITER Physics Basis, Nucl. Fusion **39**, 2178 (1999).

[17] W. Guttenfelder, *et al.*, Phys. Plasmas **19**, 056119 (2012).

[18] W. Guttenfelder, *et al.*, Nucl.Fusion **53**, 093022 (2013).

[19] G. Rewoldt, *et al*, Phys. Plasmas **3**, 1667 (1996).

[20] S. M. Kaye *et al*, Nucl. Fusion **47**, (2007) 499.

[21] S. M. Kaye *et al*, Nucl. Fusion **49**, 499 (2009).

[22] T. S. Hahm and K. H. Burrell, Phys. Plasmas **2**, 1648 (1995).

[23] K. H. Burrell, Phys. Plasmas **4**, 1499 (1997).

[24] K. H. Burrell, Phys. Plasmas **6**, 4418 (1999).

[25] J. E. Kinsey *et al.*, Phys. Plasmas **14**, 102306 (2007).

[26] J.E. Menard *et al.*, Nuc. Fusion **52**, 083015 (2012).

[27] T. E. Evans, *et al.*, Nucl. Fusion **48** 024002 (2008).

[28] P. Helander and D. Sigmar, *Collisional Transport in Magnetized Plasmas*, Cambridge Monographs on Plasma Physics, Cambridge University Press, 2002.

[29] J. P. Freidberg, *Plasma Physics and Fusion Energy*, Cambridge University Press, 2007.

[30] R. Bickerton, J. Connor and J. Taylor, Nature Phys. Sci. **229**, 110 (1971).

[31] B. B. Kadomtsev, V. D. Shafranov, Nucl. Fusion Suppl. **209**, 110 (1972).

[32] M. C. Zarnstoff *et al.*, Phys. Rev. Lett. **60**, 1306 (1988).

[33] P. K. Browning, *et al.*, Phys. Rev. Lett. **68** 1722 (1992).

[34] J. R. Wilson, *et al.*, Phys. Plasmas **10**, 1733 (2003).

[35] F. L. Hinton and R. D. Hazeltine, Rev. Mod. Phys. **48**, 239 (1976).

[36] M. C. Zarnstorff and S. C. Prager, Phys. Rev. Let. **53**, 454 (1984).

[37] M. C. Zarnstorff and S. C. Prager, Phys. Fluids **29**, 298 (1986).

[38] M. C. Zarnstorff et al., Phys. Plasmas **4**, 1097 (1997).

[39] A. J. Wootton *et al.*, Phys. Fluids B **12**, 2879 (1990).

[40] W. Horton, Rev. Mod. Phys. **71**, 735 (1999).

[41] B. Coppi, M. N. Rosenbluth, and R. Z. Sagdeev, Physics of Fluids **10(3)** 582- 587 (1967).

[42] M. Porkolab and G. S. Kino, Phys. Rev. Lett., **15**, 752-755 (1965).

[43] M. Porkolab, Nuclear Fusion **8**(1), 29 (1968).

[44] W. Horton *et al.*, Phys. Fluids **24**, 1077 (1981).

[45] B.B. Kadomtsev and O.P. Pogutse, Nuclear Fusion **11**(1), 67 (1971).

[46] W. Horton, B. G. Hong, and W. M. Tang, Phys. Fluids **31**(10), 2971-2983, 1988.

[47] R. D. Hazeltine and H. R. Strauss, Phys. Rev. Lett. **37**, 102 (1976).

[48] D. Stutman *et al.*, Phys. Rev. Lett. **102**, 115002 (2009).

[49] E. Mazzucato *et al.*, Phys. Rev. Lett. **101**, 075001 (2008).

[50] F. Chen. *Introduction to Plasma Physics and Controlled Fusion*, Springer, 1984.

[51] J. Weiland, *Collective Modes in Inhomogeneous Plasmas: Kinetic and Advanced Fluid Theory*, Series in Plasma Physics. Taylor and Francis, 2000.

[52] C Bourdelle., Plasma Phys. Control. Fusion **47**(5A), A317-A326 (2005).

[53] X. Garbet *et al.*, Plasma Phys. Control. Fusion **46**, B557-B574 (2004).

[54] J. W. Connor and O. P. Pogutse, Plasma Phys. Control. Fusion **43**, 155?175 (2001).

[55] D. R. Ernst *et al.*, Phys. Plasmas **11**, 2637 (2004).

[56] T. Dannert and F. Jenko, Phys. Plasmas **12**, 072309 (2005).

[57] A. M. Dimits *et al.*, Phys. Plasmas **7**, 969 (2000).

[58] F. Jenko and W. Dorland, Phys. Rev. Lett. **89**, 225001 (2002).

[59] D. Stutman *et al.*, Phys. Rev. Lett. **102**, 115002 (2009).

[60] N. N. Gorelenkov *et al.*, Nuclear Fusion **50**, 084012 (2009) .

[61] T. Kondoh *et al.*, Rev. Sci. Instrum. **72**, 1143 (2001).

[62] M. Stejner *et al.*, Plasma Phys. Control. Fusion **57** 062001 (2015).

[63] E. Mazzucato, *Bull. Am. Phys. Soc.* **20**, 1241 (1975); Princeton University Plasma Physics Laboratory Report MATT-1151 (1975).

[64] E. Mazzucato, Phys. Rev. Lett. **36**, 792 (1976).

[65] I. H. Hutchinson, *Principles of Plasma Diagnostics* (Cambridge University Press, Cambridge, UK, 2002), 2nd ed.

[66] T. H. Stix, *Waves in Plasmas* (Springer-Verlag, New York, 1992).

[67] E. Mazzucato *et al.*, Nucl. Fusion **49**, 055001 (2009).

[68] E. Mazzucato, *Electromagnetic Waves for Thermonuclear Fusion Reasearch*, World Scientific 2014.

[69] Press W. H., Flannery, B. P., Teukolsky, S. A. and Vetterling, W. T., *Numerical Recipes*, Cambridge University Press, Cambridge, 1988.

[70] P. T. Bonoli and E. Ott, Phys. Fluids **25**, 359 (1982).

[71] R. J. Hawryluk, *Physics of Plasma Close to Thermonuclear Conditions*, (Pergamon, New York, 1981).

[72] J. P. H. E. Ongena *et al*, *Proceedings of the Tenth Carolus Magnus Summer School on Plasma and Fusion Energy Physics*, Fusion Science and Technology **61** 2T 180-189 (2012).

[73] $http://w3.pppl.gov/transp/$.

[74] R. E. Waltz and R. L. Miller, Phys. Plasmas **6**, 4265 (1999).

[75] P. Devynck *et al*, Plasma Phys. Control. Fusion **35**, 63-75 (1993).

[76] H. K. Park, PhD thesis, UCLA (1984).

[77] H. K. Park *et al* Rev. Sci. Instrum. **53**, 1535 (1982).

[78] ITER Technical Basis, *ITER EDA Documentation Series* No. 24, IAEA, Vienna, 2002.

[79] X. Garbet, Y. Idomura, L. Villard, and T.H. Watanabe, Nuclear Fus., **50**(4), 043002 (2010).

[80] P. J. Catto, W. M. Tang, and D. E. Baldwin, Plasma Physics **23** (7), 639 (1981).

[81] E. A. Frieman and Liu Chen, Phys. Fluids **25**(3), 502-508 (1982).

[82] G.G. Howes *et al.*, The Astrophysical Journal **651**, 590?614 (2006).

[83] A. J.Brizard and T. S. Hahm, Rev. Mod. Phys. **79**, 421 (2007).

[84] M. A. Beer, S. C. Cowley, and G. W. Hammett, Phys. Plasmas **2**, 2687 (1995).

[85] $http://gs2.sourceforge.net$

[86] J.R. Ball, MS dissertation, MIT (2013).

[87] W. Dorland, M. Kotschenreuther, *Notes on Local Equilibrium Implementation*, from pppl.gov.

[88] L.L. Lao *et al.*, Nuclear Fusion **30** (6), 1035 (1990).

[89] *http://nstx-u.pppl.gov/software/lrdfit.*

[90] K. L. Wong *et al.*, Phys. Rev. Lett. **99**, 135003 (2007).

[91] NSTX 5 Year Plan for FY2009-2013, ch. 1, p. 4.

[92] D. R. Smith *et al.*, Rev. Sci. Instrum., **79**, 123501 (2008).

[93] S. M. Kaye, M. Ono, Y.-K. Peng, D. B. Batchelor, M. D. Carter, *et al.*, Fus. Technol. **36**, 16 (1999).

[94] F. Jenko *et al*, Phys. Plasmas **8**, 4096 (2001).

[95] M. Kotschenreuther *et al*, Comput. Phys. Commun. **88** 128 (1995).

[96] J. E. Menard *et al.*, Nuclear Fusion **51** (2011) 103014.

[97] W. Horton., Rev. Mod. Phys. **71**, 735 (1999).

[98] W. Horton., *Turbulent Transport in Magnetized Plasmas*, World Scientific, London 2012.

[99] P. N. Guzdar *et al*, Phys. Rev. Lett. **57**, 2818 (1986).

[100] W. Horton, B. G. Hong, and W. M. Tang, Phys. Fluids **31**, 2971 (1988).

[101] W. Horton. *et al*, Nucl. Fusion **45**, (2005) 976-985.

[102] J. W. Connor, H. R. Wilson, Plasma Phys. Control. Fusion **36**, 719 (1994).

[103] W. Dorland, F. Jenko, M. Kotschenreuther, and B.N. Rogers, Phys. Rev. Lett. **85** 5579 (2000).

[104] F. Jenko, W. Dorland, M. Kotschenreuther, and B.N. Rogers, Phys. Plasmas **7** 1904 (2000).

[105] F. Jenko and W. Dorland, Phys. Rev. Lett. **89**, 225001 (2002).

[106] R. E. Waltz, J. Candy, and M. Fahey, Phys. Plasmas **14**, 056116 (2007).

[107] D. R. Smith *et al*, Phys. Rev. Lett. **102** 225005 (2009).

[108] Y. Ren *et al*, Nucl. Fusion **53** (2013) 083007.

[109] H. Y. Yuh *et al*, Phys. Plasmas **16**, 056120 (2009).

[110] H. Y. Yuh *et al*, Phys. Rev. Lett. **106** 055003 (2011).

[111] Y. Ren *et al*, Phys. Rev. Lett. **106** 165005 (2011).

[112] Y. Ren *et al*, Phys. Plasmas **19**, 056125 (2012).

[113] E. Mazzucato, Phys. Plasmas **10**, 753 (2003).

[114] E. Mazzucato, Plasma Phys. Control. Fusion **48**, 1749 (2006).

[115] S. M. Kaye *et al*, Nucl. Fusion **49**, (2009) 045010.

[116] G. T. Hoang *et al*, Phys. Rev. Lett. **87** 125001 (2001).

[117] G. T. Hoang *et al*, Phys. Plasmas **10**, 405 (2003).

[118] W. Horton *et al*, Phys. Plasmas **11**, 2600 (2004).

[119] M. Greenwald *et al*, Phys. Rev. Lett. **53**, 352 (1984).

[120] R. E. Bell, Rev. Sci. Instrum, **74**, 10E902 (2006).

[121] B.P. LeBlanc *et al*, Rev. Sci. Instrum, **74**, 1659 (2003).

[122] F. M. Levinton and H. Yuh, Rev. Sci. Instrum, **79**, 10F522 (2008).

[123] R. L. Miller *et al*, Phys. Plasmas **5** 973 (1998).

[124] X. Garbet, Plasma Phys. Control. Fusion **43**, A251?A266 (2001).

[125] NSTX Upgrade Five Year Plan for FY2014-2018, nstx-u.pppl.gov.

[126] J. Sheffield, D. Froula, S. H. Glenzer, N. C. Luhmann, Jr. *Plasma Scattering of Electromagnetic Radiation*, Burlington, MA : Academic Press/Elsevier, 2011.

[127] D. R. Smith, *Investigation of electron gyroscale fluctuations in the National Spherical Torus Experiment*, Ph.D. dissertation, Princeton University (2009).